



UNIVERSITÀ
DEGLI STUDI
FIRENZE

DOTTORATO DI RICERCA IN
Agricultural and environmental sciences

CICLO XXXV

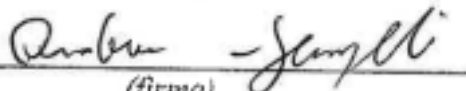
COORDINATORE Prof. Pietramellara Giacomo

**INNOVATIVE APPLICATIONS OF LOW-COST HYPERSPECTRAL
TECHNOLOGIES IN PLANTS PHENOTYPING AND POST-HARVEST
PROCESSES**

Settore Scientifico Disciplinare AGR/02

Dottorando

Dott. Genangeli Andrea


(firma)

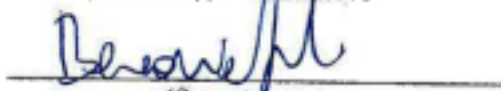
Tutor

Prof. Bindi Marco


(firma)

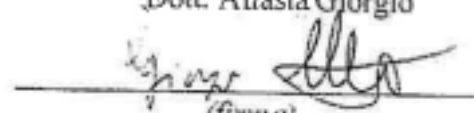
Co-tutor

Dott. Gioli Beniamino


(firma)

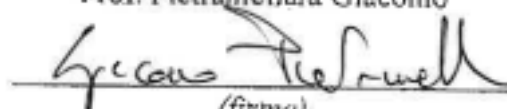
Co-tutor

Dott. Allasia Gjorgio


(firma)

Coordinatore

Prof. Pietramellara Giacomo


(firma)

Anni 2019/2022

Table of contents

Introduction.....	1
References.....	4

Chapter one

A novel methodology to improve the performance of a portable low-cost hyperspectral camera

Premise.....	8
1.1 Introduction.....	8
1.2 Materials and methods.....	11
1.2.1 Experimental activities.....	11
1.2.2 Hyperspectral devices.....	11
1.2.3 The HCM.....	14
1.2.4 Test of the HCM.....	16
1.3 Results and discussions.....	18
1.3.1 Signal noise computation and characterization.....	18
1.3.2 HCM test results.....	22
1.4 Conclusions.....	26
1.5 Attachments.....	27
References.....	29

Chapter two

Low-cost hyperspectral imaging to detect drought stress in high-throughput phenotyping

Premise	35
2.1 Introduction	35
2.2 Materials and methods	38
2.2.1 Experimental design.....	38
2.2.2 Phenotyping Platform and RGB acquisition process.....	39
2.2.3 Environmental monitoring.....	40
2.2.4 Stress induction and evapotranspiration.....	41
2.2.5 RGB images segmentation and OIs.....	42
2.2.6 Hyperspectral data acquisition and processing.....	43
2.2.7 Automatic segmentation of HIS.....	44
2.2.8 Hyperspectral data analysis.....	45
2.3 Results	46
2.3.1 Environmental variations and ET.....	47
2.3.2 HTPP results.....	48
2.3.3 Hyperspectral analysis.....	52
2.4 Discussions	56
2.5 Conclusions	59
References	61

Chapter three

A novel hyperspectral method to detect moldy core in apple fruits

Premise	68
3.1 Introduction	69
3.2 Materials and methods	71
3.2.1 Instrument setup.....	72
3.2.2 Experimental measurements.....	72
3.2.3 Transmittance retrieval.....	74
3.2.4 Band ratio and average transmittance.....	74
3.2.5 Binary classification.....	74
3.3 Results and discussions	76
3.3.1 Infection rate.....	76
3.3.2 Spectral correlations.....	78
3.3.3 Transmittance temporal pattern.....	79
3.3.4 Binary classification and ANN-AP.....	81
3.4 Conclusions	85
References	87

Chapter four

Conclusions	95
Further activities carried out during the PhD period	98

Introduction

The progressive increase of the world population in correspondence with the growing consumer needs for better quality food and standardised products is a paramount necessity for all actors involved in the supply chain concerning food production, distribution, and sale [1-5]. Simultaneously, improving the detection and monitoring of ecosystem conditions is necessary when global biodiversity loss is accelerating at an unprecedented rate due to industrial production, agricultural process development and the massive diffusion of highly productive crops [6-8]. The global environmental impact of agricultural production and connected processes is being addressed by all governments worldwide and national and international institutions, as highlighted in the 2030 Agenda, a document subscribed to 193 countries members of the United Nations (UN) [9], and in several reports produced by the Food and Agriculture United Nations Organization (FAO) [10]. The main actions recommended for developing more sustainable agriculture include digitising the monitoring processes by developing and applying non-invasive technologies [11-13]. Therefore, recent advances in optical technologies and precision agriculture have permitted the progressive development and affirmation of spectral sensors (SSs) [14,15]. The SSs are total non-invasive technologies capable of collecting the electromagnetic signal in the visible, near-infrared, and short wave infra-red spectrum (VIS–NIR–SWIR) [16], representing a valuable tool to monitor growth and health status in agricultural productions [17,18]. The spectral reflectance of vegetation is mainly a function of optical tissue properties, canopy biophysical properties, soil reflectance, viewing geometry and illumination circumstances [19,20]. Several vegetation indices (VIs), derived from spectral vegetation reflectance such as the Normalized Difference Vegetation Index (NDVI) and red-edge position (REP), can quantify crop health, water, and nutrient content [21,22]. Advances in reflectance spectroscopic techniques also provided the opportunity of using hyperspectral imaging spectrometers for detecting VIs [23]. Specifically, Hyperspectral Imaging (HSI) has become an important technique for analysing a wide spectrum of light and is capable of measuring hundreds of spectral bands from different devices such as aircraft, satellite platforms or directly on the field [13,16,17,24,25]. Recent hyperspectral sensors technologies encouraged the development

of a new generation of low-cost SSs, improving their interest and potential application for industrial processes in agriculture [26-28]. Therefore, the development and application of low-cost monitoring and analysis methods based on hyperspectral technologies represent a safe and non-invasive way to increase the performance of several agriculture industrial processes, such as developing novel phenotyping techniques to select and test new plant varieties and developing innovative quality control methods for the post-harvest phase. [29-32].

This PhD belongs to a doctorate program jointly promoted by the National Research Council of Italy (CNR) and the Italian industrial association (Confindustria), aimed at strengthening the connection between doctoral scientists and industrial research. Within this program, CNR and private companies are founding selected PhD fellowships in cooperation with national universities. Therefore, this thesis is based on the project initially proposed by the private company FOS S.p.A and jointly agreed upon by the Institute of BioEconomy (CNR IBE) and the University of Florence – DAGRI.

This PhD thesis explores and offers new ways for the profitable application of low-cost spectral technologies in an industrial research context. The aim of this PhD is to develop innovative low-cost hyperspectral applications to retrieve bio-physical indicators of plants and fruit status in phenotyping processes and post-harvest phases through controlled experiments. In this work, I present the methodologies and the results of my research obtained by the application of the hyperspectral technologies at different spatial scales, each focusing on an aspect of agriculture production processes:

- i) Plant scale: at the sub-metric spatial resolution, as achieved by a low-cost hyperspectral camera first time integrated into a high throughput phenotyping platform during a tomato phenotyping drought stress experiment.
- ii) Fruit scale: at centimetric and sub-centimetric spatial scale, as achieved in a novel Lab setup using a portable spectrometer to assess and quantify through unprecedented efficiency and precision the presence of internal damage by biotic agents in apple fruits.

For each spatial scale, specific experiments have been designed and conducted. The experimental activity and data collection were performed in the years 2020 and 2021 during the 1st and 2nd years of this PhD, leaving the 3rd year for the completion of data analysis and the scientific publication.

This PhD thesis is composed of four chapters. Chapters one, two, and three are written as journal papers with the aim of publication in international scientific journals. Chapter three is already published in an international journal. At the beginning of each chapter, the link to the journal identified for submission or the link to find the published article is given. After chapter four, other research activities and products conducted during the PhD period were synthetically reported.

The general contents of each chapter are listed below:

- Chapter one: The hyperspectral instruments used in the experimental activities of this PhD thesis were presented and explained. The critical issues derived from using the hyperspectral devices were discussed. A novel correction method to optimise the hyperspectral output of a low-cost portable hyperspectral camera was proposed and tested. The results obtained in this chapter allowed us to realise the experiment reported in the following chapter.
- Chapter two: A low-cost hyperspectral camera was first time integrated into a high-throughput phenotyping platform during a tomato drought stress experiment, conducted using four untested tomato genotypes with high industrial interest. A Novel acquisition set-up and segmentation method for the hyperspectral images were developed. The genotype responses to the water stress obtained by the image analysis of the phenotyping platform outputs were compared to a novel hyperspectral index for the water stress detection obtained by processing the hyperspectral images.
- Chapter three: An innovative low-cost system based on hyperspectral spectroscopy in the near-infrared spectral region is proposed to obtain the non-invasive detection of internal damage by biotic agents in apple fruits. The novel system is based on a light collection by an integrating sphere. The system was tested on 70 apples cultivar Golden Delicious infected by *Alternaria alternata*, one of the main pathogens responsible for the apple's internal damage. The spectral features linked to the internal damages were identified, and two binary classification models based on Artificial Neural Network Pattern Recognition and Bagging Classifier with decision trees were developed and tested.
- Chapter four: The overall conclusions and the possible industrial implications of this PhD were reported and discussed.

References

- 1- Borsellino, Valeria, Emanuele Schimmenti, and Hamid El Bilali. 'Agri-Food Markets towards Sustainable Patterns'. *Sustainability* 12, no. 6 (January 2020): 2193. <https://doi.org/10.3390/su12062193>
- 2- Vermeulen, Sonja J., Bruce M. Campbell, and John S.I. Ingram. 'Climate Change and Food Systems'. *Annual Review of Environment and Resources* 37, no. 1 (21 November 2012): 195–222. <https://doi.org/10.1146/annurev-environ-020411-130608>
- 3- Searchinger, Tim, Craig Hanson, Janet Ranganathan, Brian Lipinski, Richard Waite, Robert Winterbottom, Ayesha Dinshaw, et al. *Creating a Sustainable Food Future. A Menu of Solutions to Sustainably Feed More than 9 Billion People by 2050*. World Resources Report 2013-14: Interim Findings. World Resources Institute, 2014. <https://hal.archives-ouvertes.fr/hal-01129910>
- 4- Garnett, Tara. 'Three Perspectives on Sustainable Food Security: Efficiency, Demand Restraint, Food System Transformation. What Role for Life Cycle Assessment?' *Journal of Cleaner Production, Towards eco-efficient agriculture and food systems: Selected papers from the Life Cycle Assessment (LCA) Food Conference, 2012, in Saint Malo, France, 73 (15 June 2014): 10–18*. <https://doi.org/10.1016/j.jclepro.2013.07.045>
- 5- Searchinger, Tim, Richard Waite, Craig Hanson, Janet Ranganathan, Patrice Dumas, and Emily Matthews. 'Creating a Sustainable Food Future', 5 December 2018. <https://policycommons.net/artifacts/1360128/creating-a-sustainable-food-future/1973409/>
- 6- Leadley, Paul, Andrew Gonzalez, David Obura, Cornelia B. Krug, Maria Cecilia Londoño-Murcia, Katie L. Millette, Adriana Radulovici, et al. 'Achieving Global Biodiversity Goals by 2050 Requires Urgent and Integrated Actions'. *One Earth* 5, no. 6 (17 June 2022): 597–603. <https://doi.org/10.1016/j.oneear.2022.05.009>
- 7- Ortiz, Andrea Monica D., Charlotte L. Outhwaite, Carole Dalin, and Tim Newbold. 'A Review of the Interactions between Biodiversity, Agriculture, Climate Change, and International Trade: Research and Policy Priorities'. *One Earth* 4, no. 1 (22 January 2021): 88–101. <https://doi.org/10.1016/j.oneear.2020.12.008>

- 8- Jhariya, Manoj Kumar, Arnab Banerjee, Ram Swaroop Meena, and Dhiraj Kumar Yadav, eds. Sustainable Agriculture, Forest and Environmental Management. Singapore: Springer Singapore, 2019. <https://doi.org/10.1007/978-981-13-6830-1>
- 9- ‘THE 17 GOALS | Sustainable Development’. <https://sdgs.un.org/goals>
- 10- 2021 (Interim) Global Update Report: Agriculture, Forestry and Fisheries in the Nationally Determined Contributions. FAO, 2021. <https://doi.org/10.4060/cb7442en>
- 11- Saiz-Rubio, Verónica, and Francisco Rovira-Más. ‘From Smart Farming towards Agriculture 5.0: A Review on Crop Data Management’. *Agronomy* 10, no. 2 (February 2020): 207. <https://doi.org/10.3390/agronomy10020207>
- 12- Alchanatis, V., and Y. Cohen. ‘Special Issue: Sensing Technologies for Sustainable Agriculture.’ *Biosystems Engineering* 114, no. 4 (2013): 357–483 <https://www.cabdirect.org/cabdirect/abstract/20133135815>
- 13- Gogoi, N.K., Bipul Deka, and L.C. Bora. ‘Remote Sensing and Its Use in Detection and Monitoring Plant Diseases: A Review’. *Agricultural Reviews*, 21 December 2018. <https://doi.org/10.18805/ag.R-1835>
- 14- Zhang, Jingcheng, Yanbo Huang, Ruiliang Pu, Pablo Gonzalez-Moreno, Lin Yuan, Kaihua Wu, and Wenjiang Huang. ‘Monitoring Plant Diseases and Pests through Remote Sensing Technology: A Review’. *Computers and Electronics in Agriculture* 165 (1 October 2019): 104943. <https://doi.org/10.1016/j.compag.2019.104943>
- 15- Shafi, Uferah, Rafia Mumtaz, José García-Nieto, Syed Ali Hassan, Syed Ali Raza Zaidi, and Naveed Iqbal. ‘Precision Agriculture Techniques and Practices: From Considerations to Applications’. *Sensors* 19, no. 17 (January 2019): 3796. <https://doi.org/10.3390/s19173796>
- 16- Berger, Katja, Miriam Machwitz, Marlena Kycko, Shawn C. Kefauver, Shari Van Wittenberghe, Max Gerhards, Jochem Verrelst, et al. ‘Multi-Sensor Spectral Synergies for Crop Stress Detection and Monitoring in the Optical Domain: A Review’. *Remote Sensing of Environment* 280 (1 October 2022): 113198. <https://doi.org/10.1016/j.rse.2022.113198>
- 17- Dale, Laura M., André Thewis, Christelle Boudry, Ioan Rotar, Pierre Dardenne, Vincent Baeten, and Juan A. Fernández Pierna. ‘Hyperspectral Imaging Applications in Agriculture and Agro-Food Product Quality and Safety Control: A Review’. *Applied Spectroscopy Reviews* 48, no. 2 (1 March 2013): 142–59. <https://doi.org/10.1080/05704928.2012.705800>

- 18- Khanal, Sami, Kushal Kc, John P. Fulton, Scott Shearer, and Erdal Ozkan. 'Remote Sensing in Agriculture—Accomplishments, Limitations, and Opportunities'. *Remote Sensing* 12, no. 22 (January 2020): 3783. <https://doi.org/10.3390/rs12223783>
- 19- Sonobe, Rei, Tomohito Sano, and Hideki Horie. 'Using Spectral Reflectance to Estimate Leaf Chlorophyll Content of Tea with Shading Treatments'. *Biosystems Engineering* 175 (1 November 2018): 168–82. <https://doi.org/10.1016/j.biosystemseng.2018.09.018>
- 20- Ge, Yufeng, Abbas Atefi, Huichun Zhang, Chenyong Miao, Raghuprakash Kastoori Ramamurthy, Brandi Sigmon, Jinliang Yang, and James C. Schnable. 'High-Throughput Analysis of Leaf Physiological and Chemical Traits with VIS–NIR–SWIR Spectroscopy: A Case Study with a Maize Diversity Panel'. *Plant Methods* 15, no. 1 (26 June 2019): 66. <https://doi.org/10.1186/s13007-019-0450-8>
- 21- Huang, Sha, Lina Tang, Joseph P. Hupy, Yang Wang, and Guofan Shao. 'A Commentary Review on the Use of Normalized Difference Vegetation Index (NDVI) in the Era of Popular Remote Sensing'. *Journal of Forestry Research* 32, no. 1 (1 February 2021): 1–6. <https://doi.org/10.1007/s11676-020-01155-1>
- 22- Hennessy, Andrew, Kenneth Clarke, and Megan Lewis. 'Hyperspectral Classification of Plants: A Review of Waveband Selection Generalisability'. *Remote Sensing* 12, no. 1 (January 2020): 113. <https://doi.org/10.3390/rs12010113>
- 23- Thenkabail, Prasad S., John G. Lyon, and Alfredo Huete. *Hyperspectral Indices and Image Classifications for Agriculture and Vegetation*. CRC Press, 2018. Google-Books-ID: zoqADwAAQBAJ
- 24- Gamon, J. A., B. Somers, Z. Malenovsky, E. M. Middleton, U. Rascher, and M. E. Schaepman. 'Assessing Vegetation Function with Imaging Spectroscopy'. *Surveys in Geophysics* 40, no. 3 (1 May 2019): 489–513. <https://doi.org/10.1007/s10712-019-09511-5>
- 25- Thenkabail, Prasad S., John G. Lyon, and Alfredo Huete. *Hyperspectral Remote Sensing of Vegetation, Second Edition, Four Volume Set*. CRC Press, 2022. Google-Books-ID: DqR9EAAAQBAJ
- 26- Stuart, Mary B., Leigh R. Stanger, Matthew J. Hobbs, Tom D. Pering, Daniel Thio, Andrew J. S. McGonigle, and Jon R. Willmott. 'Low-Cost Hyperspectral Imaging System: Design and Testing for Laboratory-Based Environmental Applications'. *Sensors* 20, no. 11 (January 2020): 3293. <https://doi.org/10.3390/s20113293>

- 27- Stuart, Mary B., Andrew J. S. McGonigle, Matthew Davies, Matthew J. Hobbs, Nicholas A. Boone, Leigh R. Stanger, Chengxi Zhu, Tom D. Pering, and Jon R. Willmott. 'Low-Cost Hyperspectral Imaging with A Smartphone'. *Journal of Imaging* 7, no. 8 (August 2021): 136. <https://doi.org/10.3390/jimaging7080136>
- 28- Huang, Peikui, Xiwen Luo, Jian Jin, Liangju Wang, Libo Zhang, Jie Liu, and Zhigang Zhang. 'Improving High-Throughput Phenotyping Using Fusion of Close-Range Hyperspectral Camera and Low-Cost Depth Sensor'. *Sensors* 18, no. 8 (August 2018): 2711. <https://doi.org/10.3390/s18082711>
- 29- Bodner, Gernot, Alireza Nakhforoosh, Thomas Arnold, and Daniel Leitner. 'Hyperspectral Imaging: A Novel Approach for Plant Root Phenotyping'. *Plant Methods* 14, no. 1 (December 2018): 84. <https://doi.org/10.1186/s13007-018-0352-1>
- 30- Feng, Xuping, Yihua Zhan, Qi Wang, Xufeng Yang, Chenliang Yu, Haoyu Wang, ZhiYu Tang, Dean Jiang, Cheng Peng, and Yong He. 'Hyperspectral Imaging Combined with Machine Learning as a Tool to Obtain High-Throughput Plant Salt-Stress Phenotyping'. *The Plant Journal* 101, no. 6 (2020): 1448–61. <https://doi.org/10.1111/tpj.14597>
- 31- Sirisomboon, Panmanas. 'NIR Spectroscopy for Quality Evaluation of Fruits and Vegetables'. *Materials Today: Proceedings, International Conference on Advances in Science & Engineering ICASE -2017, 19th – 22nd January 2017*, 5, no. 10, Part 3 (1 January 2018): 22481–86. <https://doi.org/10.1016/j.matpr.2018.06.619>
- 32- Cattaneo, Tiziana M. P., and Annamaria Stellari. 'Review: NIR Spectroscopy as a Suitable Tool for the Investigation of the Horticultural Field'. *Agronomy* 9, no. 9 (September 2019): 503. <https://doi.org/10.3390/agronomy9090503>

Chapter one

A novel methodology to improve the performance of a low-cost hyperspectral portable camera

Premise

This chapter will be submitted as a journal paper to the peer-reviewed journal “*JSI—Journal of Spectral Imaging*”. The journal homepage is available here:

<https://www.impopen.com/jsi>

1.1 – Introduction

Improving the detection and monitoring of the ecosystem conditions is a critical issue when Earth’s biodiversity loss due to human activities is accelerating at an unprecedented rate [1,2]. Recent advantages in data processing and data mining, simultaneously with the development of spectral sensors (SSs) capable of retrieving spectral information from the earth’s surface using the electromagnetic radiation reflected by a terrestrial target, have permitted to opening new ways in environmental monitoring. Several ecological parameters have been successfully measured from SSs installed on satellite or airborne platforms, e.g. the variation of the CO₂ emissions from forest ecosystems and the greenhouse gas emissions from human activities and the health status of marine ecosystems [3-5]. Advances in precision agriculture techniques have demonstrated how analysing the spectral information in the electromagnetic spectrum can be a valuable tool to monitor the growth and health status of crops and agricultural products [6]. The SSs have been applied in agricultural production to improve the efficiency of processes during all supply chain operations, such as monitoring the leaves’ water content during the crop growth in the field and the quality control process during the post-harvest phases [7,8]. The application of spectral technologies (STs) in agriculture field have permitted to improve several agricultural practices, e.g. crop breeding and phenotyping applications in high-throughput phenotyping application [9], agricultural land use monitoring and crops classification from satellite or airborne platform [10,11], cereals yield forecasting [12], and ecosystem services about soil and water resources or losses in biodiversity [13]. The STs are classified as multispectral (MS) and hyperspectral (HIS) concerning the number of the spectral bands obtainable in the same data acquisition; the spectral range

suitable for MS and HIS instruments is usually classified into several spectral regions, respectively: visible light spectrum (VIS) characterised by a spectral range from 350 to 700 nm, Near-infrared (NIR) light spectrum ranging from 700 to 1100 nm, and infrared-shortwave (SWIR) highlighted by a light spectrum from 1200 to 2500 nm [14]. Multispectral technology (MT) is an optical technology able to acquire up to fourteen spectral bands simultaneously, and a hyperspectral technology (HIT) can acquire more than fourteen spectral bands [1,14]. SSs are divided in spectrometers (Ss) and imaging spectrometers (ISs). Ss is generally composed of an optical fibre cable to collect electromagnetic radiation from a defined area, returning a single spectral signature. HITs are based on push broom and snapshot sensors; a push broom sensor is a line-scan able to obtain an image with a travel of the sensor (e.g. airborne, or industrial conveyor belts) and a snapshot sensors, more recent than push broom sensors, are able to obtain an image of $n \times n$ pixel size, and the resolution of the sensor is expressed in megapixel (MP) [15]. HITs based on snapshot sensor are managed by an imaging detector that collects an image composed of a specific number of pixels and a defined number of spectral bands. Indeed, the light is focused on an optical sensor to form an image consisting of multiple spectral bands [15,16]. A hyperspectral image (HI) is the result of the acquisition using an HIT, and each pixel is composed of the spectral information for each band selected; the spectral information is expressed in digital counts (DC), also called counts, as a digital unit or in radiance ($\text{mW}/\text{nm} \cdot \text{sr} \cdot \text{m}^2$) as a measure of the intensity of the electromagnetic radiation for a defined area [17]. The data obtained are structured in a 3-Dimensional hyperspectral data cube, also described as a hypercube (HC), where the image size is the optical resolution of the HI expressed in MP [18], and the spectral resolution is the sampling rate and bandwidth in which the sensor collects the information about the target [19]. HIS application in agricultural activities consisting of the elaboration of Vegetation indices (VIs) obtained by spectral vegetation reflectance, as for the widely used Normalized Difference Vegetation Index (NDVI) based on a spectral ratio between red and near-infrared spectral bands [17]. In the last few years, several VIs were developed and tested to retrieve multiple biochemical parameters, e.g. chlorophyll content, anthocyanins, pigments, and carotenoids, and to monitor the biotic and abiotic stress during the crop's life cycle [20,21]. Therefore, the HIS application has progressively become a very interesting tool to acquire data from a broad spatial scale within short intervals of time; especially in the remote sensing application with research aims and for rare industrial applications, e.g. the production of intelligent farming apps for the farmers aimed to

provide support for the use of fertilizers and the volume of the irrigation supply [22-24]. Nevertheless, the large-scale uses of application of the HIS remain not very widespread due to the cost of this kind of technology and the technical difficulties in hyperspectral data processing [25].

Since the early 2000s, a new generation of low-cost portable hyperspectral cameras (PHCs) has been progressively developed, increasing the possibilities of hyperspectral applications during research activities because of their minor cost, higher versatility and easiness of application than the HST installed on satellite or airborne platforms, and their ability to acquire data with a super-high-spatial resolution (e.g., centimetric or sub-centimetric level) [25-27]. Indeed, PHCs can be installed on a ground-based platform or on an Unmanned Aerial Vehicle (UAV) permitting to acquire hyperspectral data on narrow temporal acquisition intervals on a defined area [27,28]. Overall, the low-cost devices reported the following characteristics: PHCs are composed of a frame detector to acquire spectral images into a specific field of view (FOV) expressed in degrees, which defines the spatial resolution of the instrument [26,29]; the spectral resolution is calculated by the Full Width at Half Maximum (FWHM) of the spectral sensor, where FWHM is defined as the width of a spectral band below which the signal would overlap [30]. PHC generally use a snapshot technology, .Imaging chip technology commonly found in the PHCs are Charged Coupled Devices (CCD) and Complementary Metal Oxide Semiconductors (CMOS). Both sensor types allow the acquisition of a million pixels in a single image with high spectral and spatial resolution. Nevertheless, CMOS sensors show higher sensitivity, low power consumption and low cost than CCD but also higher background noise and dark current presence [31]. Despite the technological developments of the low-cost PHCs, critical aspects are reported during acquisition and data processing, such as the long instrumental warm-up time, the presence of spectral discontinuities in correspondence of the spectral border region of different CMOS sensors, signal jumps, and high level of background noise [32-35].

In this work, the low-cost PHC Senop HSC-2 (HSC-2) and the Ocean Optics USB 2000 spectrometer (USB 2000, Ocean Insight, Rochester, NY, USA) with a VIS/NIR spectral range were used to collect hyperspectral data on a white reference and a vegetation target during multiple acquisitions conducted under controlled conditions during a phenotyping experiment. The spectral results obtained using the PHC and the spectrometer were compared and discussed. Subsequently, the PHC critical issues, such as signal jump and falls, background noise presence, and measurement limits due to the loss of sensitivity by

the CMOS sensors, were analysed and discussed. Based on the results, a novel hyperspectral correction methodology (HCM) suitable for all PHC and application fields was developed and tested to reduce the CMOS sensors' spectral jumps, background noise, and measurement limits.

1.2 - Materials and methods

1.2.1 Experimental activities

The work activities were conducted during the years 2020 and 2021 at CNR (National Research Council of Italy) in the facilities of Florence and Follonica (Italy), and in ALSIA (Agenzia Lucana di Sviluppo ed Innovazione in Agricoltura, S.S. Jonica Km 448,2, 75012 Metaponto MT) a node of the European Plant Phenotyping Network (EPPN) (<https://emphasis.plant-phenotyping.eu/>). The experimental activities, consisting of the simultaneous hyperspectral acquisitions on a reference and vegetation target, was conducted using the HSC-2 and the USB 2000 spectrometer.

1.2.2 Hyperspectral devices

The hyperspectral instruments used during this work were the USB 2000 spectrometer and the HSC-2. The description of the instruments is explained below:

Ocean Optics USB2000 spectrometer

The USB 2000 is a portable spectrometer able to collect continuous spectral information from a surface (figure 1). The USB 2000 is characterized by a spectral sampling interval ranging from 350 to 1000 nm with 0.2 nm of spectral resolution. The spectrometer is based on a Sony ILX511 linear silicon CCD array.

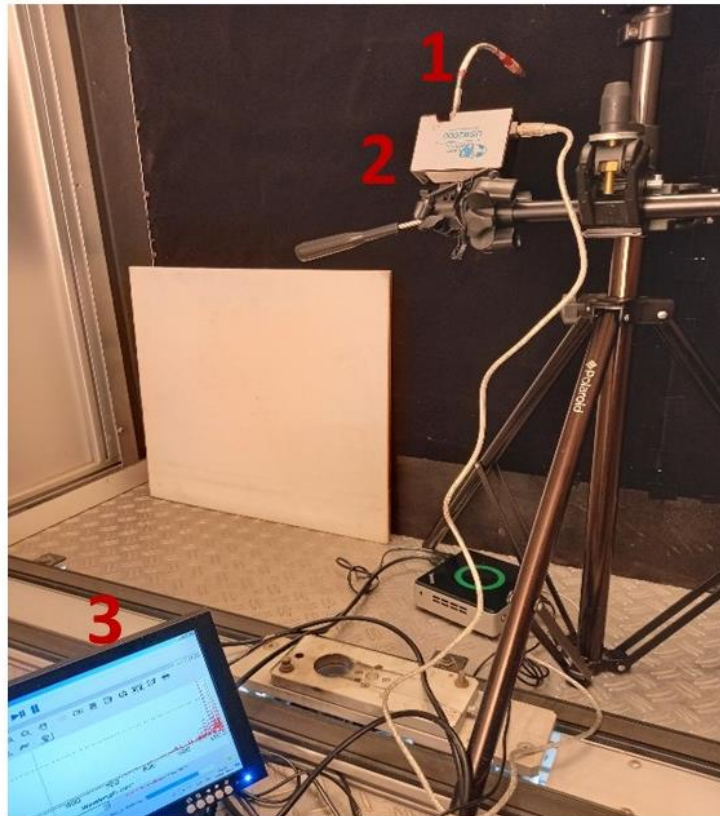


Figure 1. USB 2000 at working. The electromagnetic radiations are collected by an optical fiber (1) connected to the body of the spectrometer (2). The hyperspectral data can be visualized online using the Ocean View software (3) (Ocean Insight, Rochester, NY, USA). Further information can be found at the link of the instrument web page: <https://www.oceaninsight.com/globalassets/catalog-blocks-and-images/manuals--instruction-ocean-optics/spectrometer/usb2000-operating-instructions1.pdf>

Hyperspectral camera Senop HSC-2

The HSC-2 (figure 2) is a hyperspectral device with a VIS/NIR spectral range already used in research activities, e.g. the acquisition of high-resolution hyperspectral images acquired in flight by a UAV platform [28,35], to monitoring the plant health status through the detection of potassium concentration on leaves [36] and in biomedical applications, as the realisation on a pathological tissues database [37,38].



Figure 2. Hyperspectral camera HSC-2. Further information can be found at the link of the instrument web page <https://senop.fi/product/hsc-2-hyperspectral-camera-450-800nm/>.

The HSC-2 is a Frame Based Digital Hyperspectral camera equipped with a true global snapshot sensor (1) able to collect the entire 3-dimensional (3-D) data cube in a single integration period [46]. The snapshot sensor is composed of two separate CMOS sensors in the VIS and NIR spectral range from 400 to 1000 nm. The operator can set several acquisition parameters, such as spectral range and resolution. The hyperspectral device has a total weight of 990 grams, and it can be installed on a tripod (2) or an UAV DJI Matrice 600 drone & Ronin-MX gimbal [39]. The hyperspectral data, combined in a HC, were stored in an internal memory of one terabyte size. The instrument can transfer the hyperspectral data only using an ethernet cable (3). The hyperspectral data can be explored using the software Senop HIS-2 provided by the developers of HSC-2. The hyperspectral data can be visualised in radiance ($\text{mW}/\text{nm} \cdot \text{sr} \cdot \text{m}^2$) by using the Senop HIS-2 software. At the end of every acquisition, the HC derived was stored in a specific directory. The directory is composed of the HC and a header file consisting of all the metadata needed to use the spectral information contained in the HC, such as gain value to convert HC saved in DCs in the radiometric units, the FWHM for each band, the wavelengths, and the number of measurement bands.

The general specification for optics, image size and spectral capability of the instrument were reported in table 1.

Optics	Imaging capability	Spectral capability
FOV 36,8 degrees. Focus distance: 30cm to ∞ , limited FOV with less than 30cm distances.	Image frame size: 1024 x 1024 pixels.	Wavelength area: from 400 to 1000nm.

Table 1. Specification of the HSC-2.

1.2.3 The HCM

The HCM was based on a correction function (CF) specially designed and made to correct the radiance signal obtained using the HSC-2. The CF, called *importsenop*, was developed using MatlabR2021a (MahtWorks,USA). The workflow of the CF was reported in figure 3.

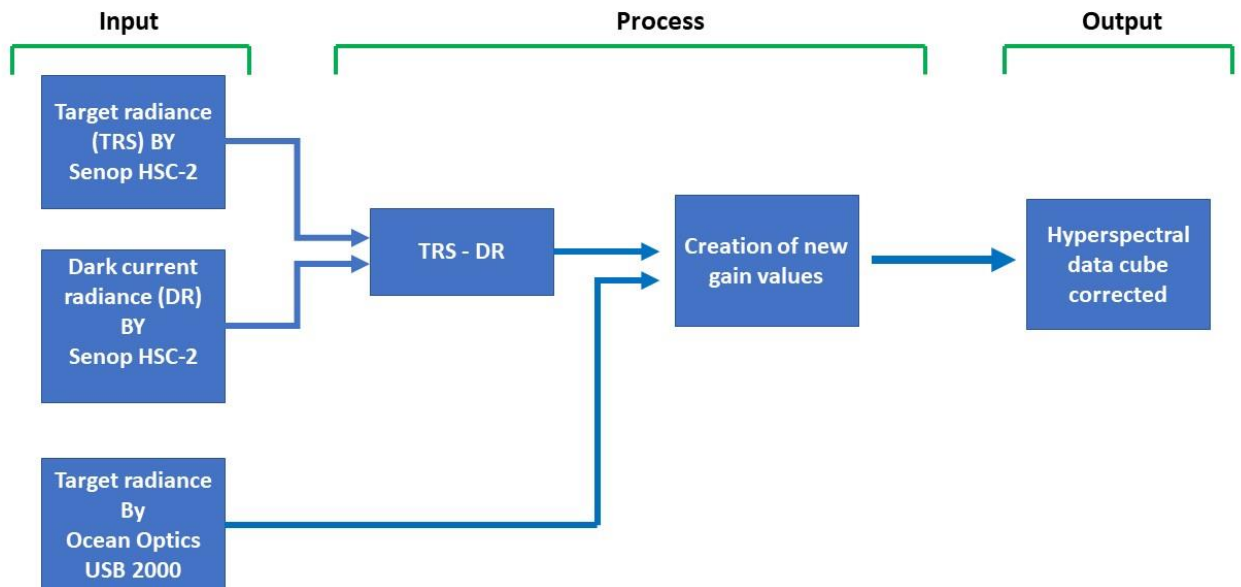


Figure 3. The architecture of the CF. The complete Matlab code of the CF is reported in section 1.5 of this chapter.

The function workflow was divided in three phases (figure 3): 1) the acquisition of the input data (input); 2) the data processing (process); 3) the generation of the output (output). The whole hyperspectral data organisation, elaboration and processing described in this work was completed using MatlabR2021a (MathWorks, USA).

Inputs

The function requires three inputs:

1- *The dark current obtained by HSC-2.* The dark current data were obtained with a hyperspectral acquisition in complete darkness condition. Therefore, the HSC-2 optic was covered entirely to obtain a total darkness. The resulting HC contains the background noise generated by the HSC-2 warming.

2- *The radiance obtained by the reference target using the USB 2000.* The hyperspectral data collected represent the true data of the radiance derived by the reference target.

3- *The target's radiance obtained by the hyperspectral camera HSC-2.*

Process

The HC derived by the HSC-2 acquisition is collected in DC units. Therefore, the conversion of HC in radiance units is needed to obtain a radiance output, and it was obtained in the following way:

$$R = DCvalues \times Ks \quad (1)$$

Where DC values are the DC value for each spectral band, and Ks are the gain value for each spectral band derived from the HSC-2 header file. Subsequently, the radiance of the HSC-2 was corrected and recalibrated using the new gain values generated by the novel CF developed here. The first operation is an automatic subtraction of the dark current values for each pixel to the corresponding pixel of the target; this operation is conducted for each spectral band (the spectral bands in the dark current HC must match with the spectral bands of the target HC). Subsequently, the function calculates the interpolated values between the radiance derived by the USB 2000 and the radiance obtained by the HSC-2 at the wavelengths reported in the HSC-2 header file using a linear interpolation. This operation is based on the Matlab function `interp1`. Subsequently, a 3-D signal filter was applied using a `medfilt3` Matlab function. The result is a new USB 2000 radiance at the HSC-2 wavelengths.

Outputs

The CF returns the Ks for each spectral band. The Ks is generated based on the radiance obtained by the truth data collected by the USB 2000. The new Ks is a numeric vector of 1 x n size, where n is the length of the original gain vector derived by the HSC-2 header file. The new Ks are automatically multiplied according to the formula (1).

The result is a new HC composed of the corrected radiance value for each spectral band. In addition, the function can be set to convert automatically the radiance obtained in reflectance as follows:

$$\text{Ref} = \text{Rad} / \text{RT} \quad (1)$$

Where Rad is the radiance obtained by the target and RT is the radiance obtained by the white reference target.

1.2.4 Test of the novel HCM

Acquisition setup

The efficiency of the correction methodology developed here was computed during an acquisition test. The acquisition setup used during the test was composed of an acquisition chamber (figure 4) based on the LemnaTec Scanalyzer 3D system (LemnaTec GmbH, Germany) [40]. A white Lambertian reference target with a 75% reflectance was posed in the acquisition chamber in a nadiral position compared to the light source. The light source comprised 120 Osram GmbH halogen lamps with a maximum level variation of 2%. Every lamp produced a net power of 35 Watts. The USB 2000 was posed a few inches from the reference with an angle of 45° to the reference target. During the acquisition process, the HSC-2 was installed at 1.50 meters from the white reference target, in a nadiral position compared to the target and light source. The exposure was set to 80 milliseconds for every spectral band. The HSC-2 underwent a warm-up time of 20 minutes to reduce the noisy effects.



Figure 4. The acquisition chamber was used in the experiment. In the image are visible the light source, the HSC-2 and a vegetation target in the background.

Dark current computation and analysis

The HSC-2 instrumental background noise trend, also called dark current, was computed through multiple acquisitions. One acquisition was conducted every 10 minutes for a total amount of 130 minutes, posing the optic of the hyperspectral camera in complete darkness condition. After every dark current acquisition, the white reference target was immediately acquired. The dark current and reference trends were processed as the mean value of the HSC-2 full spectrum, expressed in DC units. Finally, the dark current and reference trends were compared to deduce the inference of the dark current to the resulting reference radiance.

Test on a white reference target

The HCM was tested on a white reference target yet described. The reference target was acquired using the HSC-2 and the USB 2000. The HSC-2 was set with a spectral range from 450 to 950 nm for 203 spectral bands. Subsequently, the trend of the radiance

obtained using the USB 2000 was compared to the HSC-2 radiance trend computed using the original gain values reported in the header file. The two trend results were compared to the trend of the HSC-2 radiance obtained using the correction methodology developed here.

Test on a vegetation target

The HCM was also tested on a vegetation target. A maize plant was posed in the acquisition chamber organised with the acquisition setup yet described, and a hyperspectral acquisition was conducted using the HSC-2. The hyperspectral camera was set to its maximum spectral range, from 400 to 1000 nm, for a total amount of 203 spectral bands.

The hyperspectral data obtained at the end of the acquisition process was processed to obtain three outputs:

- i) The HC computed in DC units.
- ii) The HC computed in radiance units, obtained using the original gain values reported in the HSC-2 header file.
- iii) The HC computed in radiance units obtained using the novel CF.

Finally, the results obtained by the three different processes ways were compared and discussed.

1.3 - Results and discussions

1.3.1 Signal noise computation and characterization

The dark current values were obtained and results are shown in figure 5.

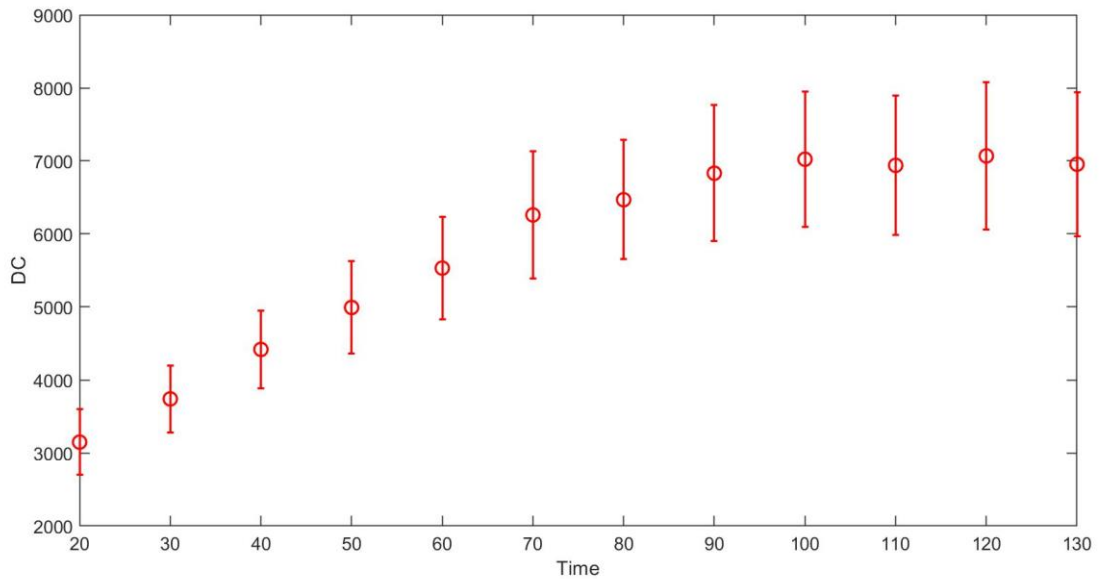


Figure 5. Mean of the dark current values expressed in DC (counts) units for a region of interest (ROI) with a size of 100 x 100 pixels, for a total of 203 spectral bands from 400 to 1000 nm. The values were obtained during a time range from 20 to 130'. The first 20' were dedicated to the instrument warm-up, and the data were not reported. The standard deviation was reported.

The dark current value constantly increases for the first 90' of the acquisition, showing an increase of up to double the initial dark current value. Indeed, at the start of the experiment a dark value near 3000 counts was registered, while at the end of the experiment was registered a dark value near 7000 counts highlighting a long warm-up time. The warm-up time appears variable between hyperspectral cameras; e.g. Zhu et al. [33] have reported 30' as sufficient warm-up time by the “GaiaSorter” HSI system produced by Zolix Co., Ltd. (Beijing, China). The HSC-2 has shown a warm-up time of over 90 minutes. The dark current appears stable from 90 minutes to the start to the end of the experiment.

The spectral signature of the dark current was computed, and the result was reported in Figure 6.

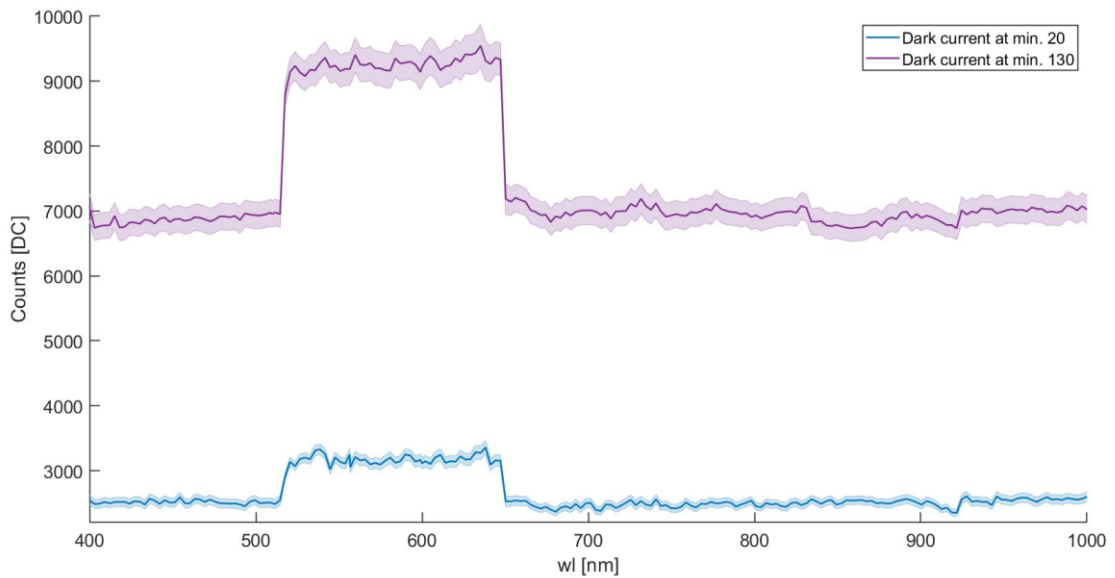


Figure 6. Example of the dark current spectral signature obtained at 20 and 130 minutes. The spectral signature (reported in DC) was obtained by processing the signal for each spectral band, and the result was obtained by the mean of an HI with 1024 x 1024 pixel size (HSC-2 full spatial resolution). The standard deviation was reported.

The spectral signature show three spectral regions (from 400 to 513 nm, from 513 to 650 nm, and from 650 to 1000 nm, respectively) divided by two spectral jumps at 513 and 650 nm. The spectral region from 400 to 513 nm shows a mean of 2000 counts at 20' and a standard deviation of 250 counts, while it shows a mean of 6900 counts and a standard deviation near 500 counts at 130'. The spectral region from 513 to 650 nm shows a mean of 3100 counts at 20' with a standard deviation of 250 counts. The spectral region from 650 to 1000 nm shows a mean of 2000 counts, reporting standard deviation values of 250 counts. The spectral signature reported spectral jumps at 513 and 650 nm and a lower spectral jump at 930 nm. Overall, the maximum dark current values were reported in the spectral regions from 513 to 650 nm on the VIS edge. The HI obtained from the three spectral regions was reported in figure 7.

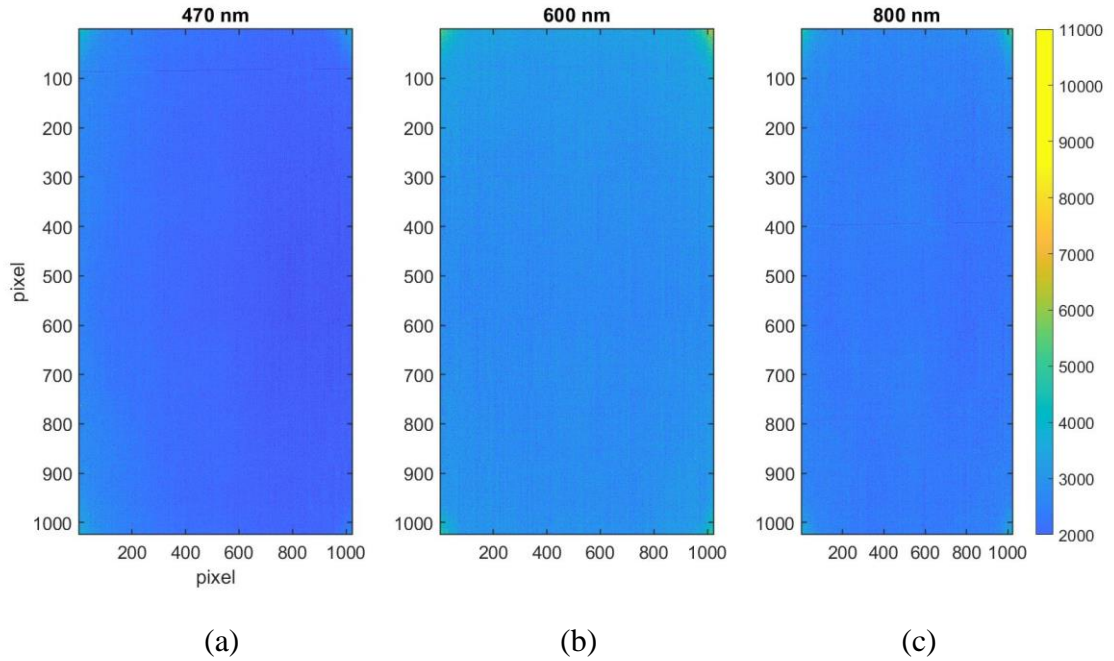


Figure 7. HIs obtained by a dark current acquisition collected after 20' from the start of the experiment. The HIs were acquired from the three spectral regions at 470 (a), 600 (b), and 800 nm (c). The HIs were obtained with 1024 x 1024 pixel size (HSC-2 full spatial resolution), and each pixel shows a DC level evidenced by the colour bar.

Results show differences between HIs regarding sharpness, uniformity and background noise level. Subfigure b shows higher DC values and lower uniformity of the pixel's DC values than subfigures a and c in with results obtained in figure 6. Figure b shows higher levels of background noise than figures a and c reporting image discontinuities highlighted by vertical stripes. The HIs obtained at 470 and 80 nm (Figures 7, a and c) show higher image sharpness and uniformity compared to the HI at 600 nm. The HI at 470 nm (figure 7, a) shows a decrease in the DC level from the left to the right side of the image (from light blue to dark blue). Generally, the HI at 800 nm appears more uniform than the HIs at 470 and 600 nm. The lower image uniformity in the edge spectral regions and the spectral jumps at 513 and 650 nm evidenced a loss of sensitivity by the two CMOS sensors, compromising the acquisition of sharpnesses HIs in the edge spectral regions [31].

A white reference target was acquired simultaneously with the dark current acquisitions, and results are shown in figure 8.

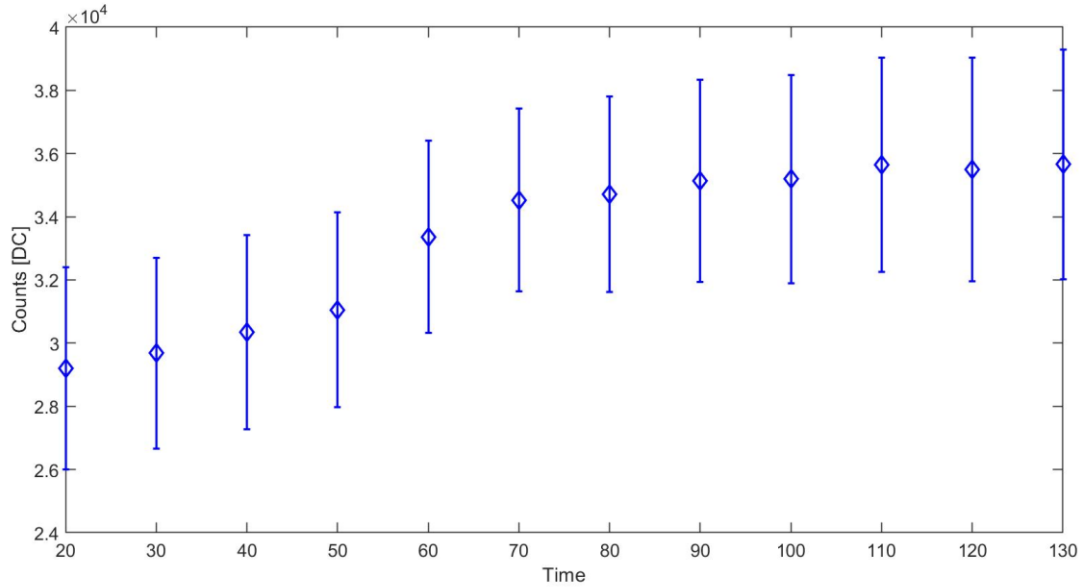


Figure 8. Mean of the white reference target expressed in DC (counts) units for a ROI of 100 x 100 pixels pixel size, for a total of 203 spectral bands from 400 to 1000 nm. The ROI was overlapped with the ROI analysed in figure 5. The standard deviation was reported.

The DC values obtained by a white reference target constantly increased for the first 90 minutes of the acquisition, according to the results obtained in Figure 5. Indeed, from 20 to 90 minutes, a progressive increment of the magnitude of the DC values was reported. The similar trend between Figure 5 and Figure 8 is due to the effect of the background noise to the signal magnitude; therefore, considering the dark current trend and its direct proportionality to the warm-up time is essential to obtain a clean spectral signal [32,33]. Based on the results, the dark current changes its value for each pixel and wavelength and must be overlapped to the target and subtracted pixel by pixel and wavelength by wavelength. Therefore, a dark current subtraction from the target image is recommended for warm-up times under 90', considering the rapid changes in the dark current values and background noise level.

1.3.2 HCM test results

The spectral datasets were collected from the white reference and vegetation target by the USB 2000 and the HSC-2. Subsequently, the CF was applied on the two hyperspectral datasets.

Application of the HCM on a white reference target

The light reflected by the white reference target was acquired using the HSC-2 and the USB 2000. The respective radiances were computed using the original gain values and new the gain values obtained using the CF. Results are shown in figure 9.

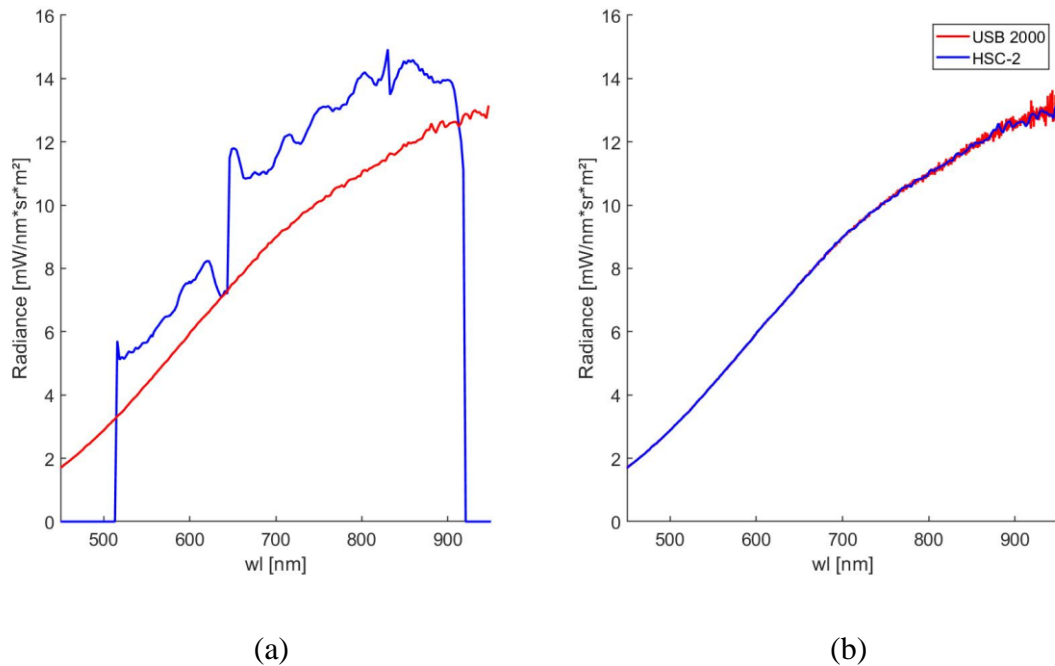


Figure 9. The figure shows the USB 2000 and HSC-2 radiances (mW/nm*sr*m²). Plot a show of the two radiances before applying the CF on the HSC-2 spectral signature. Plot b shows the two radiances after using the CF on the HSC-2 spectral signature.

The USB 2000 and the HSC-2 radiances before the application of the CF showed differences in trend and magnitude. The light spectrum obtained using the USB 2000 appears linear and homogeneous, reproducing a halogen lamp's characteristic light spectrum which shows a steady increase from VIS to NIR [41]. Instead, the radiance obtained using the HSC-2 shows several magnitudes jumps and falls compared to the USB 2000 radiance. In the spectral region from 450 to 515 nm, the HSC-2 radiance equals zero as in the spectral region from 920 to 950 nm (plot a, blue radiance). This result is due to the gain values automatically generated by HSC-2, which are equal to zero in the same spectral regions. Two radiance jumps are shown around 650 nm and 830 nm. In addition, the spectral region from 650 to 830 appears noisy and characterised by fluctuations compared to the radiance obtained using the USB 2000.

After applying the correction methodology, the HSC-2 radiance appears similar to the USB 2000 radiance, as shown in plot (b). Results show the CF's ability to overcome the DC to radiance conversion limits due to the gain value generated in the HSC-2 header file.

Application of the HCM on a vegetation target

The correction methodology was tested on a vegetation target. The spectral signatures were computed in DC and radiance ($\text{mW}/\text{nm} \cdot \text{sr} \cdot \text{m}^2$). Radiance results were obtained by applying the gain values derived by the hyperspectral camera header file and using the gain values obtained by the CF here developed.

Results are shown in Figure 10.

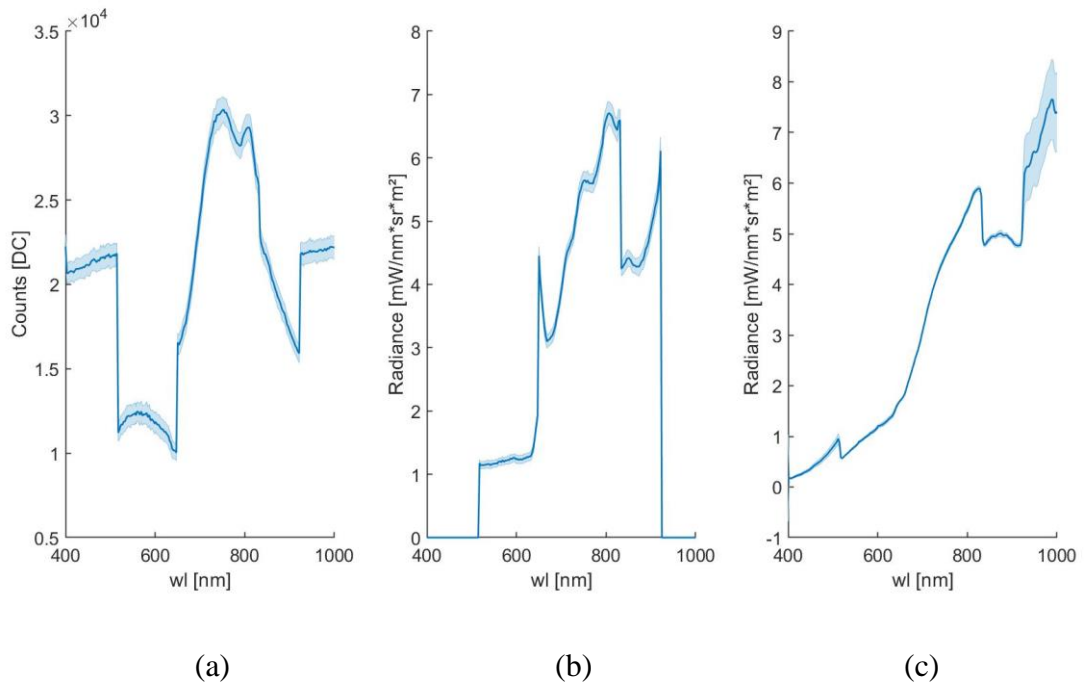


Figure 10. Three spectral signatures obtained by the same ROI (11 x 11 pixels, for a total of 121 pixels) chosen from a leaf in a nadiral position compared to the light source and the optic of the HSC-2. The spectral signatures were reported as following: 1) as DC (plot a) automatically generated by HSC-2. 2) As radiance ($\text{mW}/\text{nm} \cdot \text{sr} \cdot \text{m}^2$) obtained using the gain values in the HSC-2 header file (plot b). 3) As radiance ($\text{mW}/\text{nm} \cdot \text{sr} \cdot \text{m}^2$) obtained applying the novel CF (plot c). The spectral data were acquired from 400 to 1000 nm, using the full spectral range of the HSC-2. The standard deviation was reported.

The spectral results in DC units (plot a) showed signal stability in the spectral range from 400 to 513 nm, where DC values near 2×10^4 were reported. The signal magnitude decreased at 1×10^4 DC in the spectral region from 513 to 650 nm, showing a plateau of the spectral signal. The DC results (plot a) showed a signal fall at 513 nm. The shape of the spectral signal showed an increment in slope in the spectral region from 650 to 820 nm, in accordance with Chen et al. and Cordon et al., which evidenced a slope increment in the red-edge spectral region on a vegetation target due to photochemical processes [3,42]. A constant DC values decrement is reported in the spectral region from 820 to 930 nm. The DC results showed an anomaly in the signal trend at 930 nm, where the DC values jump from 1.5×10^4 to 2.1×10^4 . Subsequently, a signal flattening was observed from 620 to 1000 nm in the right margin of the spectral signature. Signal falls and jumps are shown at 513, 650 and 930 nm due to the management of the two CMOS sensors in the VIS and NIR spectral range, highlighting one of the main limits of the low-cost PHC based on the CMOS technology [31,32,43].

The radiance results obtained using the gain value provided by the HSC-2 header file are shown in plot b. The radiance values are equal to zero from 400 to 513 nm, and this result is due to the gain values automatically generated by HSC-2, which are equal to zero from 400 to 513 nm and from 920 to 1000 nm, according to the results described in the previous paragraph. The motivation behind the automatic generation of a gain value equal to zero in the spectral regions mentioned remains to be determined, and the HSC-2 producer still needs to explain this. However, the poor sensitivity of the two CMOS sensors in the margins sides of the VIS and NIR spectral regions, highlighted by the DC results from 400 to 513 nm and from 920 to 1000, represents a plausible hypothesis of this choice adopted by the HSC-2 developers. The radiance results show a plateau in the spectral range from 513 to 650 nm (plot b) before the slope increment in the red-edge spectral region, as described in plot a. Generally, the spectral discontinuities highlighted in plot a are not reduced by radiance conversion obtained using the gain values automatic generated in the header file.

The spectral results obtained by applying the novel CF are shown in plot c. The first result obtained by application of the CF was the production of nonzero radiance values in the two spectral ranges from 400 to 513 and 920 to 1000 nm. The radiance trend obtained by the application of the CF, compared to plot b, showed a peak near 500 nm in correspondence with the pigment's absorption spectral regions, in accordance with the spectral leaf pigments analysis results (e.g. chlorophylls, carotenoids and anthocyanins)

reported in the literature [44-46]. Nevertheless, the peak highlighted appears weak and not very sharp, probably showing a measurement limit due to the CMOS VIS sensor previously hidden by the gain value in the HSC-2 header file (imposed equal to zero). The application of the CF has permitted us to obtain a clearer spectral signal due to a noise reduction compared to the results shown in plot b. Indeed, the spectral signal has reported lower fluctuations and more stability than the results obtained using the gain value generated by the header file. Generally, the standard deviation in plot c is lower than plots a and plot b, and the application of the CF has reported a reduction of the noise effects in the spectral signature compared to the results obtained using the gain values automatic generated in the header file. Finally, the CF here developed has significantly reduced the radiance falls and jumps due to the operation limits of the two CMOS sensors near 650 nm and 820 nm, improving the precision and reliability of the low-cost PHC here tested.

1.4 – Conclusions

This work presents a novel methodology to improve the performance of a low-cost PHC. The performance of the PHC HSC-2 were explored and tested through hyperspectral acquisitions conducted on a white reference and a vegetation target under controlled conditions of light and acquisition set. The spectral results obtained by the HSC-2 were compared with the spectral results obtained by the USB 2000. Subsequently, a novel HCM was successfully developed and tested. Therefore, the conclusions of this study are:

- i) A low-cost PHC can be a powerful tool in hyperspectral applications. However, the poor sensitivity of the two CMOS sensors in the margin's sides of the VIS/NIR spectral regions, from 400 to 513 and from 920 to 1000 nm, contributed to reducing the performance of the PHC. In addition, several signal gaps as falls and jumps were identified across the spectral signatures near 513, 650, and 930 nm.
- ii) The background noise increases over time. Therefore, the instrument's warm-up time must be considered and applying an image correction based on the background noise trend is strongly recommended to obtain a clean spectral signal.
- iii) The HCM developed in this work significantly improves the qualities of the spectral output obtained using the PHC HSC-2. Indeed, the radiance fall and jumps, and the signal noise were reduced, especially in the spectral region from 650 to 830 nm. Finally, the methodology developed here opens new ways for the other research communities which

use low-cost hyperspectral technologies, e.g. soil composition retrieval, for the study of materials properties, for medical application developments and ecosystem monitoring. Finally, the hyperspectral low-cost camera Senop HSC-2 was applied to a phenotyping experiment, as described in the next chapter.

1.5 Attachments

The novel CF “importsenop” (Matlab code).

Import and correction using new gain value of the Senop HSC-2 hypercube

```
% "Import Senop" - A.Genangeli
%M = counts hypercube
% D = counts dark
% R = radiance reference(spectroradiometer)
% ROIy = roy reference in y axes
% ROIx = roy reference in x axes
% you must have 1 hdr file in your folder
function [reflectance,radiance,dat,dark] = importsenop(M,D,x,ROIy,ROIx)
h = dir('*hdr');
myfilename = [h.name];
HDR = importdata(myfilename);
wl_senop = HDR(13,:);
wl_senop = regexp(wl_senop,'d+[\.]?d*','match');
wl_senop = wl_senop{1, 1};
wl_senop = wl_senop';
wl_senop = str2double(wl_senop);
bands = HDR(11,:);
bands = regexp(bands,'d+[\.]?d*','match','once');
bands = str2double(bands);
gain = HDR(15,:);
gain = regexp(gain,'d+[\.]?d*','match');
gain = gain{1, 1};
gain = gain';
gain = str2double(gain);
```

```

dat = multibandread(sprintf(M),[1024 1024 bands ],'uint16',0,'bsq','ieee-be');
dark = multibandread((D),[1024 1024 bands ],'uint16',0,'bsq','ieee-be');
x = load(x);
x = struct2array(x);
F = (dat(:,:))- (dark(:,:));
Froi = F(ROIy,ROIx,:);
Fraction = reshape(Froi,[],bands);
FROI = mean(Fraction,1)';
wl_ocean = x(:,1);
radocean = x(:,2);
newradocean = interp1(wl_ocean,radocean,wl_senop);
newgain = ( newradocean./FROI)*100;
refroi = FROI.*newgain;
for i = 1 : bands
    radiance(:,i) = newgain(i,1)*F(:,i);
end
radiance = medfilt3(radiance);
for i = 1 : bands
    reflectance(:,i) = radiance(:,i)./refroi(i,1);
end
end

```


References

1. Weiss, M., F. Jacob, and G. Duveiller. 'Remote Sensing for Agricultural Applications: A Meta-Review'. *Remote Sensing of Environment* 236 (1 January 2020): 111402. <https://doi.org/10.1016/j.rse.2019.111402>
2. Pham, Tien Dat, Naoto Yokoya, Dieu Tien Bui, Kunihiko Yoshino, and Daniel A. Friess. 'Remote Sensing Approaches for Monitoring Mangrove Species, Structure, and Biomass: Opportunities and Challenges'. *Remote Sensing* 11, no. 3 (January 2019): 230. <https://doi.org/10.3390/rs11030230>
3. Chen, Yun, Juan P Guerschman, Zhibo Cheng, and Longzhu Guo. 'Remote Sensing for Vegetation Monitoring in Carbon Capture Storage Regions: A Review'. *Applied Energy* 240 (15 April 2019): 312–26. <https://doi.org/10.1016/j.apenergy.2019.02.027>
4. Schneising, Oliver, Michael Buchwitz, Maximilian Reuter, Steffen Vanselow, Heinrich Bovensmann, and John P. Burrows. 'Remote Sensing of Methane Leakage from Natural Gas and Petroleum Systems Revisited'. *Atmospheric Chemistry and Physics* 20, no. 15 (3 August 2020): 9169–82. <https://doi.org/10.5194/acp-20-9169-2020>
5. Belkin, Igor M. 'Remote Sensing of Ocean Fronts in Marine Ecology and Fisheries'. *Remote Sensing* 13 no. 5 (January 2021): 883. <https://doi.org/10.3390/rs13050883>
6. Sishodia, Rajendra P., Ram L. Ray, and Sudhir K. Singh. 'Applications of Remote Sensing in Precision Agriculture: A Review'. *Remote Sensing* 12, no. 19 (January 2020): 3136. <https://doi.org/10.3390/rs12193136>
7. Genangeli, Andrea, Giorgio Allasia, Marco Bindi, Claudio Cantini, Alice Cavaliere, Lorenzo Genesio, Giovanni Giannotta, Franco Miglietta, and Beniamino Gioli. 'A Novel Hyperspectral Method to Detect Moldy Core in Apple Fruits'. *Sensors* 22, no. 12 (January 2022): 4479. <https://doi.org/10.3390/s22124479>
8. Raj, Rahul, Jeffrey P. Walker, Vishal Vinod, Rohit Pingale, Balaji Naik, and Adinarayana Jagarlapudi. 'Leaf Water Content Estimation Using Top-of-Canopy Airborne Hyperspectral Data'. *International Journal of Applied Earth Observation and Geoinformation* 102 (1 October 2021): 102393. <https://doi.org/10.1016/j.jag.2021.102393>
9. Yendrek, Craig R., Tiago Tomaz, Christopher M. Montes, Youyuan Cao, Alison M. Morse, Patrick J. Brown, Lauren M. McIntyre, Andrew D.B. Leakey, and Elizabeth A. Ainsworth. 'High-Throughput Phenotyping of Maize Leaf Physiological and

- Biochemical Traits Using Hyperspectral Reflectance'. *Plant Physiology* 173, no. 1 (January 2017): 614–26. <https://doi.org/10.1104/pp.16.01447>
10. Lv, Zhiyong, Fengjun Wang, Guoqing Cui, Jón Atli Benediktsson, Tao Lei, and Weiwei Sun. 'Spatial–Spectral Attention Network Guided With Change Magnitude Image for Land Cover Change Detection Using Remote Sensing Images'. *IEEE Transactions on Geoscience and Remote Sensing* 60 (2022): 1–12. <https://doi.org/10.1109/TGRS.2022.3197901>
 11. Wu, Qiong, Ruofei Zhong, Wenji Zhao, Kai Song, and Liming Du. 'Land-Cover Classification Using GF-2 Images and Airborne Lidar Data Based on Random Forest'. *International Journal of Remote Sensing* 40, no. 5–6 (19 March 2019): 2410–26. <https://doi.org/10.1080/01431161.2018.1483090>
 12. Qiao, Mengjia, Xiaohui He, Xijie Cheng, Panle Li, Haotian Luo, Lehan Zhang, and Zhihui Tian. 'Crop Yield Prediction from Multi-Spectral, Multi-Temporal Remotely Sensed Imagery Using Recurrent 3D Convolutional Neural Networks'. *International Journal of Applied Earth Observation and Geoinformation* 102 (1 October 2021): 102436. <https://doi.org/10.1016/j.jag.2021.102436>
 13. Abad-Segura, Emilio, Mariana-Daniela González-Zamar, Esteban Vázquez-Cano, and Eloy López-Meneses. 'Remote Sensing Applied in Forest Management to Optimize Ecosystem Services: Advances in Research'. *Forests* 11, no. 9 (September 2020): 969. <https://doi.org/10.3390/f11090969>
 14. 'Multi- and Hyperspectral Geologic Remote Sensing: A Review | Elsevier Enhanced Reader'. Accessed 28 November 2022. <https://doi.org/10.1016/j.jag.2011.08.002>
 15. Stuart, Mary B., Andrew J. S. McGonigle, and Jon R. Willmott. 'Hyperspectral Imaging in Environmental Monitoring: A Review of Recent Developments and Technological Advances in Compact Field Deployable Systems'. *Sensors* 19, no. 14 (January 2019): 3071. <https://doi.org/10.3390/s19143071>
 16. Cen, Yi, Ying Huang, Shunshi Hu, Lifu Zhang, and Jian Zhang. 'Early Detection of Bacterial Wilt in Tomato with Portable Hyperspectral Spectrometer'. *Remote Sensing* 14, no. 12 (January 2022): 2882. <https://doi.org/10.3390/rs14122882>
 17. Benelli, Alessandro, Chiara Cevoli, and Angelo Fabbri. 'In-Field Hyperspectral Imaging: An Overview on the Ground-Based Applications in Agriculture'. *Journal of Agricultural Engineering* 51, no. 3 (29 September 2020): 129–39. <https://doi.org/10.4081/jae.2020.1030>

18. Dixit, Yash, Mahmoud Al-Sarayreh, Cameron Craigie, and Marlon M. Reis. 'A Rapid Method of Hypercube Stitching for Snapshot Multi-Camera System'. In 2020 35th International Conference on Image and Vision Computing New Zealand (IVCNZ), 1–6, 2020. <https://doi.org/10.1109/IVCNZ51579.2020.9290723>
19. Kotawadekar, Rahul. '9 - Satellite Data: Big Data Extraction and Analysis'. In Artificial Intelligence in Data Mining, edited by D. Binu and B. R. Rajakumar, 177–97. Academic Press, 2021. <https://doi.org/10.1016/B978-0-12-820601-0.00008-2>
20. Deshmukh, Ratnadeep, Suresh Mehrotra, and Sachin Deshmukh. 2nd International Conference on Knowledge Engineering, 2016. https://scholar.google.com/scholar?hl=it&as_sdt=0%2C5&q=vegetation+idicies+review&btnG=
21. Palanisamy, Shanmugapriya, Rathika Selvaraj, Thanakkan Ramesh, and Janaki Ponnusamy. 'Applications of Remote Sensing in Agriculture - A Review'. International Journal of Current Microbiology and Applied Sciences 8 (20 January 2019): 2270–83. <https://doi.org/10.20546/ijcmas.2019.801.238>
22. Migdall, Silke, Philipp Klug, Antoine Denis, and Heike Bach. 'The Additional Value of Hyperspectral Data for Smart Farming'. In 2012 IEEE International Geoscience and Remote Sensing Symposium, 7329–32, 2012. <https://doi.org/10.1109/IGARSS.2012.6351937>
23. Inoue, Yoshio. 'Satellite- and Drone-Based Remote Sensing of Crops and Soils for Smart Farming – a Review'. Soil Science and Plant Nutrition 66, no. 6 (1 November 2020): 798–810. <https://doi.org/10.1080/00380768.2020.1738899>
24. Said Mohamed, Elsayed, AA. Belal, Sameh Kotb Abd-Elmabod, Mohammed A El-Shirbeny, A. Gad, and Mohamed B Zahran. 'Smart Farming for Improving Agricultural Management'. The Egyptian Journal of Remote Sensing and Space Science 24, no. 3, Part 2 (1 December 2021): 971–81. <https://doi.org/10.1016/j.ejrs.2021.08.007>
25. Lu, Bing, Phuong D. Dao, Jianguai Liu, Yuhong He, and Jiali Shang. 'Recent Advances of Hyperspectral Imaging Technology and Applications in Agriculture'. Remote Sensing 12, no. 16 (January 2020): 2659. <https://doi.org/10.3390/rs12162659>
26. Bolton, Frank J., Amir S. Bernat, Kfir Bar-Am, David Levitz, and Steven Jacques. 'Portable, Low-Cost Multispectral Imaging System: Design, Development, Validation, and Utilization'. Journal of Biomedical Optics 23, no. 12 (December 2018): 121612. <https://doi.org/10.1117/1.JBO.23.12.121612>

27. Jung, András, Michael Vohland, and Sören Thiele-Bruhn. 'Use of A Portable Camera for Proximal Soil Sensing with Hyperspectral Image Data'. *Remote Sensing* 7, no. 9 (September 2015): 11434–48. <https://doi.org/10.3390/rs70911434>
28. Di Gennaro, Salvatore Filippo, Piero Toscano, Matteo Gatti, Stefano Poni, Andrea Berton, and Alessandro Matese. 'Spectral Comparison of UAV-Based Hyper and Multispectral Cameras for Precision Viticulture'. *Remote Sensing* 14, no. 3 (January 2022): 449. <https://doi.org/10.3390/rs14030449>
29. Fan, Xinghao, Chunyu Liu, Shuai Liu, Yunqiang Xie, Liangliang Zheng, Tiancong Wang, and Qinqing Feng. 'The Instrument Design of Lightweight and Large Field of View High-Resolution Hyperspectral Camera'. *Sensors* 21, no. 7 (January 2021): 2276. <https://doi.org/10.3390/s21072276>
30. Xie, Mingliang, Mizhen Sun, Shanfeng Xue, and Wenjun Yang. 'Recent Progress of Blue Fluorescent Organic Light-Emitting Diodes with Narrow Full Width at Half Maximum'. *Dyes and Pigments* 208 (1 December 2022): 110799. <https://doi.org/10.1016/j.dyepig.2022.110799>
31. RadhaKrishna, M. V. V., M. Venkata Govindh, and P. Krishna Veni. 'A Review on Image Processing Sensor'. *Journal of Physics: Conference Series* 1714, no. 1 (January 2021): 012055. <https://doi.org/10.1088/1742-6596/1714/1/012055>
32. Tommaselli, A.M.G.; Santos, L.D.; Berveglieri, A.; Oliveira, R.A.; Honkavaara, E. A study on the variations of inner orientation parameters of a hyperspectral frame camera. *Int. Arch. Photogramm. Remote Sens. Spat. Inf. Sci.* 2018, XLII–1, 429–436. <https://doi.org/10.5194/isprs-archives-XLII-1-429-2018>
33. Zhu, Jingwu, Hao Li, Zhenhong Rao, and Haiyan Ji. 'Identification of Slightly Sprouted Wheat Kernels Using Hyperspectral Imaging Technology and Different Deep Convolutional Neural Networks'. *Food Control* 143 (1 January 2023): 109291. <https://doi.org/10.1016/j.foodcont.2022.109291>
34. Ji, Yamin, Laijun Sun, Yingsong Li, Jie Li, Shuangcai Liu, Xu Xie, and Yuantong Xu. 'Non-Destructive Classification of Defective Potatoes Based on Hyperspectral Imaging and Support Vector Machine'. *Infrared Physics & Technology* 99 (1 June 2019): 71–79. <https://doi.org/10.1016/j.infrared.2019.04.007>
35. Chan, Yee Kit, Voon Chet Koo, Edmund Hou Kheat Choong, and Chee Siong Lim. 'The Drone Based Hyperspectral Imaging System for Precision Agriculture'. *NVEO - NATURAL VOLATILES & ESSENTIAL OILS Journal* | NVEO, 20 November 2021, 5561–73. <https://www.nveo.org/index.php/journal/article/view/1703>

36. ABENINA, Megan Io Ariadne S., et al. Application of Principal Component Analysis to Hyperspectral Data for Potassium Concentration Classification on Peach leaves. In: 2022 ASABE Annual International Meeting. American Society of Agricultural and Biological Engineers, 2022. p. 1. <https://doi.org/10.13031/aim.202200490>
37. Lehtonen, Samu J. R., Hana Vrzakova, Jussi J. Paterno, Sami Puustinen, Roman Bednarik, Markku Hauta-Kasari, Hideaki Haneishi, et al. 'Detection Improvement of Gliomas in Hyperspectral Imaging of Protoporphyrin IX Fluorescence – in Vitro Comparison of Visual Identification and Machine Thresholds'. *Cancer Treatment and Research Communications* 32 (1 January 2022): 100615. <https://doi.org/10.1016/j.ctarc.2022.100615>
38. Puustinen, Sami, Joni Hyttinen, Gemal Hisuin, Hana Vrzáková, Antti Huotarinen, Pauli Fält, Markku Hauta-Kasari, et al. 'Towards Clinical Hyperspectral Imaging (HSI) Standards: Initial Design for a Microneurosurgical HSI Database'. In 2022 IEEE 35th International Symposium on Computer-Based Medical Systems (CBMS), 394–99, 2022. <https://doi.org/10.1109/CBMS55023.2022.00077>
39. Horstrand, Pablo, Raúl Guerra, Aythami Rodríguez, María Díaz, Sebastián López, and José Fco. López. 'A UAV Platform Based on a Hyperspectral Sensor for Image Capturing and On-Board Processing'. *IEEE Access* 7 (2019): 66919–38. <https://doi.org/10.1109/ACCESS.2019.2913957>
40. Janni, Michela, Nicola Coppede, Manuele Bettelli, Nunzio Briglia, Angelo Petrozza, Stephan Summerer, Filippo Vurro, et al. 'In Vivo Phenotyping for the Early Detection of Drought Stres in Tomato'. *Plant Phenomics* 2019 (27 November 2019). <https://doi.org/10.34133/2019/6168209>
41. Tawfik, M., X. Tonnellier, and C. Sansom. 'Light Source Selection for a Solar Simulator for Thermal Applications: A Review'. *Renewable and Sustainable Energy Reviews* 90 (1 July 2018): 802–13. <https://doi.org/10.1016/j.rser.2018.03.059>
42. Cordon, Gabriela, Carolina Andrade, Lucía Barbara, and Ana María Romero. 'Early Detection of Tomato Bacterial Canker by Reflectance Indices'. *Information Processing in Agriculture* 9, no. 2 (1 June 2022): 184–94. <https://doi.org/10.1016/j.inpa.2021.06.004>
43. Hagen, Nathan A., Liang S. Gao, Tomasz S. Tkaczyk, and Robert T. Kester. 'Snapshot Advantage: A Review of the Light Collection Improvement for Parallel High-Dimensional Measurement Systems'. *Optical Engineering* 51, no. 11 (June 2012): 111702. <https://doi.org/10.1117/1.OE.51.11.111702>

44. Walsh, Kerry B., José Blasco, Manuela Zude-Sasse, and Xudong Sun. ‘Visible-NIR “Point” Spectroscopy in Postharvest Fruit and Vegetable Assessment: The Science behind Three Decades of Commercial Use’. *Postharvest Biology and Technology* 168 (1 October 2020): 111246. <https://doi.org/10.1016/j.postharvbio.2020.111246>
45. Gitelson, Anatoly, Alexei Solovchenko, and Andrés Viña. ‘Foliar Absorption Coefficient Derived from Reflectance Spectra: A Gauge of the Efficiency of in Situ Light-Capture by Different Pigment Groups’. *Journal of Plant Physiology* 254 (1 November 2020): 153277. <https://doi.org/10.1016/j.jplph.2020.153277>
46. Gitelson, Anatoly, and Alexei Solovchenko. ‘Non-Invasive Quantification of Foliar Pigments: Possibilities and Limitations of Reflectance- and Absorbance-Based Approaches’. *Journal of Photochemistry and Photobiology B: Biology* 178 (1 January 2018): 537–44. <https://doi.org/10.1016/j.jphotobiol.2017.11.023>

Chapter two

Low-cost hyperspectral imaging to detect drought stress in high-throughput phenotyping

Premise

The contents of this chapter was submitted as a journal paper to the journal “*Plants*” (Manuscript ID- 2331860) in special issue "From Genome to Phenome: A Bridge to Accelerate Adaptation of Crops to Abiotic Stress". The journal homepage and the special issue identified for the submission are available here:

https://www.mdpi.com/journal/plants/special_issues/genome_phenome_crops

2.1 – Introduction

Global population is projected to reach 9.8 billion in the year 2050, generating a growing demand in food production [1,2]. The global agricultural sector is facing growing risks associated to more frequent extreme meteorological events [3,4], able to undermine the classic cultivars commonly used in food production. The direct consequence of this phenomenon is a loss in terms of quantity and quality of productions and a loss of security [5-7]. Indeed, from 2008-2018, the loss of production at regional scale caused by precipitation events, above-average temperature and other anomalous weather events, was estimated at around 8% of the yearly total for an overall value of 116.7 billion dollars [8-12]. The need for a greater amount of food production comes with an increasing need for adaptation by global agriculture to global climate changes, with the final objective of producing high-quality food while lowering environmental impacts and greenhouse gas emissions. All those challenges are crucial for all stakeholders employed in the agricultural and food production chains [13-15]. Achieving these objectives is furthermore essential for global and local institutions as indicated in various international treaties, such as the 2030 Agenda subscribed by the 193 countries members of the United Nations (UN) [16], and in several documents and reports produced by the Food and Agriculture United Nations Organization (FAO) [17].

To improve the food quality and to reduce the environmental impact of crops cultivation, the producers can consider different ways, such as optimizing the water used during the

irrigation process, optimizing the amount of fertilization used during the cultivation cycle [18] and choosing genotypes resistant to water, salt and thermal stresses [19]. More importantly, the management of food security requires the production of accurate data about crop production in every geographic area and their environmental adaptability in all growth stages [20,21]. The selection of new genotypes capable of withstanding stressful situations due, for example, to unpredictable climatic evolutions is one of the seed industries' main challenges. Nevertheless, genetic selection is unable to predict the interaction through the environment and genotype [22]. The result of the interaction through genotype and environment is called phenotype and considering the phenotyping expressions is basic to obtaining a satisfactory breeding result. Environmental factors can affect the development of the plants, and measuring their effect on genotype represents a primary method to discriminate the better genotypes destined for each cultivation area [21,23]. To solve those issues, applying non-invasive and low-cost technologies to monitor crops' development and health status has become essential in plant breeding techniques [24].

High-throughput plant phenotyping (HTP) can be considered a rapid, efficient and low-cost tool to test the interaction between G and E across a large number of genotypes. The use of High-throughput plant phenotyping platforms (HTPPs) is a powerful method to provide information on the plant growth process [25] through the measurement of biophysical traits, such as biomass, dry and wet weight, Leaf Area Index (LAI) [26,27] and Transpiration (Tr) [28]. Classical biometrical measures can be integrated with Optical indices (OIs) based on colour variation to retrieve information about the plant life cycle. Normally, the acquisition process consists of multiple RGB acquisitions combined with the collection of biometrical parameters over time [22].

Since 2000, Hyperspectral Imaging (HI) has been used in scientific research, e.g. in environmental monitoring, vegetation analysis, atmospheric characterization, and biological and chemical detection. HI is a non-invasive technique based on the properties of light reflectance in the VIS/NIR/SWIR spectral range, and the application of HI techniques is widely used by scientists to retrieve information about the biochemical parameters and the biophysical properties of crops [29,30]. In the past twenty years, Hyperspectral sensors have been successfully applied in several different spatial scales of investigation; e.g. at the satellite scale, to obtain the ecosystem properties over large areas (at 10-30 meters grid spatial resolution), during research activities conducted by the European Space Agency (ESA) and Italian Space Agency (ASI) [31,32]; at the land-scape

scale through aerial surveys, to retrieve field level spectral data at 0,5-5 meters grid spatial resolution), such as in a field drought stress experiment conducted on Zea Mais plants by Damn et al. [33]; to investigate the vineyard health status using an Unmanned Aerial Vehicle (UAV) [30]; and at the proximal scale collecting information from the inner structure in fruits (at sub-centimetric spatial resolution), as in the case of the early detection with a non-invasive method to detect the moldy core infection in apple fruits [34].

New approaches in the HTP field also include the use of HI. Therefore, the capability of HI to classify plants' stress status by using a non-invasive method is attractive for HTP applications [35]. Researchers have used several applications of HI in HTP and HTPP during phenotyping biotic and stress experiments, e.g. to retrieve spectral vegetation indices (VIs), to estimate plant biophysical and biochemical traits [36] through the ratio of VIS/NIR/SWIR spectral bands, or for the early detection of plant diseases; e.g., Thomas et al. have successfully introduced a new HI phenotyping system in a greenhouse experiment which creates a field-like situation to obtain the early detection of powdery mildew. Anyway, the use of HI on a full-scale application in phenotyping remains a distant goal due to the cost of the instruments, the significant time of data processing, the large memory occupied by hyperspectral data and the problematic applicability of rapid and efficient image segmentation processes [29,36-39]. In the last few years, a new generation of portable and low-cost HI cameras and sensors with a VIS/NIR spectral range have been developed. Such devices are relatively straight forward in producing an image composed of multiple spectral bands, increasing the possibility of using new VIs in plant phenotyping applications [29]. Low-cost HI cameras are rarely used in phenotyping. Indeed, their integration into an HTPP was the complicated cause of their need for ample data storage space, difficulties in the image segmentations process and a long time of data processing [38,39]. According to this, studies concerning the application and test of low-cost HI technologies in a HTPP are urgently required to develop new fast and straightforward segmentation methods, new hyperspectral indices to the status of crops, and to test new phenotyping ways alternative to OIs commonly adopted in phenotyping [40,41].

The current work is based on the integration of the Senop HSC-2 low-cost hyperspectral camera (HSC-2) [42] in the HTPP based on Lemna Tec Scanalyzer3D system (LemnaTec GmbH, Germany) during a tomato drought stress experiment. The agronomic and physiologic responses of four untested tomato genotypes (770P, 990P, Red Setter and

Torremaggiore) characterized by a high level of industrial interest, were tested under two cycles of well-watered and deficit irrigation. Several Optical indices (OIs) derived by HTPP imaging analysis, such as Projected Shoot Area (PSA) [43], Hue Index (HUEI) [44], and Colour Senescence Index (SI) [45], obtained during the image acquisition process were analysed and discussed. Subsequently, the OIs obtained were compared with the HI results derived by the hyperspectral acquisition with the HSC-2. Therefore, the objectives of this work were:

- i) To assess the tolerance or sensitivity of four untested tomato genotypes during a greenhouse water stress experiment comparing OIs, e.g. PSA, HUE and SI obtained by HTPP image analysis, to hyperspectral data derived by HI.
- ii) To determine the most important spectral region linked to the tomato water stress in the sampled spectral range.
- iii) To develop an innovative, fast, and simple HI segmentation method suitable in the HTP context.
- iv) To evaluate the potential application and integration of the HSC-2 in a Lemna Tec Scanalzer3D system.

Finally, further applications of low-cost hyperspectral technologies in a phenotyping industrial context are discussed.

2.2 Materials and methods

2.2.1- Experimental design

The experiment was conducted in ALSIA (Agenzia Lucana di Sviluppo ed Innovazione in Agricoltura, S.S. Jonica Km 448,2, 75012 Metaponto MT) from the beginning of May until the end of June 2021. The HTPP in ALSIA is included in the Italian Plant Phenotyping Network Phen-Italy (Phen-Italy). Phen-Italy is the Italian node of EMPHASIS, the European infrastructure (ESFRI) on plant phenotyping (<https://emphasis.plant-phenotyping.eu/>).

Four genotypes of tomatoes, respectively 770P, 990P, Red Setter and Portici (table 1), were tested in a drought stress experiment under two cycles of well-watered and deficit irrigation. For each genotype, one stressed, and one control thesis (six replicates per thesis, for a total amount of 48 tomato plants) were analysed in the HTPP based on a LemnaTec Scanalzer 3D system. The HTPP was integrated with the HSC-2. The experiment timetable is reported in table 2.

Genotype	Origin
770P	Portici (Naples, Italy)
990P	Portici (Naples, Italy)
Red Setter	Portici (Naples, Italy)
Torremaggiore	ISI Sementi (Fidenza, Italy)

Table 1. Genotypes tested during drought stress experiment.

Operation	Day
Transplant in ALSIA	07/05/2021
Start 1st stress	27/05/2021
Hyperspectral acquisition-Image acquisition	27/05/2021
Hyperspectral acquisition- Image acquisition	02/06/2021
Start Recovery	02/06/2021
Hyperspectral acquisition- Image acquisition	08/06/2021
Start 2nd stress	08/06/2021
Hyperspectral acquisition- Image acquisition	15/06/2021
Start Recovery	15/06/2021
Hyperspectral acquisition- Image acquisition	22/06/2021

Table 2. Drought stress experiment timetable.

2.2.2 – Phenotyping Platform and RGB acquisition process

HPP is based on a LemnaTec Scanalyzer 3D system (figure 1) and consists of an automated belt conveyor system with a tracking system based on bar code and RFID for identifying single plants. Four sequential cameras are installed in the HPP to take 3D images of plants in visible (RGB) spectral range. An automated watering system with a

weighting station is installed in the HTPP. The platform allows the quantitative, non-destructive analysis of different crops or model plants under high-throughput conditions. Each plant is imaged sequentially in multiple scanalyzer3D camera units, employing different wavelengths far beyond human vision. A result is a wide number of reproducible and significant data points on any aspect of plant development. Tomato plants were automatically conveyed to the imaging chamber equipped with RGB KAI 2093 image sensor with a 1920×1084-pixel (2 megapixels) resolution. Three images were acquired per plant: one from above the plant in the top view (TV) and two from the side view (SV) at 0° and 90°. The plants were illuminated by standard fluorescence light tubes (35 W/865 cool daylight) and recorded with a Scout camera (*Basler Scout*). Spectral acquisitions were carried out simultaneously with RGB acquisitions.

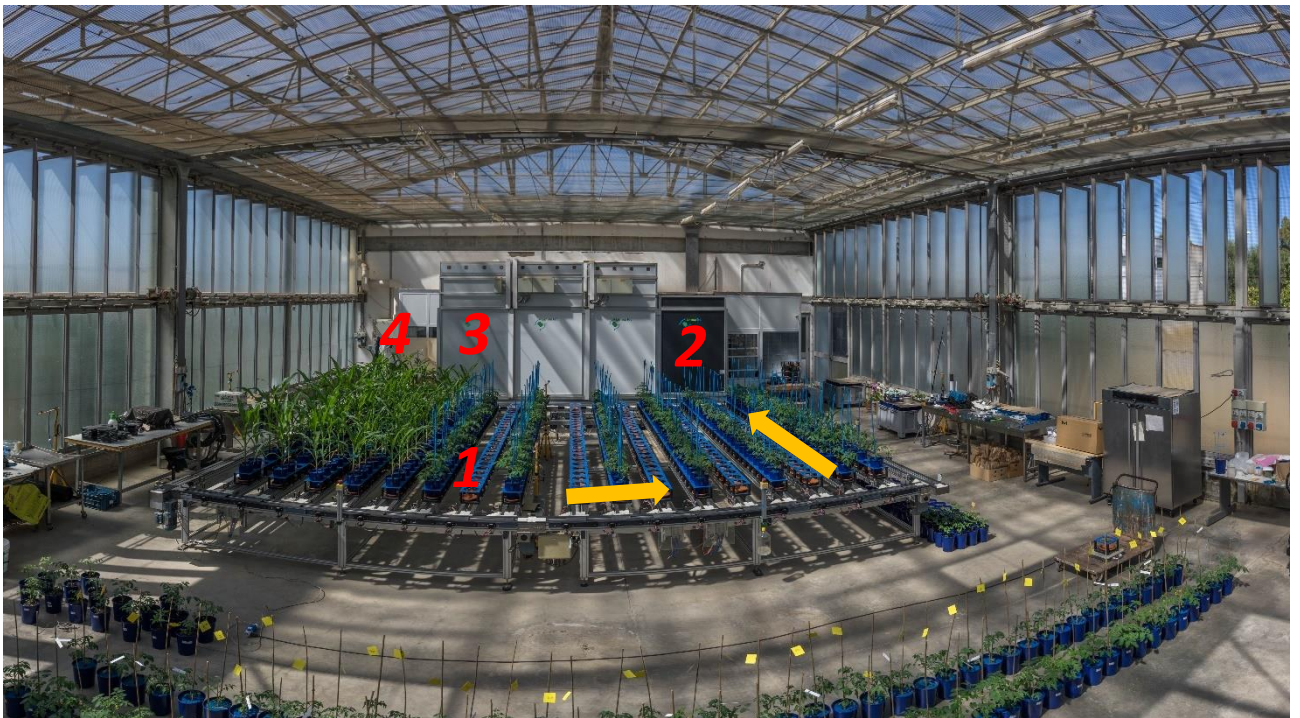


Figure 1. Plants located on the conveyor belt (1) were moved to Visible camera (2) during the acquisition process. Subsequently, plants were moved to hyperspectral camera (3) and automatic irrigation system (4). Plants were left on the conveyor belt during the time between acquisition processes. HTPP is based on a LemnaTec Scanalyzer 3D system.

2.2.3 – Environmental monitoring

Environmental conditions were measured every 15 minutes from the start to the end of the experiment by two relative humidity (HR) and temperature (T) sensors placed on the conveyor belt at the height of 1 meter. Vapour pressure deficit (VPD) is the difference

between the amount of moisture in the air (e_s) and how much water the air can hold when it is saturated (e_a) [46], and it was obtained using RH and T data as follows:

$$VPD = e_s - e_a \quad (1)$$

Where e_s is the saturation vapour pressure or vapour pressure measured in kilopascal (kPa) at air temperature, and e_a is the actual vapour pressure or vapour pressure measured in kPa at dewpoint temperature. e_a and e_s are obtained as follows:

$$e_s = 0.6108 \exp\left(\frac{12.27T}{T + 237.3}\right)$$

and

$$e_a = e_s \frac{RH}{100}$$

When the temperature of the atmosphere increases, the e_s increases, and when the temperature decreases, the e_a decreases. Because it increases or decreases non-linearly, the mean e_a at the mean daily maximum and minimum air temperatures is used for a given period. The actual amount of water vapor held at the current temperature is called the active vapor pressure (e_a). When the temperature of the atmosphere increases, the e_a increases, and when the temperature decreases, the e_a decreases.

2.2.4 – Stress induction and evapotranspiration

Plants were grown in 3.2-litre pots containing 1.8 kg sand-peat mixture from the transplant to the end of the experiment. Water volume in the two theses, well-irrigated and stressed respectively, was maintained at the field capacity (FC) [47] before the first stress induction. Drought stress stages were applied through a 70% reduction of irrigation water in stressed plants (S), maintaining 100% of the irrigation water in the control (C) thesis. The exact water volume provided to the plant was assessed by a balance and irrigation control system (BIS) installed on the conveyor belt. The water weight loss from pots by pot was used to compute ET, that is defined as the water transpired daily by plants summed to water evaporated daily from pots [48], and computed as:

$$ET = TW_{(x)} - TW_{(y)} \quad (2)$$

Where $TW_{(x)}$ is the target weight on a day, and $TW_{(y)}$ is the target weight at the same day. The weight difference, expressed in grams (g), is the water evapotranspired by the plant.

2.2.5- RGB images segmentation and OIs

The segmentation process and OIs retrieving were performed using the Python 3.8 with the PlantCV package v3.9 (<https://plantcv.danforthcenter.org/>). The first step consisted of image resizing and discarding all pixels not corresponding to the plant area. Subsequently, pixel values were computed to obtain a few OIs, respectively:

PSA

PSA is the sum of the number of pixels inside the plant region in each of the three orthogonal views [43], and it was computed in the following way:

$$PSA = TA_{(x)} + TA_{(y)} + TA_{(z)} \quad (3)$$

Where $TA_{(x)}$ is the target top area, $TW_{(y)}$ is the target side area and $TW_{(z)}$ is the target side area rotated 90 degrees, the result is the sum of the three areas expressed in cm^2 .

HUE

HUE is a single number corresponding to an angular position, from 0° to 360° , around a central point or axis on a colour wheel [44], where an angle of 0° corresponds to red, an angle of 90° corresponds to green, and an angle of 180° corresponds to the blue. Usually, leaf colour is included in a HUE range from 120° (dark green) to 60° (yellow). HUE is obtained by the mean of HUE pixel values inside the plant region, and it was computed as follows:

$$HUE = \frac{\sum_1^n PHV}{n} \quad (4)$$

Where PHV is a single HUE pixel value and n is the pixel number inside the plant region.

SI

SI is an optical index used to define a senescence status in plants [45]. SI was computed by the ratio of the HUE values of an image captured in the side view. SI was computed as follows:

$$SI = \frac{(GAS - GerAS)}{GAS} \quad (5)$$

Where GAS is a green area in the side view, and the corresponding value is the sum of pixel values in the HUE angular region from 60° to 180°. GerAS is a greener area in the side view obtained by the sum of pixel values in the HUE angular region from 80° to 180°.

To differentiate control and stressed theses using the PSA, HUE and SI comparisons between theses and genotypes were performed using the analysis of variance (ANOVA) at every experimental phase. The ANOVA was performed using the `anova1` function by MatlabR2021a (MahtWorks,USA).

2.2.6- Hyperspectral data acquisition and processing

Hyperspectral data were collected using the HSC-2. The instrument presents a spectral range available from 650 to 820 nm (see chapter 1) with an image frame size of 1024 x 1024 pixels (1 megapixel). The spectral resolution was settled around 2 nm. A single hyperspectral image was saved as a 3D cube, also called hypercube (HC), formed by 69 spectral bands overlapping on a single object for a virtual memory of 400 megabytes per image. The exposure time was settled at 80 milliseconds per band, and the distance from the hyperspectral camera to the target was established at 1.5 meters (figure 2). A white Lambertian reference target at 75% of reflectance, capable of reflecting light uniformly [49], was placed target area below.



Figure 2. Hyperspectral acquisition process on tomato plant. The white Lambertian surface reference target at 75% of reflectance is the white panel on the plant's left.

The spectral data were acquired in digital number units, and their conversion in radiance ($\text{mW} / \text{nm} \cdot \text{sr} \cdot \text{m}^2$) was obtained through the multiplication of the digital units by a calibration coefficient (see chapter 1). The radiance HC was converted in reflectance as follows:

$$\text{Ref} = \text{Rad} / \text{RT} \quad (6)$$

Where Rad is the radiance obtained by the target and RT is the radiance obtained by the white reference target.

The whole hyperspectral data organization, elaboration and processing described in this work was completed using MatlabR2021a (MahtWorks,USA).

2.2.7- Automatic segmentation of HIS

The application of an automatic segmentation method is needed to obtain a rapid plant pixels separation from the background. To facilitate this, the background was covered

with a matt black cover to delete reflection effects due to photons scattering (figure 2). Segmentation's first step was excluding the white target reference from the image. This operation was automated by maintaining the reference position and target distance from the hyperspectral device during acquisition. According to this, the HIS dimension was reduced to exclude the reference panel. Segmentation's second step was the application of a binary mask. The HC was composed of 69 images (one image per spectral band), and the segmentation process was based on segmentation in an image at one single spectral band; through visive and manual selection of the band capable of separating the target from the background. The reflectance value capable of separating the target from the background was chosen through a selection method based on defined reflectance values, selected through a percentile value selection. The segmentation percentile value was determined based on the complete image background elimination and the removal of geometric light reflection effects. Indeed, only plant regions in a perpendicular position to the hyperspectral camera optics should be selected. Subsequently, were applied a segmentation mask on images composed of 0 and 1 values, where 0 corresponded to the values less than the chosen percentile and 1 corresponded to the values greater or equal. The segmentation mask derived by one-band percentile segmentation was applied in all bands.

2.2.8 – *Hyperspectral data analysis*

After calibration and segmentation of the HI, the HC was processed to extract the average signature by each pixel from each genotype at all acquisition times. The spectral signatures were processed to obtain the hyperspectral index (H-index) capable of discriminating the stress status in genotypes during the experimental phases. The H-index was obtained computing the maximum value of the approximate derivative point by point for of each spectral signature. The result represents the maximum slope point in the full acquired spectral range. The approximate derivative was performed using the diff function by MatlabR2021 (MahtWorks,USA). To differentiate control and stressed theses using the novel H-index, a few comparisons between theses and genotypes for a total of twenty comparisons (one per genotype per five acquisition times) were performed using the analysis of variance (ANOVA) at every stress and recovery phase. The ANOVA was performed using the anova1 function by MatlabR2021a (MahtWorks,USA).

Finally, the performance of the H-index and the OIs to the water stress detection on 770P, 990P, Red Setter and Torremaggiore tomato genotypes were compared and discussed.

2.3- Results

2.3.1- Environmental variations and ET

RH, T and VPD were computed by processing the humidity and temperature data collected from the beginning to the end of the experiment (figure 3).

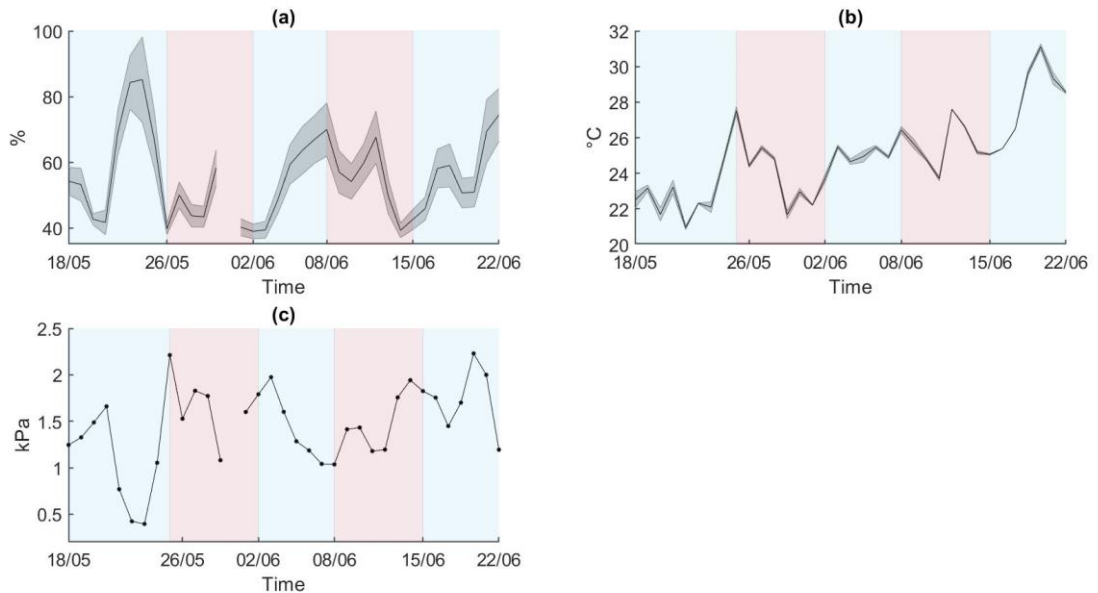


Figure 3. RH (a) expressed as percentage, T (b) reported in °C and VPD (c) reported as Kilopascal (kPa) trends from the beginning to the end of the experiment, where the red and blue areas represent the stress and full-irrigation experimental phases. The standard deviation was reported in RH and T plots. T data were not recorded on day 31/05/2021.

Air temperature showed a general increase over time. The daily maximum temperature (TMax) was collected on day 20/06/2021, and the daily minimum temperature (TMin) was collected on day 22/05/2021. The daily maximum RH (RH max) was registered on 25/05, and the daily minimum RH (RHmin) was registered on 14/05/2021. RH and T show opposite trends during the initial stages of the experiment (until 04/06/2021). Subsequently, T and RH trends appear similar from 05/06/2021 to 11/06/2021. Trends returned opposite from 12/06/2021 to the end of the experiment. VPD values spanned from 1 kPa to 2.3 kPa and follow a general increment reflecting the temperature rise during the experiment.

The evapotranspiration (ET) was computed for all four genotypes and for all water treatments by daily weight differences of pots (figure 4).

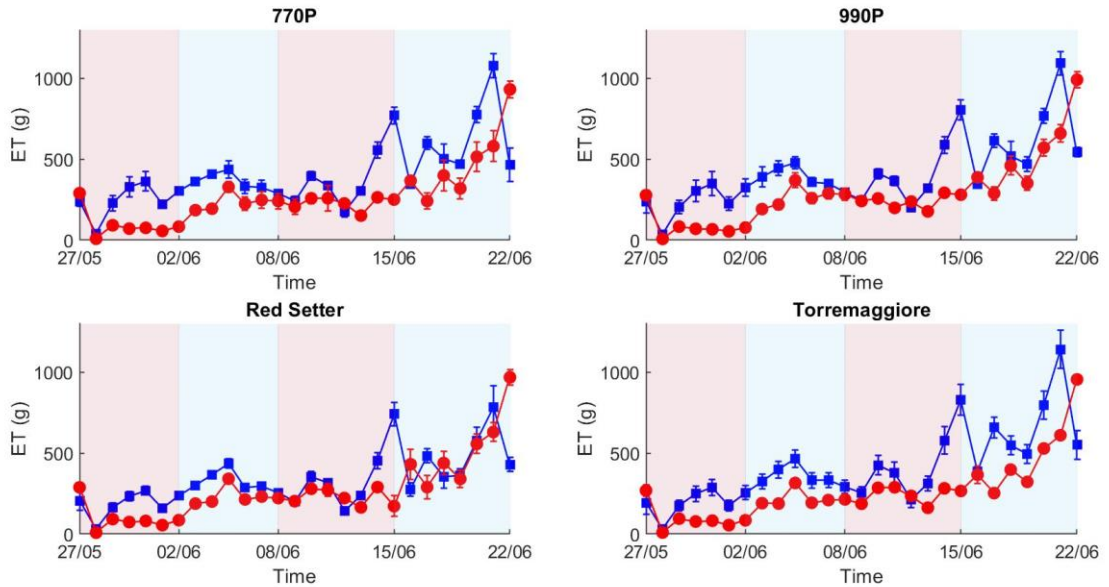


Figure 4. ET trend by 770P, 990P, Red Setter and Torremaggiore genotypes from the beginning to the end of the experiment. The red line represents the stress thesis, and the blue line represents the control thesis. The red and blue areas in the plots represent the stress and full-irrigation experimental phases. The standard deviation was reported. The choice of colours in plots (lines and experimental phases, respectively) was applied in subsequent graphs in the same way as the figure just described, and the description of the plot colour style will not be repeated in similar graphs.

The first stress phase exhibits differences in ET between genotypes in stressed and control theses, where 770P and 990P show higher differences in ET than Torremaggiore and Red Setter between control and stressed theses. ET is growing during the 1st stress phase in the watered thesis, likely reflecting the plant growth process. ET values are higher for the well-watered theses due to water availability in the soil. ET values tend to converge for all theses on 08/06/2021, concomitantly to the end of the first recovery period, and this result shows an efficient recovery by stressed theses in all genotypes. The second stress phase shows the maximum levels of ET, where the total amount of water lost reached peaks of 900 grams per days in 770P and 990P genotypes, showing a higher ET level than Torremaggiore and Red Setter. Generally, the thesis that received full irrigation during all experimental phases shows a greater value of ET than the stressed over time. Indeed, the experimental phases with differential irrigation show a clear separation in terms of ET between theses showing remarkable differences, especially in 770P and 990P genotypes, which appear more susceptible to water stress than Red Setter and Torremaggiore.

2.3.2- HTPP results

Optical and biometrical data obtained by the HTPP were successfully computed and processed. Results have permitted to obtain the assessment of three different phenotyping parameters.

PSA

PSA was computed over the experimental phases; the results are shown in figure 5.

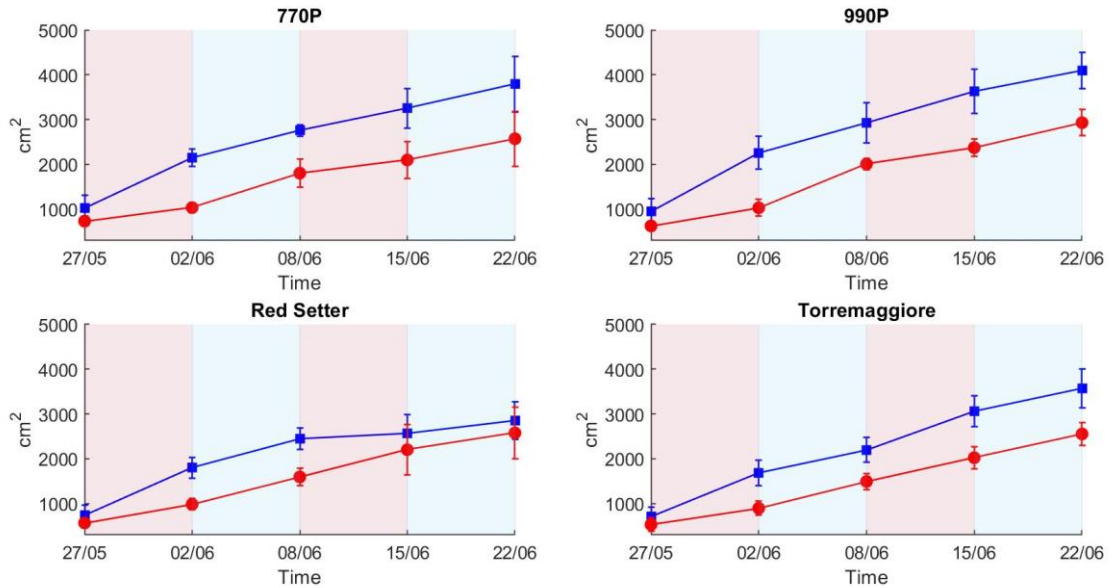


Figure 5. PSA trend for all four genotypes from the beginning to the end of the experiment. The standard deviation was reported.

The analysis of variance (ANOVA) was performed on PSA results to assess significant differences between theses. The results are shown in Table 3.

Genotypes	Start	1 st Stress	1 st Recovery	2 nd Stress	2 nd Recovery
770P	NS	S	S	S	S
990P	NS	S	S	S	S
Red Setter	NS	S	S	NS	NS
Torremaggiore	NS	S	S	S	S

Table 3. ANOVA results. The ANOVA was performed between theses on PSA results for all genotypes. For P-value ≤ 0.01 , the result was considered as significant (S), while for P-value > 0.01 , the result was considered as non-significant (NS). The subsequent

ANOVA results were reported using the same parameters (abbreviations and P-value) adopted here.

At the start of the experiment plants show similar PSA values, about 800-900 cm², and significant differences between these were not reported. Generally, PSA appeared well differentiated during the first stress phase due to the application of the two irrigation levels, as confirmed by ANOVA results. The most significant gap in terms of PSA between well-irrigated and stressed these was measured in 770P and P970 genotypes at the end of the first stress, due to lower biomass production in stressed plants, concomitantly with a higher ET difference between control and stressed these compared to Red Setter and Torremaggiore genotypes. Indeed, Red Setter and Torremaggiore show a minor gap between these compared to the other two genotypes in terms of water evapotranspired during the first stress phase. The significance of the PSA differences were confirmed by ANOVA results. During the first recovery, an increasing of growth rate in all stressed these was reported, where 770P and 990P have shown a marked increment in biomass production compared to Red Setter and Torremaggiore genotypes. The second stress phase, from 08/06 to 15/06, shows a growth rate decrement in 770P and 990P stressed these, while the growth rate in Red Setter and Torremaggiore remains constant compared to the precedent recovery phase. Red Setter control thesis show a growth rate decrement strongly reducing PSA differences compared to the stressed. The second recovery phase show a similar trend compared to the first recovery phase, showing a growth rate increment in 770P and 990P genotypes reducing differences between these. Significant differences between these are shown in 770P, 990P and Torremaggiore genotypes at the end of the second recovery phase.

HUE

HUE were computed during the experimental phases and results are shown in figure 6.

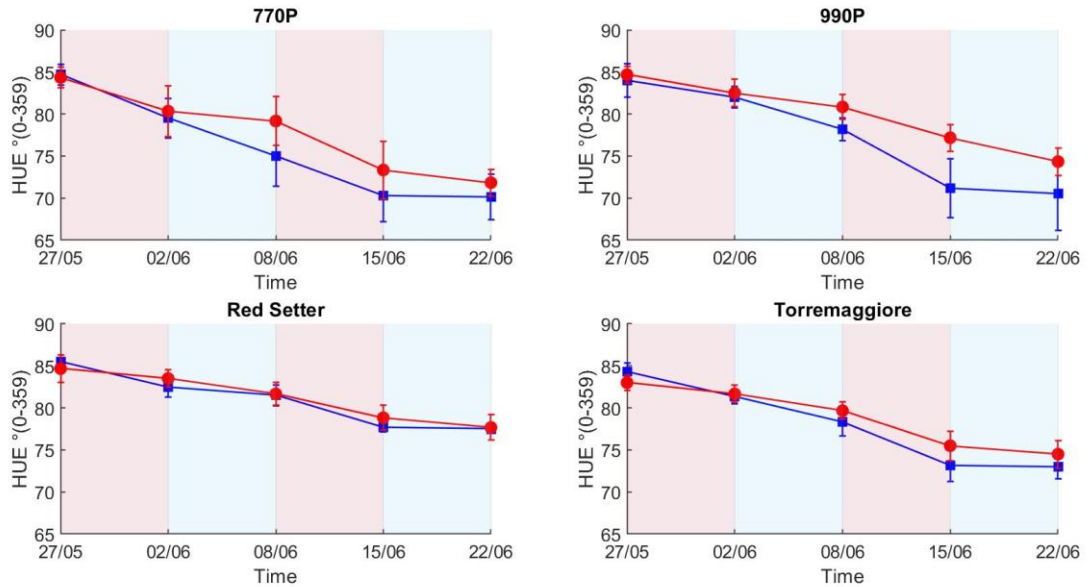


Figure 5. HUE results. HUE is expressed in degrees. The standard deviation was reported.

The ANOVA was performed on HUE, and results are shown in Table 4.

Genotypes	Start	1 st Stress	1 st Recovery	2 nd Stress	2 nd Recovery
770P	NS	NS	NS	NS	NS
990P	NS	NS	S	S	NS
Red Setter	NS	NS	NS	NS	NS
Torremaggiore	NS	NS	NS	NS	NS

Table 4. ANOVA results. The ANOVA was performed between theses on HUE results for all genotypes.

Results show a similar start regarding the HUE range for all genotypes and theses to a HUE average of 84° corresponding to light green. Significant differences between genotypes were not reported as showed by ANOVA results. At the end of the first stress phase, HUE does not show significant differences between genotypes and theses. After the subsequent recovery phase, HUE shows significant differences in Genotype 990P and a mild separation between stressed and control theses in the 770P genotype, where the control theses have started to show a colour change from green to yellow. Differences in HUE level on 990P theses appears substantial, where the control thesis shows a level of

75-77 degrees, and stressed thesis reported an HUE around 80 degrees. During the 2nd stress, results confirmed differences in HUE trends in control and stress theses for 990P genotype, showing an increase of HUE differences between theses. A mild separation without significant differences in terms of HUE was reported in Red Setter, Torremaggiore and 770P genotypes as highlighted by ANOVA results and HUE trends. At the end of the last recovery phase, the HUE results aren't show significant differences between theses in all genotypes, and the mild HUE gaps showed during the second stress were reduced.

Senescence Index (SI)

SI is an optical index used to define a senescence status in plants. SI was computed during the experimental phases and results are shown in figure 6.

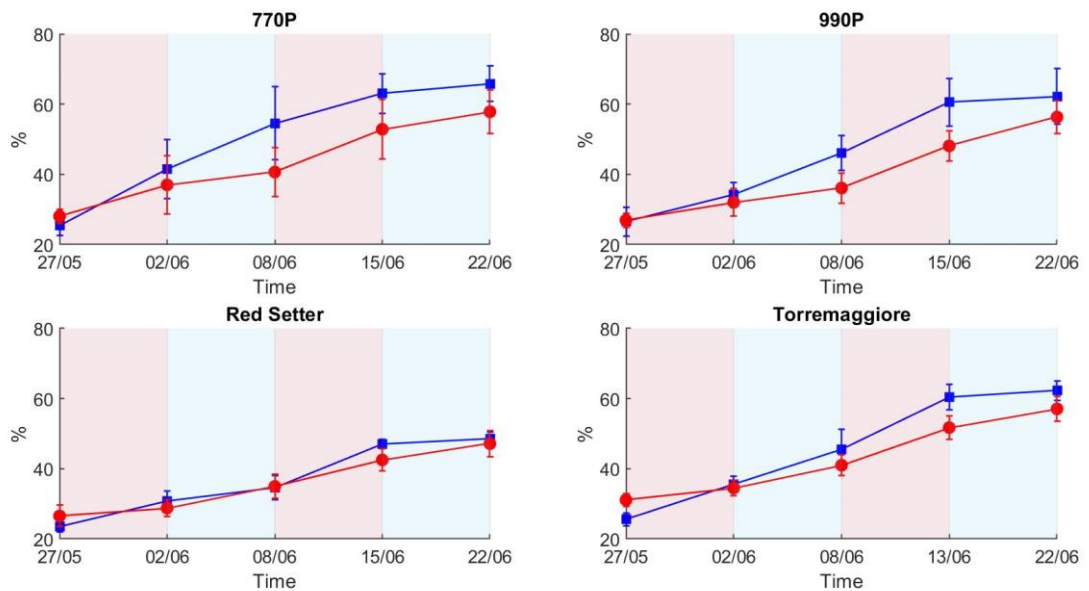


Figure 6. SI results. SI is expressed as percentage. The standard deviation was reported.

The ANOVA was performed on SI, and results are shown in Table 5.

Genotypes	Start	1 st Stress	1 st Recovery	2 nd Stress	2 nd Recovery
770P	NS	NS	NS	NS	NS
990P	NS	NS	S	S	NS
Red Setter	NS	NS	NS	S	NS
Torremaggiore	S	NS	NS	S	S

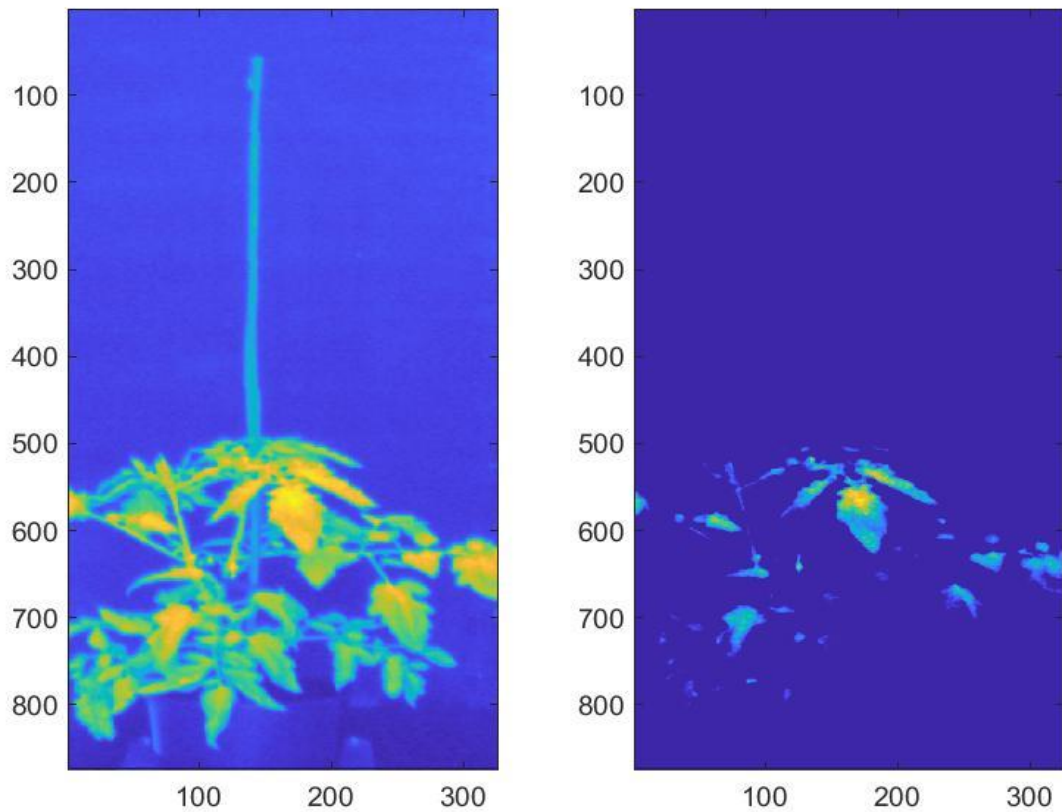
Table 5. SI ANOVA P-value results for all genotypes and theses.

At the start of the experiment, all genotypes and theses start with a SI range from 20 to 30%. 770P, 990P, and Red Setter don't evidence substantial differences between theses, whereas Torremaggiore genotype shows significant differences between theses at 27/05, disagreeing with PSA, HUE and ET results. ANOVA results don't show significant differences between genotypes at the end of the first stress. The first recovery underlines significant differences only for 990P genotype, which has confirmed this result even in subsequent stress phases. At the end of the second stress, significant differences between theses highlighted by ANOVA results were also reported in Torremaggiore and Red Setter. After the last recovery phase, results have shown a decrement of SI in 990P and Red Setter genotypes which don't evidence significant differences between theses. In contrast, Torremaggiore has maintained significant differences between the two differential irrigation regimes. Overall, the SI trend in control theses show a major shape than stressed during the experimental phases.

2.3.3- Hyperspectral analysis

Segmentation process

A segmentation process based on the 96^o percentile was adopted to obtain a clear separation between plants and background (figure 7) for all hyperspectral images.



(a)

(b)

Figure 7. Example of segmentation results. In this example, the segmentation process based on the 96^o percentile was applied on a Red Setter genotype control thesis acquired on 08/06/2021.

Before the segmentation process (a), the image was composed of background and plant; after the segmentation process (b), the image was composed of only plant re-gions with a reflectance value larger than 96^o percentile, for a total amount of 11408 pixels belonging to the plant region. Results show a clear separation between plants and background combined with eliminating the canopy reflection effects. The spectral band selected to extrapolate the plant region from the background was identified at 750 nm, in the spectral region corresponding to the end of the red edge curve (figure 8). The magnitude of the reflectance values resulted higher in comparison to the previous spectral bands.

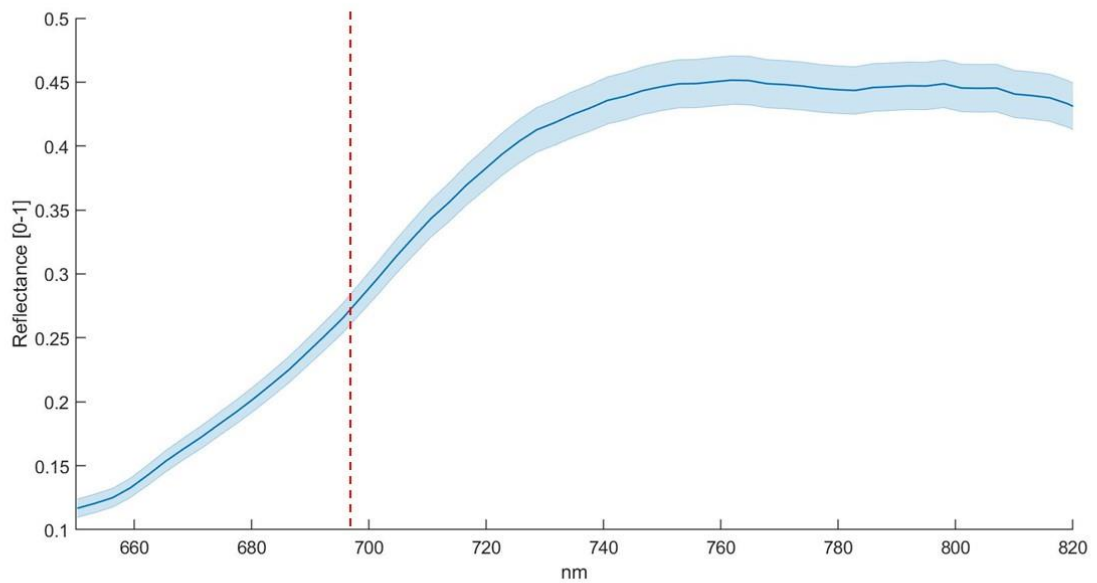


Figure 8. The spectral signature derived by the segmented plant (figure 7). The red dashed line shows the spectral band (691 nm) with the maximum value of the approximate derivative used to obtain the H-index. The standard deviation was reported.

The spectral signature comprised 11408 signatures derived from the same number of pixels. The figure clearly shows differences in reflectance magnitude from the red edge curve spectral region (from 650 to 720 nm) on the left and the rest of the curve on the right. During the experiment, over 250 HI images were collected for a total amount of 120.6 Gigabytes occupied; the storage of the HI is an expensive process in terms of memory and using an efficient segmentation method can reduce the memory occupied. After the segmentation, the hyperspectral data were reduced to a total storage space of 18.7 Gigabytes, reporting a complex data reduction of 85.5%.

Hyperspectral index

The hyperspectral data obtained by the segmentation process were processed to obtain the H-index capable to differentiate stress and control these over stress and recovery phases. The H-index is based on the maximum value of the approximate derivative and it is linked to the red-edge spectral region slope. The H-Index was tested on all experimental phases and results were reported in figure 9.

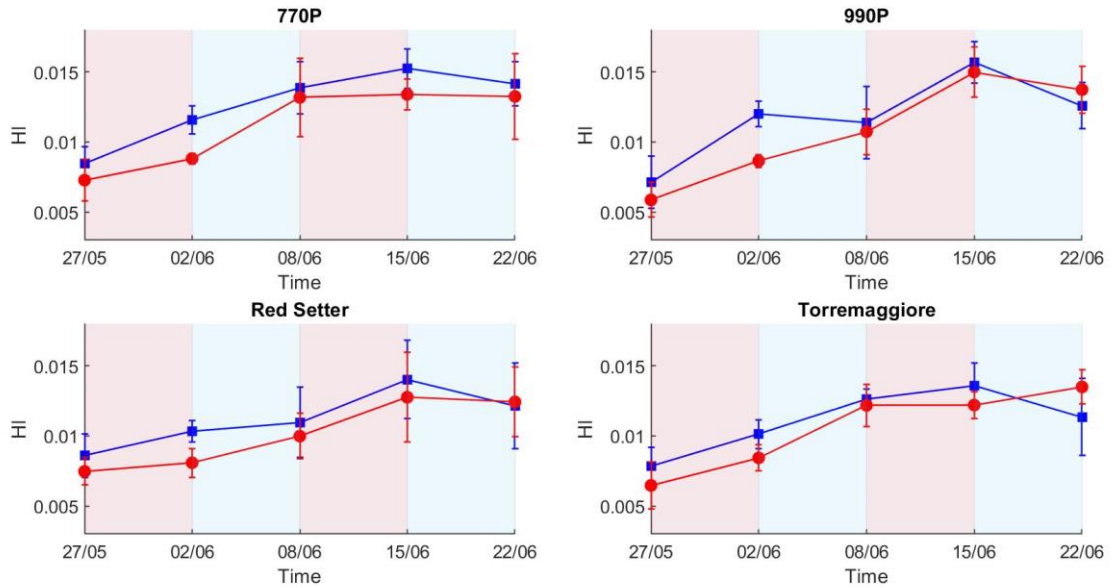


Figure 9. H-index (HI) trends for all four genotypes from the beginning to the end of the experiment. The standard deviation was reported.

The ANOVA was computed for all genotypes to evidence the H-index differences between the two theses over the experiment. Results are shown in table 6.

Genotypes	Start	1 st Stress	1 st Recovery	2 nd Stress	2 nd Recovery
770P	NS	S	NS	NS	NS
990P	NS	S	NS	NS	NS
Red Setter	NS	S	NS	NS	NS
Torremaggiore	NS	S	NS	NS	NS

Table 6. H-index ANOVA results for all genotypes and theses.

All genotypes and theses started the first stress phase without significant differences. At the end of the first stress, there are substantial variations in all theses, as shown by ANOVA results. All theses show a net separation between control and stressed theses. 770P and 990P well-irrigated theses show a significant separation in the H-index compared to the stressed. Red Setter and Torremaggiore offer a lower break between theses than 990P and 770P, demonstrating a higher level of stress resistance. At the end of the first recovery, the H-index show similar results in all theses and genotypes. Stressed theses show a net recovery reporting a major increment in terms of H-index compared to

the well-irrigated theses confirming the irrigation regime trend and the ET results. Significant differences in H-index are not reported, as demonstrated by ANOVA results. The slope of the control theses in the 990P and Setter genotypes de-creases between the end of the first stress and recovery, reporting an increment of the standard deviation at the end of the first recovery phase. Overall, the first recovery phase shows a substantial recovery in stressed theses which show a similar spectral response than the well-irrigated theses in accordance with the full irrigation regime and ET results reported at the first recovery. After the second stress, the ANOVA results don't show significant differences in H-index between theses. However, 770P and Tor-re Maggiore genotypes have reported differences in the slope of the two theses, high-lighting a lower slope in the stressed than the control. At the end of the second recovery, there are no differences in H-index between theses, as shown by ANOVA results.

2.4- Discussions

RH and T results reflect the seasonal course registered in the geographic area where the experiment was conducted [50]. RH and T changes are related to VPD trend and ET demand. Indeed, when the water availability is reduced and VPD increases as in water stress conditions, the plant responds by closing her stomata with a consequent reduction of the ET, as described by Sadok et al. [52]. The closure of the stomata and the consequent reduction in transpiration is the first response to the water stress condition. The second stress phase was significantly more intense than the first phase, showing a maximum level of ET, and this result is due to the high-temperature values registered during the second stress. The consequent of the temperature rise was an increment of VPD during the second stress phase causing a greater ET demand compared to the first stress phase, in agreement with the results obtained by Noh et al. and Sadok et al. [46,52] which have demonstrated the link between VPD and ET. ET differences between stressed and control theses appear more contained compared to trends reported during the first stress. There are not several studies in the literature about the drought adaptability of genotypes used in this experiment; deposite this, results obtained can be explained by a physiological adaptation to the water stress condition in partially irrigated plants, in accordance with Jureková et al. [53] and Rhodes et al. [54] which have measured metabolic and physiological changes associated with adaptation of plant cells to water stress. Overall, the four genotypes show different responses in terms of ET between the two theses due to the stress phases. Genotypes 770P and 990P show greater values of ET in control theses showing a lower

water stress resistance than Red Setter and Torremaggiore genotypes. Generally, ET differences between tomato genotypes can be due to their water stress resistance, explicable in different morphological traits, such as leaf rolling, leaf orientation, leaf size and plant habit [55]. The biomass production and growth rate in tomato plants were influenced by the water availability, and differences in PSA between control and stressed theses can be due to the different irrigation levels, in accordance with results obtained by Rhodes et al. and Patanè et al. [55,56], which have demonstrated the direct proportionality between available water and biomass production. Red Setter and Torremaggiore show minor differences between stressed and well-irrigated theses in terms of PSA compared to 770P and 990P genotypes. In addition, Red Setter has registered lower PSA differences between thesis over stress and recovery phases showing greater tolerance to the water stress condition. HUE results show a physiological colour change from green to light yellow in all genotypes and theses over the experimental phases. The colour change in leaves is a natural physiological effect due to the tomato plant's senescence and consists of a chlorophyll breakdown from the leaf margin to the interior of the leaf blade as reported by Quirino et al. [57]. The stress condition causes a decrease in the water content in stressed plant leaves, as measured by Khan et al. [58], and the result of this process is a slowdown in the chlorophyll breakdown. Therefore, a slowdown in a colour change can be attributed to the stress status, in accordance with results obtained by Janni et al. [59] which has conducted a tomato drought stress experiment using the LemnaTec Scanalyzer 3D system. The HUE results do not efficiently describe the ET trend excepted for the 990P genotype, which have reported significant differences between theses at the second stress and second recovery phases.

The most significant variations in SI between control and stressed theses were reported in the 990P genotype as confirmed by ANOVA results at the end of the first stress and second recovery; at the same time, Torremaggiore showed limited variations of SI in all experimental phases excepted at the second stress where the theses are statistically diffracted. SI, as HUE, are colorimetric index based on the analysis of RGB images. Therefore, SI better describes than HUE the ET trend, highlighting more differences between theses during the experimental phases. Higher SI values correspond to a light green /yellow plant colour and high SI values in controls are due to their minor ratio between chlorophyll and water compared to stressed theses, where the minor water content increases the chlorophyll and water ratio showing a green colour more intense than control theses [60]. The inconsistencies between HUE, SI and PSA results can be

attributed to a differential response over time to the water stress condition between biometric and RGB parameters. Indeed, the growth rate slowing is immediately registered in the presence of limited water availability, while colour variation appears with a delay and a less homogeneous distribution between plants.

The segmentation technique developed has permitted the minimization of the geometric light scattering effects in combination with removing of the background pixels and shadow effects caused by the complex and unpredictable canopy structure. The light reflection effects due to the overlapped leaves represent a critical issue in obtaining a clean spectral signal. Therefore, an approach based on the automatic selection of the leaves in a nadiral position compared to the camera's optics simplifies the use of 3D radiative transfer models by focusing only on leaf sub regions [29,35]. Using a homogeneous background in the acquisition process characterised by low reflectance values compared to the target represents a fundamental element to obtain a rapid and efficient segmentation, solving the needs of storage space and speed in the hyperspectral data processing [38,39]. Indeed, the application of HI for plant phenotyping in an industrial context needs to be economical in terms of memory occupied and image segmentation efficiency because the application of complex and expensive processes represents a cost for the industries.

The trend of the spectral signatures collected during the experiment respects the spectral signatures derived by a vegetation target with an increase in slope from 650 to 720 nm, as reported in the literature [29,32]. The H-index is based on the maximum value of the approximate derivative point by point for each spectral signature. The result represents the maximum slope point in the full acquired spectral range. Therefore, higher H-index values correspond to a greater slope in the red-edge position, from 650 to 730 nm. The link between the slope of the red edge spectral region and water stress condition was already investigated by Schlemmer et al. and Boochs et al. [60,61], which have demonstrated the link between a lower slope in the red edge spectral region and the water stress presence. Differences between these are linked to the different plant's spectral responses in full and partial irrigation regimes. Indeed, the higher H-index value indicates a significant difference in the reflectance slope of the red-edge spectral region. Compared to the HUE and SI results, H-index better describe the differential irrigation regimes conducted during the first stress phase. HUE and SI don't show clearly differences between these compared to the ET results, while H-index clearly describes differences between the two theses in all genotypes. This result highlights HI's potential for the early

detection of water stress than the RGB methods. The optical response in the visible spectral region turns out to be less rapid than the NIR response for the leaf water content, as already demonstrated by Steidleer et al. [61]. There are no studies on the red edge spectral response and susceptibility or tolerance to the water stress condition for the tomato genotypes tested in this study. Still, the behaviors of the stressed theses obtained in the second stress, where ANOVA results highlighted no differences between theses, can be due to the water stress adaptability of stressed plants [53,54]. Major values of standard deviation in 990P and Red Setter genotypes at the end of the first recovery than the first stress can be attributed to the different growth rate between samples. Nevertheless, the global trend of the H-index was not significantly influenced providing clear results in terms of trend.

Overall, 770P and 990P theses show the most remarkable statistical differences over the experimental phases, also considering the ET results compared to Red Setter and Torremaggiore, as highlighted by PSA, H-index and less clearly by HUE, SI and effects. Therefore, this result indicates a minor capacity by 770P and 990P stressed theses to maintain a similar behavior to the controls. Consequently, 770P and 990P show a higher susceptibility to water stress than the Red Setter and Torremaggiore genotypes.

2.5- Conclusions

In this study, four untested tomato genotypes were successfully tested in an HTPP LemnaTec Scanalyzer 3D system during a tomato drought stress experiment. The HTPP was integrated for the first time with the HSC-2, and over 120 Gigabytes of HIS were acquired and processed. The Genotypes were tested during two cycles of full and partial irrigation, and the principal phenotyping traits, such as PSA, HUE and SI were assessed. The RH and T parameters were collected, and VPD was obtained over the experiment. Therefore, the conclusions of this study are:

i) The integration of the HSC-2 in the HTPP based on the LemnaTec Scanalyzer 3D system has permitted to increase in the water stress detection capability by the HTPP; indeed, a hyperspectral camera with a NIR spectral range appears more efficient to detect the stress status during the first stress and recovery phases than the RGB technologies. In addition, a novel H-index based on the red-edge slope capable of detecting the water stress status in P970, 990P, Red Setter and Torremaggiore tomato genotypes was developed and tested.

ii) The PSA describe more efficiently than HUE and SI the differential irrigation regimes especially in the first stress phase, whereas SI and HUE don't show a clear picture of the irrigation trend compared to the ET results. The H-index clearly describe the first stress and recovery phases compared to PSA, HUE and SI, showing a higher sensitivity and better describing the ET trend. In addition, the H-index more clearly represents the second stress phase than PSA, HUE and SI, which globally appears less visible, probably due to an adaptation to the stress condition by stressed theses. Based on the results, a low-cost hyperspectral camera with a spectral range similar to the Senop HSC-2 can be integrated with the RGB technologies commonly used in phenotyping activities, increasing the performance of the phenotyping process. In addition, integrating low-cost hyperspectral technology in an HTPP could open new ways to develop innovative phenotyping techniques.

iii) The segmentation method based on the percentile technique in a standardised acquisition set has efficiently reduced the hyperspectral dataset dimension, reporting a data reduction of the 85.5%; simultaneously, the time processing of the HIS has been reduced. These results are gaining in an industrial context, where storage space and time processing are primary issues.

iv) The tolerance and susceptibility to the water stress of the four untested genotypes were successfully assessed. Overall, the OIs and H-index results show that genotypes 770P and 990P were more susceptible to water stress than Red Setter and Torremaggiore genotypes. Finally, results obtained in this study open new ways for applying a low-cost hyperspectral camera in a phenotyping contest to detect other abiotic stress statuses, such as the nutrient deficit and metabolic alteration, and pathology caused by biotic stresses; therefore, further studies were recommended.

References

- 1- Lutz, Wolfgang, Warren Sanderson, and Sergei Scherbov. 'The End of World Population Growth'. *Nature* 412, no. 6846 (August 2001): 543–45. <https://doi.org/10.1038/35087589>
- 2- McKenzie, Fiona C., and John Williams. 'Sustainable Food Production: Constraints, Challenges and Choices by 2050'. *Food Security* 7, no. 2 (1 April 2015): 221–33. <https://doi.org/10.1007/s12571-015-0441-1>
- 3- Cogato, Alessia, Franco Meggio, Massimiliano De Antoni Migliorati, and Francesco Marinello. 'Extreme Weather Events in Agriculture: A Systematic Review'. *Sustainability* 11, no. 9 (January 2019): 2547. <https://doi.org/10.3390/su11092547>
- 4- Frame, David J., Suzanne M. Rosier, Ilan Noy, Luke J. Harrington, Trevor Carey-Smith, Sarah N. Sparrow, Dáithí A. Stone, and Samuel M. Dean. 'Climate Change Attribution and the Economic Costs of Extreme Weather Events: A Study on Damages from Extreme Rainfall and Drought'. *Climatic Change* 162, no. 2 (1 September 2020): 781–97. <https://doi.org/10.1007/s10584-020-02729-y>
- 5- Beillouin, Damien, Bernhard Schauburger, Ana Bastos, Phillipe Ciais, and David Makowski. 'Impact of Extreme Weather Conditions on European Crop Production in 2018'. *Philosophical Transactions of the Royal Society B: Biological Sciences* 375, no. 1810 (26 October 2020): 20190510. <https://doi.org/10.1098/rstb.2019.0510>
- 6- Dalhaus, Tobias, Wolfram Schlenker, Michael M. Blanke, Esther Bravin, and Robert Finger. 'The Effects of Extreme Weather on Apple Quality'. *Scientific Reports* 10, no. 1 (13 May 2020): 7919. <https://doi.org/10.1038/s41598-020-64806-7>
- 7- Elahi, Ehsan, Zainab Khalid, Muhammad Zubair Tauni, Hongxia Zhang, and Xing Lirong. 'Extreme Weather Events Risk to Crop-Production and the Adaptation of Innovative Management Strategies to Mitigate the Risk: A Retrospective Survey of Rural Punjab, Pakistan'. *Technovation* 117 (1 September 2022): 102255. <https://doi.org/10.1016/j.technovation.2021.102255>
- 8- Lehmann, Jascha, Dim Coumou, and Katja Frieler. 'Increased Record-Breaking Precipitation Events under Global Warming'. *Climatic Change* 132, no. 4 (1 October 2015): 501–15. <https://doi.org/10.1007/s10584-015-1434-y>
- 9- Spinoni, Jonathan, Paulo Barbosa, Alfred De Jager, Niall McCormick, Gustavo Naumann, Jürgen V. Vogt, Diego Magni, Dario Masante, and Marco Mazzeschi. 'A New Global Database of Meteorological Drought Events from 1951 to 2016'. *Journal*

- of Hydrology: Regional Studies 22 (1 April 2019): 100593. <https://doi.org/10.1016/j.ejrh.2019.100593>
- 10- Niu, Shuli, Yiqi Luo, Dejun Li, Shuanghe Cao, Jianyang Xia, Jianwei Li, and Melinda D. Smith. 'Plant Growth and Mortality under Climatic Extremes: An Overview'. Environmental and Experimental Botany 98 (1 February 2014): 13–19. <https://doi.org/10.1016/j.envexpbot.2013.10.004>
- 11- Asseng, S., F. Ewert, P. Martre, R. P. Rötter, D. B. Lobell, D. Cammarano, B. A. Kimball, et al. 'Rising Temperatures Reduce Global Wheat Production'. Nature Climate Change 5, no. 2 (February 2015): 143–47. <https://doi.org/10.1038/nclimate2470>
- 12- www.fao.org. 'Damages and Losses'. <https://doi.org/10.4060/cb3673en>
- 13- Costa, Ciniro, Eva Wollenberg, Mauricio Benitez, Richard Newman, Nick Gardner, and Federico Bellone. 'Roadmap for Achieving Net-Zero Emissions in Global Food Systems by 2050'. Scientific Reports 12, no. 1 (5 September 2022): 15064. <https://doi.org/10.1038/s41598-022-18601-1>
- 14- Godde, C. M., D. Mason-D'Croz, D. E. Mayberry, P. K. Thornton, and M. Herrero. 'Impacts of Climate Change on the Livestock Food Supply Chain; a Review of the Evidence'. Global Food Security 28 (1 March 2021): 100488. <https://doi.org/10.1016/j.gfs.2020.100488>
- 15- Molotoks, Amy, Pete Smith, and Terence P. Dawson. 'Impacts of Land Use, Population, and Climate Change on Global Food Security'. Food and Energy Security 10, no. 1 (2021): e261. <https://doi.org/10.1002/fes3.261>
- 16- 'THE 17 GOALS | Sustainable Development'. <https://sdgs.un.org/goals>
- 17- 2021 (Interim) Global Update Report: Agriculture, Forestry and Fisheries in the Nationally Determined Contributions. FAO, 2021. <https://doi.org/10.4060/cb7442en>
- 18- Garibaldi, Lucas A., Néstor Pérez-Méndez, Michael P. D. Garratt, Barbara Gemmill-Herren, Fernando E. Miguez, and Lynn V. Dicks. 'Policies for Ecological Intensification of Crop Production. Trends in Ecology & Evolution 34, no. 4 (1 April 2019): 282–86. <https://doi.org/10.1016/j.tree.2019.01.003>
- 19- Khan, Athar, M. Shirazi, Aisha Shereen, M. Ali, Ben Hadjimbark Asma, Nabila Jilani, and Wajid Mahboob. 'Agronomical and Physiological Perspectives for Identification of Wheat Genotypes for High-Temperature Tolerance'. Pakistan Journal of Botany 52 (15 December 2020). [https://doi.org/10.30848/PJB2020-6\(13\)](https://doi.org/10.30848/PJB2020-6(13))

- 20- Vogel, Elisabeth, Markus G. Donat, Lisa V. Alexander, Malte Meinshausen, Deepak K. Ray, David Karoly, Nicolai Meinshausen, and Katja Frieler. 'The Effects of Climate Extremes on Global Agricultural Yields'. *Environmental Research Letters* 14, no. 5 (May 2019): 054010. <https://doi.org/10.1088/1748-9326/ab154b>
- 21- Challinor, A. J., T. R. Wheeler, P. Q. Craufurd, C. A. T. Ferro, and D. B. Stephenson. 'Adaptation of Crops to Climate Change through Genotypic Responses to Mean and Extreme Temperatures'. *Agriculture, Ecosystems & Environment* 119, no. 1 (1 February 2007): 190–204. <https://doi.org/10.1016/j.agee.2006.07.009>
- 22- Tariq, Muhammad, Mukhtar Ahmed, Pakeeza Iqbal, Zartash Fatima, and Shakeel Ahmad. 'Crop Phenotyping'. In *Systems Modeling*, edited by Mukhtar Ahmed, 45–60. Singapore: Springer, 2020. https://doi.org/10.1007/978-981-15-4728-7_2
- 23- Xu, Yunbi. 'Envirotyping for Deciphering Environmental Impacts on Crop Plants'. *Theoretical and Applied Genetics* 129, no. 4 (1 April 2016): 653–73. <https://doi.org/10.1007/s00122-016-2691-5>
- 24- Teressa, Temesgen, Zigale Semahegn, and Tamirat Bejiga. 'Multi Environments and Genetic-Environmental Interaction (GxE) in Plant Breeding and Its Challenges: A Review Article' 7 (1 January 2021): 11–18. <https://doi.org/10.20431/2454-6224.0704002>
- 25- Pratap, Aditya, Sanjeev Gupta, Ramakrishnan Madhavan Nair, S. K. Gupta, Roland Schafleitner, P. S. Basu, Chandra Mohan Singh, et al. 'Using Plant Phenomics to Exploit the Gains of Genomics'. *Agronomy* 9, no. 3 (March 2019): 126. <https://doi.org/10.3390/agronomy9030126>
- 26- Sarkar, Sayantan, Alexandre-Brice Cazenave, Joseph Oakes, David McCall, Wade Thomason, Lynn Abbott, and Maria Balota. 'Aerial High-Throughput Phenotyping of Peanut Leaf Area Index and Lateral Growth'. *Scientific Reports* 11, no. 1 (4 November 2021): 21661. <https://doi.org/10.1038/s41598-021-00936-w>
- 27- Nomura, Koichi, Eriko Wada, Masahiko Saito, Hiromi Yamasaki, Daisuke Yasutake, Tadashige Iwao, Ikunao Tada, Tomihiro Yamazaki, and Masaharu Kitano. 'Estimation of the Leaf Area Index, Leaf Fresh Weight, and Leaf Length of Chinese Chive (*Allium Tuberosum*) Using Nadir-Looking Photography in Combination with Allometric Relationships'. *HortScience* 57, no. 7 (1 July 2022): 777–84. <https://doi.org/10.21273/HORTSCI16569-22>
- 28- El Haddad, Nouredine, Hasnae Choukri, Michel Edmond Ghanem, Abdelaziz Smouni, Rachid Mentag, Karthika Rajendran, Kamal Hejjaoui, Fouad Maalouf, and

- Shiv Kumar. 'High-Temperature and Drought Stress Effects on Growth, Yield and Nutritional Quality with Transpiration Response to Vapor Pressure Deficit in Lentil'. *Plants* 11, no. 1 (January 2022): 95. <https://doi.org/10.3390/plants11010095>
- 29- Jia, Jianxin, Yueming Wang, Jinsong Chen, Ran Guo, Rong Shu, and Jianyu Wang. 'Status and Application of Advanced Airborne Hyperspectral Imaging Technology: A Review'. *Infrared Physics & Technology* 104 (1 January 2020): 103115. <https://doi.org/10.1016/j.infrared.2019.103115>
- 30- Wang, Junjie, Yi Xu, and Guofeng Wu. 'The Integration of Species Information and Soil Properties for Hyperspectral Estimation of Leaf Biochemical Parameters in Mangrove Forest'. *Ecological Indicators* 115 (1 August 2020): 106467. <https://doi.org/10.1016/j.ecolind.2020.106467>
- 31- Pepe, Monica, Loredana Pompilio, Beniamino Gioli, Lorenzo Busetto, and Mirco Boschetti. 'Detection and Classification of Non-Photosynthetic Vegetation from PRISMA Hyperspectral Data in Croplands'. *Remote Sensing* 12, no. 23 (January 2020): 3903. <https://doi.org/10.3390/rs12233903>
- 32- Tagliabue, Giulia, Mirco Boschetti, Gabriele Bramati, Gabriele Candiani, Roberto Colombo, Francesco Nutini, Loredana Pompilio, et al. 'Hybrid Retrieval of Crop Traits from Multi-Temporal PRISMA Hyperspectral Imagery'. *ISPRS Journal of Photogrammetry and Remote Sensing* 187 (1 May 2022): 362–77. <https://doi.org/10.1016/j.isprsjprs.2022.03.014>
- 33- Damm, A., S. Cogliati, R. Colombo, L. Fritsche, A. Genangeli, L. Genesio, J. Hanus, et al. 'Response Times of Remote Sensing Measured Sun-Induced Chlorophyll Fluorescence, Surface Temperature and Vegetation Indices to Evolving Soil Water Limitation in a Crop Canopy'. *Remote Sensing of Environment* 273 (1 May 2022): 112957. <https://doi.org/10.1016/j.rse.2022.112957>
- 34- Genangeli, Andrea, Giorgio Allasia, Marco Bindi, Claudio Cantini, Alice Cavaliere, Lorenzo Genesio, Giovanni Giannotta, Franco Miglietta, and Beniamino Gioli. 'A Novel Hyperspectral Method to Detect Moldy Core in Apple Fruits'. *Sensors* 22, no. 12 (January 2022): 4479. <https://doi.org/10.3390/s22124479>
- 35- Sarić, Rijad, Viet D. Nguyen, Timothy Burge, Oliver Berkowitz, Martin Trtílek, James Whelan, Mathew G. Lewsey, and Edhem Čustović. 'Applications of Hyperspectral Imaging in Plant Phenotyping'. *Trends in Plant Science* 27, no. 3 (1 March 2022): 301–15. <https://doi.org/10.1016/j.tplants.2021.12.003>

- 36- Koh, Joshua C.O., Bikram P. Banerjee, German Spangenberg, and Surya Kant. 'Automated Hyperspectral Vegetation Index Derivation Using a Hyperparameter Optimisation Framework for High-Throughput Plant Phenotyping'. *New Phytologist* 233, no. 6 (2022): 2659–70. <https://doi.org/10.1111/nph.17947>
- 37- Thomas, Stefan, Jan Behmann, Angelina Steier, Thorsten Kraska, Onno Muller, Uwe Rascher, and Anne-Katrin Mahlein. 'Quantitative Assessment of Disease Severity and Rating of Barley Cultivars Based on Hyperspectral Imaging in a Non-Invasive, Automated Phenotyping Platform'. *Plant Methods* 14, no. 1 (8 June 2018): 45. <https://doi.org/10.1186/s13007-018-0313-8>
- 38- Stuart, Mary B., Matthew Davies, Matthew J. Hobbs, Tom D. Pering, Andrew J. S. McGonigle, and Jon R. Willmott. 'High-Resolution Hyperspectral Imaging Using Low-Cost Components: Application within Environmental Monitoring Scenarios'. *Sensors* 22, no. 12 (January 2022): 4652. <https://doi.org/10.3390/s22124652>
- 39- Islam, Rashedul, Boshir Ahmed, and Ali Hossain. 'Feature Reduction of Hyperspectral Image for Classification'. *Journal of Spatial Science* 67, no. 2 (4 May 2022): 331–51. <https://doi.org/10.1080/14498596.2020.1770137>
- 40- Morisse, Merlijn, Darren M. Wells, Emilie J. Millet, Morten Lillemo, Sven Fahrner, Francesco Cellini, Peter Lootens, et al. 'A European Perspective on Opportunities and Demands for Field-Based Crop Phenotyping'. *Field Crops Research* 276 (1 February 2022): 108371. <https://doi.org/10.1016/j.fcr.2021.108371>
- 41- Xie, Chuanqi, and Ce Yang. 'A Review on Plant High-Throughput Phenotyping Traits Using UAV-Based Sensors'. *Computers and Electronics in Agriculture* 178 (1 November 2020): 105731. <https://doi.org/10.1016/j.compag.2020.105731>
- 42- Di Gennaro, Salvatore Filippo, Piero Toscano, Matteo Gatti, Stefano Poni, Andrea Berton, and Alessandro Matese. 'Spectral Comparison of UAV-Based Hyper and Multispectral Cameras for Precision Viticulture'. *Remote Sensing* 14, no. 3 (January 2022): 449. <https://doi.org/10.3390/rs14030449>
- 43- Golzarian, Mahmood R., Ross A. Frick, Karthika Rajendran, Bettina Berger, Stuart Roy, Mark Tester, and Desmond S. Lun. 'Accurate Inference of Shoot Biomass from High-Throughput Images of Cereal Plants'. *Plant Methods* 7, no. 1 (1 February 2011): 2. <https://doi.org/10.1186/1746-4811-7-2>
- 44- Carron, T., and P. Lambert. 'Color Edge Detector Using Jointly Hue, Saturation and Intensity'. In *Proceedings of 1st International Conference on Image Processing*, 3:977–81 vol.3, 1994. <https://doi.org/10.1109/ICIP.1994.413699>

- 45- Sancho-Adamson, Marc, Maria Isabel Trillas, Jordi Bort, Jose Armando Fernandez-Gallego, and Joan Romanyà. 'Use of RGB Vegetation Indexes in Assessing Early Effects of Verticillium Wilt of Olive in Asymptomatic Plants in High and Low Fertility Scenarios'. *Remote Sensing* 11, no. 6 (January 2019): 607. <https://doi.org/10.3390/rs11060607>
- 46- Noh, Hyemin, and Jihyun Lee. 'The Effect of Vapor Pressure Deficit Regulation on the Growth of Tomato Plants Grown in Different Planting Environments'. *Applied Sciences* 12, no. 7 (January 2022): 3667. <https://doi.org/10.3390/app12073667>
- 47- Cassel, D. K., and D. R. Nielsen. 'Field Capacity and Available Water Capacity'. In *Methods of Soil Analysis*, 901–26. John Wiley & Sons, Ltd, (1986). <https://doi.org/10.2136/sssabookser5.1.2ed.c36>
- 48- Pereira, L., Alain Perrier, Richard Allen, and Isabel Alves. 'Evapotranspiration: Review of Concepts and Future Trends'. *Evapotranspiration and Irrigation Scheduling. Proc. Int. Conf.*, 1 January 1996, 109–15. <https://www.researchgate.net>
- 49- Basri, R., and D.W. Jacobs. 'Lambertian Reflectance and Linear Subspaces'. *IEEE Transactions on Pattern Analysis and Machine Intelligence* 25, no. 2 (February 2003): 218–33. <https://doi.org/10.1109/TPAMI.2003.1177153>
- 50- <http://www.arpab.it/idrometeorologico/indice4.asp>
- 51- Sadok, Walid, Jose R. Lopez, and Kevin P. Smith. 'Transpiration Increases under High-Temperature Stress: Potential Mechanisms, Trade-Offs and Prospects for Crop Resilience in a Warming World'. *Plant, Cell & Environment* 44, no. 7 (2021): 2102–16. <https://doi.org/10.1111/pce.13970>
- 52- Jureková, Zuzana, Kristína Németh-Molnár, and Viera Paganová. 'Physiological Responses of Six Tomato (*Lycopersicon Esculentum* Mill.) Cultivars to Water Stress', n.d., 7. <https://academicjournals.org/journal/JHF/article-full-text-pdf/7B337231843>
- 53- Rhodes, David, Sangita Handa, and Ray A. Bressan. 'Metabolic Changes Associated with Adaptation of Plant Cells to Water Stress 1'. *Plant Physiology* 82, no. 4 (1 December 1986): 890–903. <https://doi.org/10.1104/pp.82.4.890>
- 54- Nemeskéri, Eszter, and Lajos Helyes. 'Physiological Responses of Selected Vegetable Crop Species to Water Stress'. *Agronomy* 9, no. 8 (August 2019): 447. <https://doi.org/10.3390/agronomy9080447>
- 55- Patanè, Cristina, Simona Tringali, and Orazio Sortino. 'Effects of Deficit Irrigation on Biomass, Yield, Water Productivity and Fruit Quality of Processing Tomato under

- Semi-Arid Mediterranean Climate Conditions’. *Scientia Horticulturae* 129, no. 4 (27 July 2011): 590–96. <https://doi.org/10.1016/j.scienta.2011.04.030>
- 56- Quirino, Betania F, Yoo-Sun Noh, Edward Himelblau, and Richard M Amasino. ‘Molecular Aspects of Leaf Senescence’. *Trends in Plant Science* 5, no. 7 (1 July 2000): 278–82. [https://doi.org/10.1016/S1360-1385\(00\)01655-1](https://doi.org/10.1016/S1360-1385(00)01655-1)
- 57- Khan, Sher Hassan. ‘Effect of Drought Stress on Tomato Cv. Bombino’. *Journal of Food Processing & Technology* 06, no. 07 (2015). <https://doi.org/10.4172/2157-7110.1000465>
- 58- Janni, Michela, Nicola Coppede, Manuele Bettelli, Nunzio Briglia, Angelo Petrozza, Stephan Summerer, Filippo Vurro, et al. ‘In Vivo Phenotyping for the Early Detection of Drought Stres in Tomato’. *Plant Phenomics* 2019 (27 November 2019). <https://doi.org/10.34133/2019/6168209>
- 59- Schlemmer, M. R., D. D. Francis, J. F. Shanahan, and J. S. Schepers. ‘Remotely Measuring Chlorophyll Content in Corn Leaves with Differing Nitrogen Levels and Relative Water Content’. *Agronomy Journal* 97, no. 1 (2005): 106–12. <https://doi.org/10.2134/agronj2005.0106>
- 60- BOOCHS, F., G. KUPFER, K. DOCKTER, and W. KÜHBAUCH. ‘Shape of the Red Edge as Vitality Indicator for Plants’. *International Journal of Remote Sensing* 11, no. 10 (1 October 1990): 1741–53. <https://doi.org/10.1080/01431169008955127>
- 61- Steidle Neto, Antonio José, Daniela C. Lopes, Francisco A. C. Pinto, and Sérgio Zolnier. ‘Vis/NIR Spectroscopy and Chemometrics for Non-Destructive Estimation of Water and Chlorophyll Status in Sunflower Leaves’. *Biosystems Engineering* 155 (1 March 2017): 124–33. <https://doi.org/10.1016/j.biosystemseng.2016.12.008>

Chapter three

A Novel Hyperspectral Method to Detect Moldy Core in Apple Fruits

Premise

This chapter is published as a journal paper in the journal “*Sensors*”. The link to the full article is <https://www.mdpi.com/1424-8220/22/12/4479>

3.1 - Introduction

The apple production and post-harvest industry is among the largest fruit markets at the global scale, given the large diffusion and consumptions of apple fruits [1]. Final consumers are showing increasing attention towards food quality and sustainability of food supply chains, aiming to consume products with low environmental impact and homogeneous organoleptic characteristics without internal or external alterations [2]. Satisfying these requirements represents one of the main objectives for farmers and food-companies involved in the production and marketing of apples [3-5]. One of the most relevant causes of quality loss is represented by the internal browning in apple post-harvest phases caused by *Alternaria sp* (Asp), a ubiquitous genus fungorum widely present in all apple-growing areas.

The pathology caused by Asp is called mould core, or simply moldy core (MC) and initiates and produces its damage effects in the interior part of the fruits [6,7]. Previous studies have shown that the principal MC susceptible apple’s cultivar (cv) are represented by Fuji, Red Delicious and Granny Smith, but other significant varieties, such as Golden Delicious, can still present relevant internal damages by MC [8]. Indeed, apple cv Golden Delicious plays a fundamental role in the world apple industry, especially in Italy, where it is the most widely cultivated apple cv, with a total production volume of 858423 tonnes [9,10]. The damage by MC is an internal injury, with dry-brown areas developed in the inner part of fruit. The fruit does not present any external sign of damage, making MC detection with classical non-invasive methods very challenging or practically impossible [11].

Therefore, the development of non-invasive analytical methods to detect MC damages throughout the production process, especially in post-harvest phases deserves a great attention from producers.

Novel non-invasive approaches deriving from different technological sectors have been successfully tested and applied in recent years to detect internal injury or internal browning in apples, such as time-frequency images of vibro-acoustic signals [12,13]; magnetic resonance techniques [14,15] and x-ray analysis [16,17]. Thereby, these techniques deliver a meaningful occasion to explore innovative analysis methods capable to detect qualitative parameters in apples, but at the same time they show limitations due to their cost, size of equipment and operating time. Another innovative and promising solution with non-invasive methods for quality control in apple production has derived from recent developments by spectroscopy application from field to post-harvest phases [18,19]. Especially, the exploitation of light properties around the near infrared (NIR) region of the electromagnetic spectrum has captured the interest of researchers and industry in recent years, since it provides a valid alternative compared to invasive analysis methods [20,21]. Near infrared spectroscopy (NIRS) technics are based on the collection of spectral information such as absorption (ABS), reflectance (REF) and transmittance (TR) of electromagnetic signals in the spectral region spanning from 700 to 1200 nm [22]. REF based methods measure the reflected spectral signature under controlled illumination conditions and is typically used to retrieve parameters or compounds that are present on the fruit surface. REF was successfully used in several different applications, e.g., real-time quantification of biophysical and biochemical parameters through non-destructive method in citrus [23] and detection of oil palm maturity in bunches of fruits [24]. Techniques based on light reflectance in VIS/NIR have been successfully applied in apples quality control to detect a wide number of biophysical and biochemical parameters, such as external decay in apples [25], degrees brix [26], postharvest storage periods [27] and chlorophyll content [28]. ABS/ TR techniques are based on generating a convenient light source at one side of the fruit, that propagates across the interior of the fruit, being finally collected at a convenient escape sensing surface. In recent years, the improvement of efficient machine learning techniques (MLT) was permitted to develop innovative analysis models in different application areas, e.g. engineering science, modeling in geology and data reduction [29-31]. Moreover, MLT associated with TR analysis was successfully used in developing calibration models to quantify brix and pol at various stages of an industrial sugar production process [32]; therefore, the application of these

methods is a relatively new field in the agricultural post-harvest science. TR and MLT were applied sporadically on apples and other commercial fruits. Nevertheless, such methods were applied sporadically on apples while they were already successfully tested in different commercial fruits, e.g., TR techniques and convolutional neural network (CNN) were successfully applied in blueberry internal damage detection with classification accuracy over 80% [33]. Also, TR techniques represent an important analysis tool in high-income fruits, e.g., the grade of ripeness in nectarine (*Prunus Persica*) was evaluated with accuracy of 88 % by TR analysis in combination with Partial Least Square Regression (PLS-R) [34].

In the last few years, interest for MC detection by NIRS has increased in research activities and some different NIRS applications have been proposed. The main studies concerning the assessment of the capability to detect MC presence by VIS/NIR transmittance spectra retrieval were conducted mainly in cv Fuji. Zhaoyong et al. [35] verified MC presence in cv Fuji through an acquisition method based on multiple measurements per fruit; results obtained through the application of classifications algorithms based on back propagation artificial neural network (BP-NN) and support vector machine (SVM) have shown a classification accuracy of infected and healthy apples larger than 83%. Similarly, Shenderoy et al. [36] obtained a classification accuracy of healthy and infected apples larger than 90% by PLS-R in cv Fuji with a mouldy area larger than 5%. Tian et al. [37] investigated the relationship between the orientation of fruit trough light source position achieving best results with fruit stem-calyx axis horizontal and perpendicular to transmission belt in apples. These studies highlighted the high complexity of transmittance based hyperspectral NIR measurements, that are strongly affected by fruit and illumination geometry and by cv specific traits and chromatic characters, that strongly affect the measured spectral signatures. Results obtained on a specific cv are therefore likely not transposable to different ones.

The objective of this work was:

i) to develop and validate an innovative and low-cost application of NIRS to detect and monitor MC presence and growth in cv Golden Delicious through a novel measurement system based on a light source – light transmission – light collection architecture. An integrating sphere (IS) having homogeneous light reflectance properties [38] is adopted to compensate the geometrical variability in each fruit and toward the illumination geometry, and a low-cost VIS-NIR commercial spectroradiometer is used to measure the transmitted radiance inside the integrating sphere.

ii) to develop spectral based algorithms capable of detecting the MC and classifying the fruits in a binary classification framework (e.g classifying a fruit as healthy or moldy), based on several state of the art machine learning techniques: pattern recognition neural networks (ANN-AP), Logistic Regression (LR), Linear Support Vector Classification (SVC), Random Forest (RF), Naive Bayes (NB), K-Nearest Neighbor (KNN) and Bagging Classifier based on Decision tree (BC).

iii) to assess the temporal performance of the detection algorithms, i.e. to assess the amount of time after the inoculus at which it becomes detectable.

iv) to assess the sensitivity of the algorithms, i.e. the minimum amounts of infected tissues can be detected.

v) to determine the most important spectral bands responsible for the MC detection, and the minimum number of bands that can be used to further develop low-cost-multispectral rather than hyperspectral detectors.

Finally, the technological and industrial implications of the proposed sensing technology are discussed.

3.2 Materials and Methods

3.2.1- Instrument setup

The prototype measurement system to detected MC in apples presented here is called Apple Light Transmittance System (ALT-S) and is shown in Figure 1. It consists of a box (1) where on his top was inserted a polystyrene integrating sphere (2) with 160 mm diameter and 50 mm thickness. The sphere was externally covered with an aluminum foil to remove external light noise. The inner part of the sphere is made of polystyrene and was assumed to have white-body-like properties such as an integral spectral signature that is independent from the light geometry. The fruit (3) is placed on the base of the IS and it is detained by a neoprene gasket with 60 mm diameter (4) between the sphere and a vacuum chamber (5). The vacuum chamber is a negative pressure space that has the function of sucking the fruit to obtain a complete adherence to the gasket, thus avoiding the possibility of having photons that escape and reach the sphere and the detector without passing through the fruit core. The chamber is made of a connecting pipe (6) which connects the vacuum chamber to a vacuum pump (7), in turn connected to the outside of the box through a gasket (8). The fruit is illuminated by a NIR 40 W light source (9) placed at the base of the vacuum chamber. The NIR light source spectral range start from 770 nm to 920 nm. Spectral data were collected by an Ocean Optics USB2000

spectrometer (Ocean Insight, Rochester, NY, USA) with a spectral sampling interval ranging from 350 to 1000 nm and around 0.3 nm of spectral resolution, and internally based on a Sony ILX511 linear silicon CCD array (11-12). The apparatus was controlled by an industrial PC and data have been collected by Ocean View software (*Ocean Insight, Rochester, NY, USA*) (13). Light source and all the devices were powered by a 12V power supply (10). At the beginning and at the end of every acquisition round, a white Delrin™ sphere, 80 mm diameter, was placed over the neoprene gasket in the same way as fruits, to collect reference transmittance spectra to be used to derive transmittances for all the measurements of that round. The use of such a reference sphere was necessary to obtain a reference spectra comparable with the magnitude of fruit spectra without changing the exposure interval of the spectroradiometer.

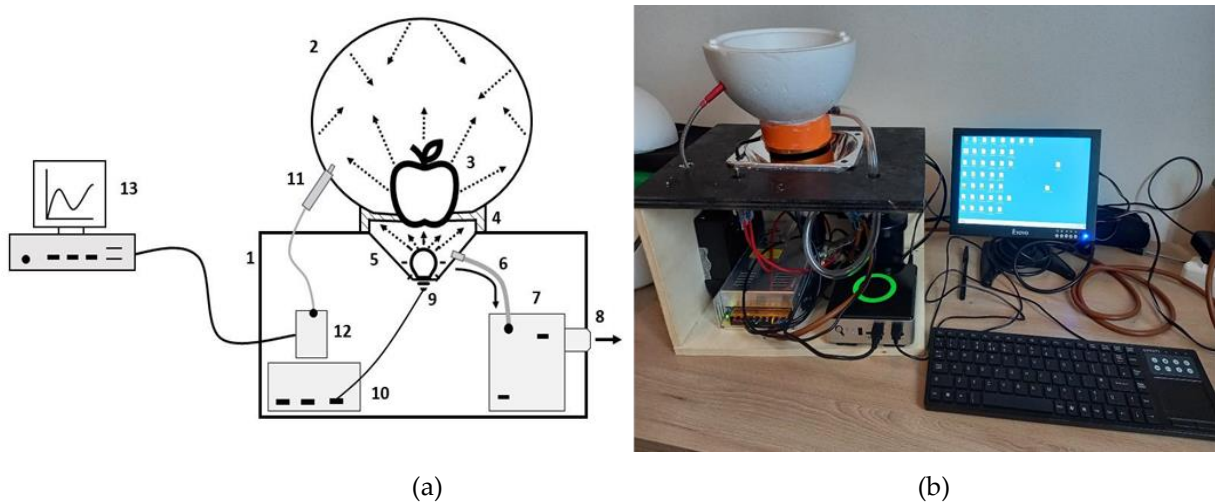


Figure 1. ALT-System (Apple Light Transmittance System) operation diagram (a) and ALT-System at working (b).

3.2.2- Experimental measurements

The experiment was made at CNR (National Research Council of Italy) facility in Follonica (Italy) in April 2021. Seventy apples cv Golden Delicious at commercial maturity were collected from the mass retail channels and were stored in two plastic boxes having a size 50 x 40 cm, thirty-five apples per box. Apples were inoculated with *Alternaria alternata* spp., one of the most representative fungi responsible for MC disease in according to the replication and inoculation methodology already used by Ntasiu et al. [8]. The *Alternaria* was sampled by cv Golden Delicious in Valsugana (TN, Italy), and it

was characterized and preserved by Edmund Mach Foundation of San Michele All'Adige (TN, Italy). The culture of pathogens was flooded with 5 ml of sterile distilled water and the conidia were scraped off with a surgical blade. The resulting conidial suspension was filtered through two layers of cheesecloth to remove mycelial fragments. Prior to inoculation, apple fruit surface was disinfected for 5 min by drenching them in a 1% NaOCl solution. The fruit were artificially inoculated by aseptically injecting 100 ul of a conidial suspension through the calyx into the fruit core with a syringe. Then, boxes were stored in a climatic chamber at 26°C and 40 ml of water was added to each box that was covered to maintain relative humidity over 70%. Each sample was measured with the ALT-S every 3 days for 5 times for a total duration of the experiment (Table 1).

Table 1. Experiment timetable.

Days	Round	Operations
02/04/ 2021	1	Biometrical measurement, Inoculation, and spectral acquisition
05/04/ 2021	2	Spectral acquisition
08/04/2021	3	Spectral acquisition
11/04/2021	4	Spectral acquisition
14/04/2021	5	Spectral acquisition, biometrical measurement, MC presence validation and RGB acquisition

The operational analysis time (positioning of the fruit in the sphere and spectral acquisition) was approximately 90 seconds for each sample. Apples were sampled every time in two different positions, vertically (T1) and horizontally (T2) with respect to the NIR light source location. A total amount of 700 spectra signatures was collected in this way (70 samples x 5 times x 2 positions). After the final spectral acquisition, all fruits have been cut to check the growth of MC and the degree of its development. Fruits were positioned in an image acquisition platform to acquire RGB images to retrieve information about the amount of rotten versus healthy surface. The rotten area expressed as a percentage of the total cutted area was retrieved with a threshold-based segmentation method operated in MatlabR2021a (MahtWorks, USA) using Image Processing Toolbox. Biometrical data such as weight, volume, height, maximum and minimum diameter at the beginning and end of the experiment were collected. The MC data consisted of 70 values determined at the end of the experiment.

3.2.3 Transmittance retrieval

The entire spectral dataset was composed of 700 spectral signatures of 2048 wavelengths (WL) ranging from 350 to 1000 nm. Only the spectral wavelengths within the range of the NIR light source were selected for the analysis, resulting in 750 bands from 770 nm to 920 nm. The set of 70 fruits was sampled in T1 and T2 positions for 5 measurement rounds. The spectral data were collected in absolute irradiance ($\mu\text{W}/\text{nm}/\text{cm}^2$) and the spectral transmittance (TR) computed as the ratio:

$$\text{TR} = \text{FRad} / \text{RRad} \quad (1)$$

Where FRad is the radiance obtained by the photons transmitted through the fruit and RRad the radiance obtained by the photons transmitted through the Delrin sphere reference target.

3.2.4 Band ratios and average transmittance

A preliminary analysis was made to explore the acquired spectral dataset and verify the existence of a significant relation between MC measured at the end of the experiment and the spectral data measured at the 5-time steps along the experiment duration. The presence of such relation can be considered as a prerequisite for the application of more complex machine learning classification methods, and may serve as an indirect estimate of the timing of the MC development by exploring different time steps. A simple band ratio index was computed for all possible combinations of couples of spectral bands transmittance ranging between 800 and 880 nm, separately for each fruit, each position, and each time step. Then the correlation coefficient between MC data (70 samples) and the multiple band ratios for the 70 fruits was computed for each measurement round and position, obtaining a correlation map for each round.

Furthermore, the average transmittance was computed for all the fruits belonging to the two classification categories (healthy and moldy), for each round, to derive additional qualitative indicators of the presence of spectral features associated to moldy state.

3.2.5 Binary Classification

The overall objective of this study was to develop and test different binary classification models. The label-encoding was adopted assigning label 1 to moldy samples in relationship with the MC presence and label 0 to healthy samples. The spectral dataset was divided in one training dataset and four test datasets, where round 5 was used to train

the model and rounds 1,2,3 and 4 were used as test. In all the classification models developed here, each WL represented an independent variable (IV) while the MC state represented the target variable to be predicted. Different binary classifiers were evaluated by computing performance metrics on accuracy, precision and recall commonly used in machine learning models [39]. The performance metric was estimated by computing the confusion matrix on the training dataset [40]. By the definition of the confusion matrix, C is such that $C_{i,j}$ is equal to the number of observations known to be in group i and predicted to be in group j. Thus, in binary classification the count of true negatives is $C_{0,0}$, false negatives is $C_{1,0}$, true positives is $C_{1,1}$ and false positives is $C_{0,1}$. Therefore, the performance metrics were obtained to evaluate the best classifiers and to compare them.

Supervised classification models

Multiple supervised classification models (MSCM) based on the scikit-learn python library [41] were evaluated in this study; respectively: LR, SVC, RF, NB, KNN and BC [42,43]. The model parameters of the RF, NB, KNN and BC were optimized by cross-validated grid-search over a parameter grid [44]. The best performing model was selected, and then further improved by a dimensionality reduction aimed at reducing the number of independent variables. In fact, the presence of redundant information in the spectral data can distort classification results [45]. In classification problems some statistical techniques can be used to minimize redundant data [46]. Here, we applied a univariate feature selection, as univariate statistical test to select k features that have the strongest relationship with the output variable. To select a specific k number of features, the ANOVA F-value method [47] via the Sklearn `f_classif()` function was used, while a grid search was implemented for the tuning of k [48].

Pattern Recognition Neural Network

A binary classification model based on ANN-AP was developed using MatlabR2021a Pattern Recognition Toolbox (MathWorks, USA). Backpropagation with Momentum Algorithm (BMA) represents a powerful tool to resolve non-linear problems and it was selected to train the network [49,50]. BMA is a particular class of backpropagation algorithms where the input units are propagated forward to the output layer through the connecting weights. An accurate description of BMA can be found in the work of Phansalkar et al. [51]. The network's architecture was developed in accordance with

backpropagation rules and it was formed by 252 input, one layer with 252 hidden layers, one layer with two hidden layers and two output labels. The train function ‘traingdm’ based on Fletcher-Powell Conjugate Gradient was used. The limit of training periods was set at 600 epochs. Other settings have been set at their default values.

3.3 Results and discussion

3.3.1 Infection rate

The infection rate was computed at the end of round 5 by destructive samplings and image segmentation. Results showed an infection rate of 54.2% (38 fruits over 70) against 45.8% of samples remained healthy (33fruits over 70). Based on the segmentation results, all the 70 samples were classified by the infection rate (Figure 2).

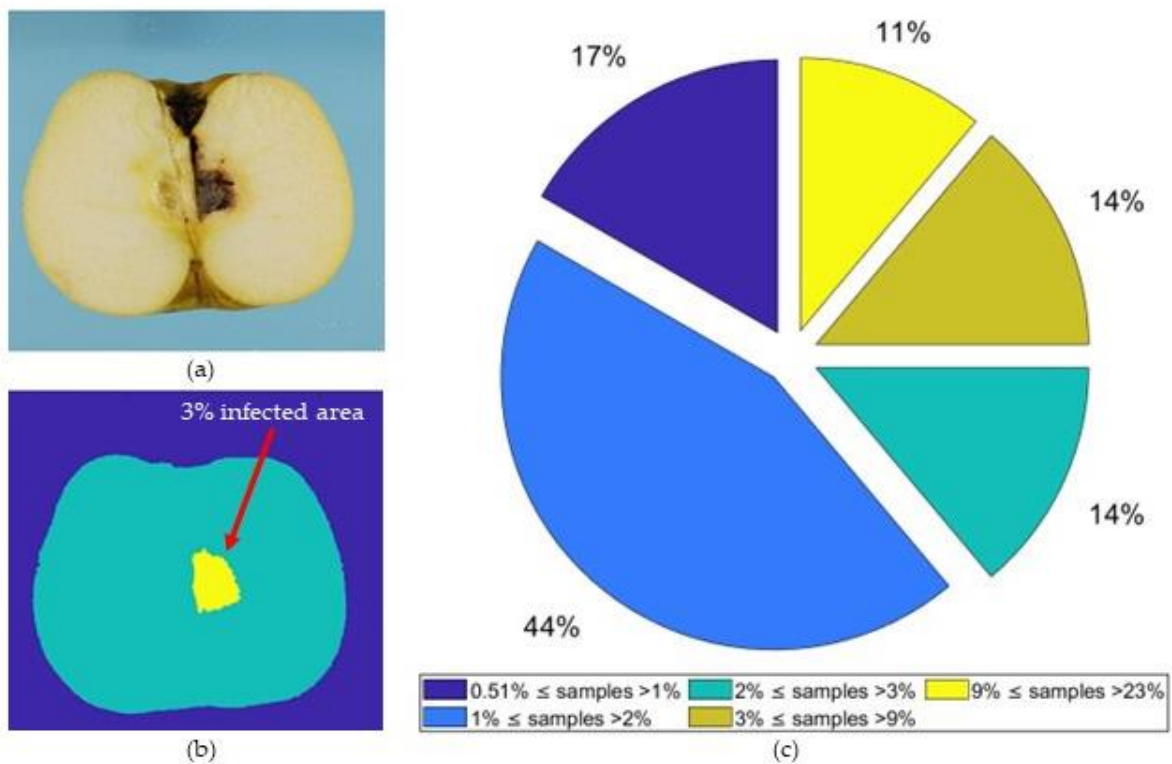


Figure 2. Example of segmentation results in a sample with a 3.0% infection rate.

RGB image (a) was isolated from background, the results obtained (b) was furthermore processed to obtain necrotic area (yellow) separated from healthy area (light blue). Infection results grouped into classes based on infection levels (c).

A relevant fraction of the infected samples (44%) had an infection level between 1% to 2% (Fig. 2c). This condition made it possible to select an infection threshold of 0.51% to balance the number of samples labelled as healthy and moldy (respectively 35 moldy and 35 healthy samples) in the binary classification training dataset. The choice of the infection threshold represents a critical issue in MC early detection [52] and has economic and industrial implications. The selection of a relatively large threshold on the one hand would facilitate the development of good classification algorithms, but on the other hand would carry the risk to classify fruits with infection rates lower than the threshold as healthy, which has relevant negative industrial impact [53]. The threshold selected here is remarkably low, improving over ten-times the minimum infection level used in similar previous study [35]. Keeping the minimum detectable infection at a low value represents a primary challenge for the performance assessment of the machine learning based methods presented here.

3.3.2 -Spectral correlations

The maps of correlation between transmittance band ratios and MC across all possible permutations of couples of bands was computed in T1 and T2 fruit positions and for each time step (Figure 3).

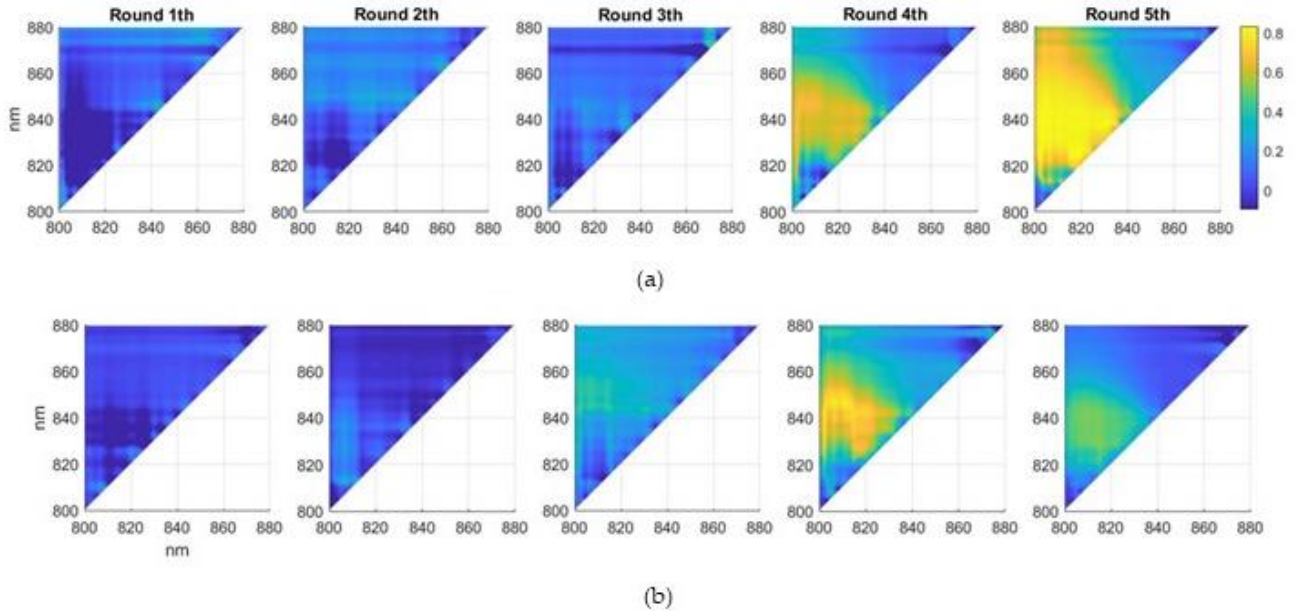


Figure 3. Maps of the correlation coefficient between MC measured at the end of the experiment (round 5), and transmittance ratios T_x/T_y based on two individual bands, computed on all combinations of x and y ranging over the sampled spectral interval [800-880 nm] or each round (1 to 5). Panels (a) and (b) refer to T1 and T2 positions respectively.

These maps show the absence of any significant correlation at round 1 and 2 in both T1 and T2 positions, with values contained within -0.2 to 0.2 not associated with any consistent pattern. This result is likely related to the absence of infection at these early stages of the experiment. At round 3, correlations are still very low for T1 position, while they reach values of 0.43 in T2 position, likely indicating that spectral proxies of the infection progress started to be detectable at this stage. The presence of a distinctive higher correlation region was then observed at round 4 and then round 5, with maximum correlation values in T1 position of 0.67 and 0.82 and 0.74 and 0.51 in T2 position. This evidence supports the hypothesis that MC is developing within the fruits between round 1 and round 3, it is partially developed and detectable at round 4 and fully developed at round 5, when the destructive sampling and MC determination were made. The spectral

bands whose ratio was associated with the maximum correlation are very similar in round 4 and 5, at 850 nm and 805 nm in round 4, and 849 nm and 802 nm in round 5.

Correlations between band ratios and MC in T1 position (vertical) are remarkably higher than in T2 position (horizontal), revealing that the measurement position influences the MC detection capability by affecting the spectral geometry. The explanation for this difference is likely related to the geometric symmetry of apple fruits along the vertical axis, that reflects in anisotropic conditions and photons homogeneously passing through the internal of the fruit. On the other hand, the fruit placed in horizontal position is not symmetrical along the vertical axis aligned with the light source, likely generating fruit specific geometric conditions affecting the light penetration and the spectral sampling. Given this difference in the performance, only the spectra retrieved in T1 position were selected for the subsequent analysis and machine learning classification.

3.3.3 - Transmittance temporal pattern

The average spectral transmittance pattern in T1 position was obtained for each round (Figure 4).

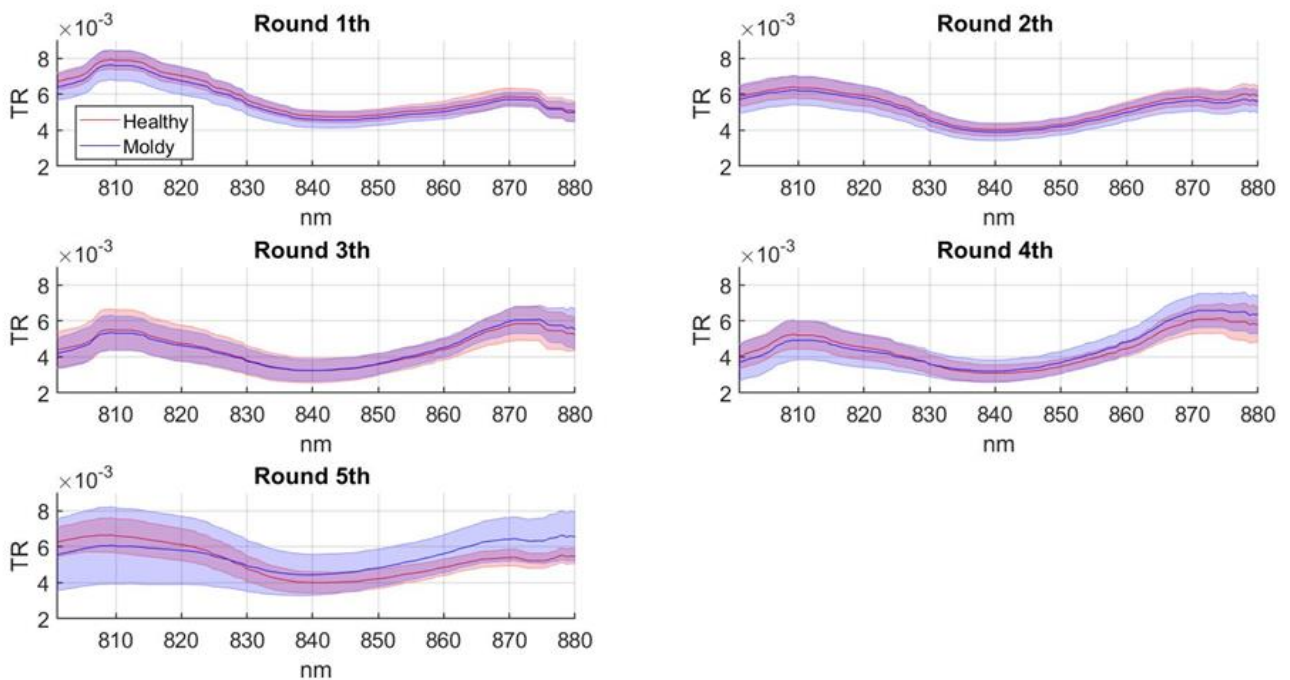


Figure 4. Temporal pattern of mean transmittance for healthy and infected samples with a threshold infection level of 2% or more. Transmittance was first averaged across all wavelengths and then mean and standard deviation were computed.

In round 1 and 2, the TR curve does not show any significant difference between healthy and moldy samples. In round 3, the magnitude of TR from 860 nm to 880 nm increased in infected samples more than in healthy ones. In round 4 the difference in TR between healthy and moldy samples is further accentuated, especially from 800 to 820 nm and from 850 to 880 nm. In round 5 results show the maximum TR difference between healthy and moldy samples. The standard deviation of the infected population increases significantly compared to healthy samples. In addition, round 5 shows an increase of infected population's transmittance from 825 to 880 nm. Similar studies were conducted on Fuji apples by Tian et al. and Zhaoyong et al. [36,34]. Tian et al. measured in moldy samples an increase of TR in the spectral region from 775 to 830 nm and decrease from 830 to 880 nm; In contrast, Zhaoyong et al. showed a decrease of TR in moldy samples from 700 to 820 nm. Generally, the Transmittance temporal pattern obtained in our work shows a decrease of TR in moldy samples from 800 to 830 nm and an increase from 830 to 880 nm, in contrast to Tian et al. results and in accord to Zhaoyong et al. result. The difference in results might be due to the different apple varieties used in previous spectroscopy analysis. Indeed, apple varieties present morphological differences such as their texture, skin color and chemical composition and the spectral response results inevitably influenced by these characteristics [54]. In addition, TR differences encountered in several studies might also depend on the large number of pathogens related to MC disease [7]; Therefore, a precise taxonomic classification of the detected pathogens would be recommended.

3.3.4- Binary classification and ANN-AP

Based on ANOVA univariate results, F-value was computed in round 5 to select a specific k number of features to reduce the redundant information (Figure 5).

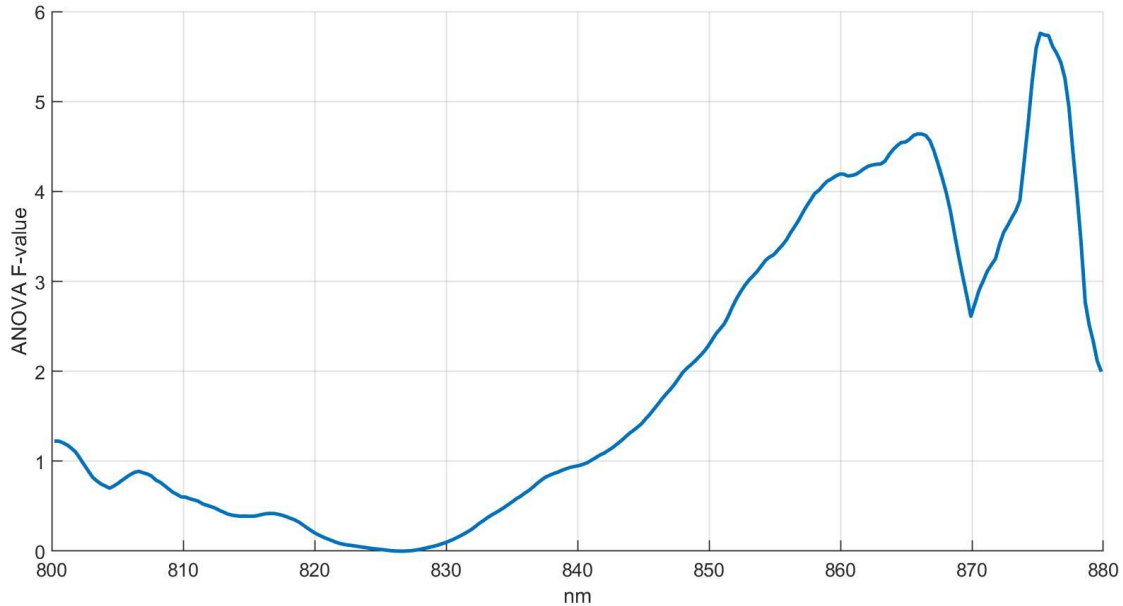


Figure 5. ANOVA F-value results from 800 to 880 nm. F-value is a ratio between two variance and a higher F-value corresponds to a significant statistical mean separation between healthy and moldy groups.

Results show a constantly increasing pattern of F-value from 830 nm to 866 nm, followed by a decrease and then a remarkable increase from 870 to 878 nm. Figure 5 shows two peaks in the spectral region from 860 to 878 nm caused by a larger variance in the spectral region from 860 to 880 nm. The F-value increases significantly from 860 to 878 nm in accordance with the increase of TR (Figure 4) obtained in Temporal pattern results to the same spectral range and round. Therefore, spectral bands characterized by larger F-value indicate the spectral features most influenced by MC presence. Results obtained by ANOVA analysis allowed the reduction of the spectral range in MSCM training from 863.38 to 877.69 nm.

Several MSCM and one ANN-AP were assessed in this study. Between MSCM, the BC reported the best training score in accuracy and precision; consequently, classification results obtained from BC and ANN-AP were compared. Training results are shown in Table 2.

Table 2. BC model and ANN-AP training results. The Binary classification models were trained on round 5 and the performance metrics (accuracy, precision and recall) were computed by confusion matrix.

Model	Accuracy	Precision	Recall
BC	0.95	0.85	0.88
ANN-AP	0.72	0.89	0.62

ANN-AP reported a higher level of precision (0.89) while BC model reported a higher level of accuracy (0.95) and recall (0.88). The accuracy measures the number of correct predictions made divided by the total number of predictions made. The precision is the number of true positives divided by the number of true positives and false positives. The recall is the ability to find all relevant instances (intuitively the ability of the classifier to find all the positive samples). The higher level of accuracy and recall reported by the BC model shows a better ability to classify correctly samples labeled (both positives and negatives) in comparison to the ANN-AP model. However, the higher level of precision reported by ANN-AP suggests a better ability to find positive instances. Indeed, a high score of precision reflects a high degree of discrimination between positive and false positive samples in training set. The precision score obtained in the training set confirms the higher capability to classify a low number of false positive by ANN-AP, as already reported in literature concerning the hyperspectral classification based on decision tree and neural network [55,56]. The importance of high precision in the training set is accentuated in a quality control industrial context, where the identification of infected samples has the greatest impact compared to the elimination of healthy samples. Therefore, failures in correctly detecting infected samples leads to a direct damage for the end consumers which require healthy and standardized products. Differences in classification results by ANN-AP and BC models can be due to their different processing of the input variable. Indeed, ANN-AP is an algorithm inspired by biological neural networks instead BC is based on a top-down approach of looking at the data. In ANN-AP the value of the weights selected during the training process and the training goal is to minimize the error between values predicted by ANN-AP and true values [57]. The BC model uses a binary tree graph to assign for each data sample a target value and the target

values are presented in the tree leaves. To reach the leaf the sample is propagated through nodes [58].

The two models, calibrated in round 5, were then tested on the previous rounds to assess them on completely independent datasets, also characterized by a different (e.g lower) level of MC compared to the level used to train the models. Classification results on previous rounds are reported in figure 6.

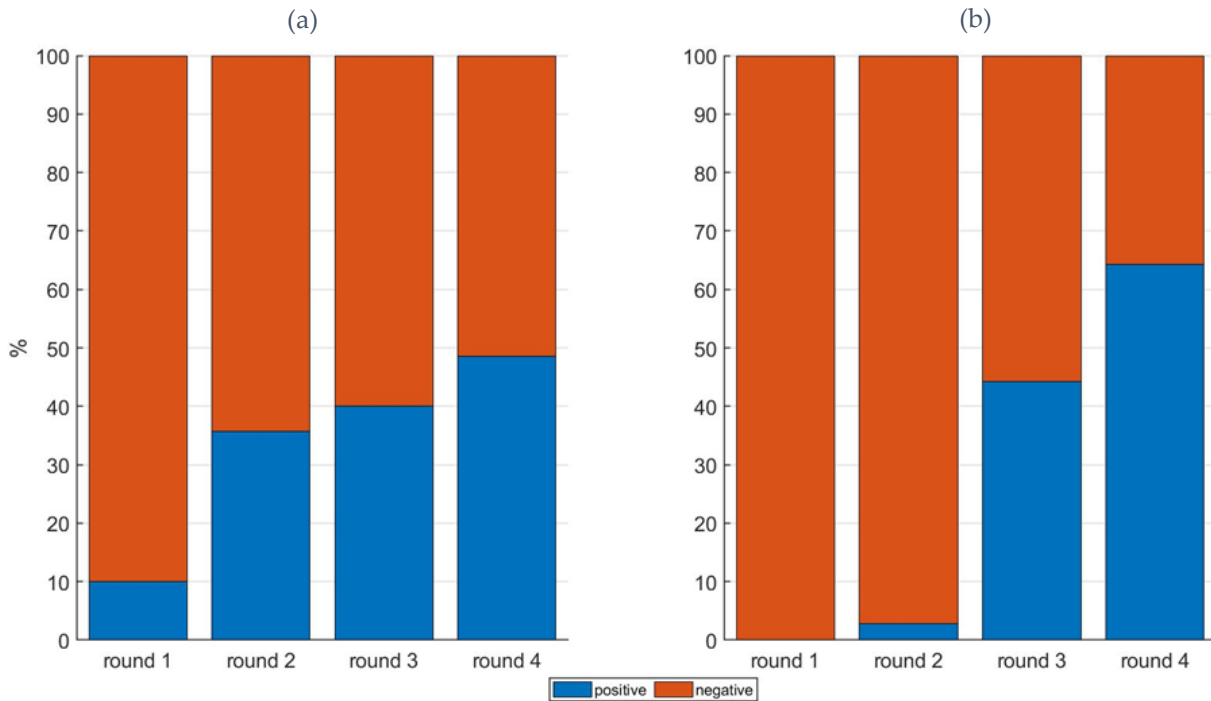


Figure 6. BC model (a) and ANN-AP (b) test results in round 1,2,3,4. The Binary classification results on unlabeled datasets show two classes, respectively infected (positive) and healthy (negative).

The two models were trained on round 5 with a threshold infection rate of 0.51%; therefore, the number of positive samples and negative in training set resulted of 35 and 35 (50% positive and 50% negative), respectively.

Overall, results obtained from both the BC and ANN-AP models exhibit an increase over time of the amount of detected infected samples; this behavior is in agreement with an expected exponential development of the infection [59]. The lowest number of positive samples was detected in round 1, respectively 10% in BC model and 0% in ANN-AP. At

round 1 a condition of complete absence of the infection was likely present, given that the inoculus was just applied at the beginning of the experiment. This condition is only met with the ANN-AP model, while the BC model reported a relatively large number of false positives (7 samples classified as positive). In round 2 the BC and the ANN-AP models detected an amount of 35.72% and 2.85% of positive samples, respectively. The temporal proximity of round 2 from to the inoculation time (6 days) discourages the hypothesis that a high level of infection was reached. The correlation maps (Figure 3) and the average transmittance patterns (Figure 4) also support the hypothesis of a complete absence of infection at round 2. Therefore, BC model is likely reporting a large number of false positives while ANN-AP is performing properly. This difference can be attributed to ANN-AP learning skills, that better adapt to new data patterns and reveal a higher capacity to interpret non-linear problems, as reported in the literature from Rojas and Abiodun et al. [60,61]. In round 3 the percentage of detected positive samples resulted similarly in the two models, at 40 % and 44% for BC and ANN-AP, respectively.

Both models suggest the presence of the infection at round 3, a finding that is supported by the correlation maps (Figure 3) and transmittance patterns (Figure 4), which reveal the first signs of the MC presence at this stage. It is possible that the machine learning methods have a higher specificity compared to a simple band ratio or an average transmittance pattern and detect an actual starting of the infection more effectively. Nevertheless, the possibility of these methods reporting false positives at this stage cannot be ruled out, and further research is needed to verify the actual infection rate at an early stage by destructive samplings that could be done only at the end of the experiment.

In round 4, 48.57% and 64.29% of samples were classified as positives in the BC and ANN-AP models, respectively; a large spread of infected samples at this stage is also confirmed by the correlation maps (Figure 3) and the average Transmittance patterns that are significantly different between infected and healthy samples (Figure 5). Based on MC presence in round 5, the ANN-AP shows an overestimation of positive classifications. Overall, the classification models trained in this study might exhibit a possible uncertainty due to the limited size of the dataset [62].

This analysis gives insight on the model capability to detect MC at different development stages and it provides information about the model general applicability in real post-harvest condition. As already discussed, in industrial context the economic damage for primary producers due to the inputs of the infected samples in large scale retail trade is greater than the damage associated to the healthy product discard.

The BC model, while having an overall good classification capacity on the training dataset (Table 2), reported a large fraction of false positives at previous time steps while used in testing mode. This characteristic prevents its application in industrial detection given that the amount of infection and the temporal stage of the infection process are generally unknown. The ANN-AP model, on the other hand, exhibited both a good precision on the training dataset, and a consistent reproduction of the infection rates and development on the testing datasets, therefore resulting to have a greater potential for industrial applicability. This potential should be further confirmed and assessed by means of further research deploying a significantly larger number of sampled and inoculated fruits, also encompassing infection variability across different cultivars.

3.4 - Conclusions

This study proposes a novel early detection system based on NIRS technologies to detect MC in cv Golden Delicious apples. The measurement device, called ALT-System, was successfully developed and tested on a set of infected samples. The ALT-System has demonstrated its capability to detect MC through one single measurement per fruit surpassing the previous measurement systems that were requiring repeated measurements. Therefore, the achievement of this goal represents an important starting point to develop an efficient industrial prototype. In this study, spectral features linked to the MC presence were identified in the spectral region from 863.38 to 877.69 nm, and the spectral differences in term of TR between healthy and infected samples were explained over five different measurement rounds during the development of the infection. Several binary classification methods based on decision trees and ANN methods were tested here. ANN-AP and BC models were the two best methods with a better score in terms of performance metrics as accuracy, precision and recall. Moreover, their performance in training and validation datasets were assessed and discussed. By comparing training results between the two methods, the ANN-AP training results exhibited the best score in precision (0.89), a parameter whose optimization is mostly associated with the industrial needs of fruits post-harvest processing. Indeed, an efficient capability to distinguish healthy samples is a primary requirement to develop a functional industrial detection system. BC and ANN-AP models were tested on independent datasets obtained at previous stages of the infection development, and the ANN-AP showed a better classification result in relation to the infection growth rate. Indeed, ANN-AP showed a predictive accuracy of 100% at round 1 and 97.15% at round 2, demonstrating a better

capability compared to BC model to interpret unknown datasets. Classification errors reported here might be related to the small dataset size and a low infection threshold adopted.

In industrial context, MC early detection through non-invasive methods remains a critical issue, and this work represents a starting point to develop an industrial-scale prototype based on NIRS. Further studies are recommended to develop a measurement system capable to overcome the limits of the ALT-System: i) inability to measure multiple fruits simultaneously ii) need to minimize the measurement time per fruit. In addition, further investigations are needed to integrate the ALT-System directly on a conveyor belt. Additional spectral tests on multiple apple varieties are also recommended to explore the link between skin color, texture, biochemical contents and spectral response. Finally, the technology and methods used and developed in this work might be applied in other apple diseases detection, e.g. biotic and abiotic internal browning or post-harvest CO₂ damages, and show a high potential for application to other fruits.

References

1. Aksoy, M. Ataman, John C. Beghin, All Rights Reserved, M. Ataman Aksoy, and John C. Beghin. 'Fruits and Vegetables: Global Trade and Competition in Fresh and Processed Product Markets'. The World Bank Washington, D.C. (2005): 237-243. <https://doi:10.1017/S1474745606232877>.
2. Jaeger, Sara R., Lucía Antúnez, Gastón Ares, Marianne Swaney-Stueve, David Jin, and F. Roger Harker. 'Quality Perceptions Regarding External Appearance of Apples: Insights from Experts and Consumers in Four Countries'. *Postharvest Biology and Technology* 146 (1 December 2018): 99–107. <https://doi.org/10.1016/j.postharvbio.2018.08.014>.
3. El Khaled, D., N.N. Castellano, J.A. Gazquez, R.M. García Salvador, and F. Manzano-Agugliaro. 'Cleaner Quality Control System Using Bioimpedance Methods: A Review for Fruits and Vegetables'. *Journal of Cleaner Production* 140 (January 2017): 1749–62. <https://doi.org/10.1016/j.jclepro.2015.10.096>
4. Granatstein, David, Elizabeth Kirby, Harold Ostenson, and Helga Willer. 'Global Situation for Organic Tree Fruits'. *Scientia Horticulturae*, Recent advances in organic horticulture technology and management - Part 1, 208 (29 August 2016): 3–12. <https://doi.org/10.1016/j.scienta.2015.12.008>.
5. O'Rourke, A. Desmond. *The World Apple Market*. Boca Raton: Routledge, 2018. <https://doi.org/10.1201/9780203719091>.
6. Elfar, Karina, Juan P. Zoffoli, and Bernardo A. Latorre. 'Identification and Characterization of *Alternaria* Species Associated with Moldy Core of Apple in Chile'. *Plant Disease* 102, no. 11 (1 November 2018): 2158–69. <https://doi.org/10.1094/PDIS-02-18-0282-RE>.
7. Gao, L. L., Q. Zhang, X. Y. Sun, L. Jiang, R. Zhang, G. Y. Sun, Y. L. Zha, and Alan R. Biggs. 'Etiology of Moldy Core, Core Browning, and Core Rot of Fuji Apple in China'. *Plant Disease* 97, no. 4 (4 October 2012): 510–16. <https://doi.org/10.1094/PDIS-01-12-0024-RE>.
8. Ntasiou, Panagiota, Charalampos Myresiotis, Sotiris Konstantinou, Euphemia Papadopoulou-Mourkidou, and George S. Karaoglanidis. 'Identification, Characterization and Mycotoxigenic Ability of *Alternaria* Spp. Causing Core Rot of Apple Fruit in Greece'. *International Journal of Food Microbiology* 197 (16 March 2015): 22–29. <https://doi.org/10.1016/j.ijfoodmicro.2014.12.008>

9. Italian Institute of Statistics. Available online: <https://www.istat.it/> (accessed on 18/05/2022)
10. Italian association of apple producers. Available online: <http://www.assomela.it> (accessed on 18/05/2022)
11. Basson, Elaine, Julia C. Meitz-Hopkins, and Cheryl L. Lennox. 'Morphological and Molecular Identification of Fungi Associated with South African Apple Core Rot'. *European Journal of Plant Pathology* 153, no. 3 (March 2019): 849–68. <https://doi.org/10.1007/s10658-018-1601-x>.
12. Zhang, Hui, Zhihua Zha, Don Kulasiri, and Jie Wu. 'Detection of Early Core Browning in Pears Based on Statistical Features in Vibro-Acoustic Signals'. *Food and Bioprocess Technology* 14, no. 5 (1 May 2021): 887–97. <https://doi.org/10.1007/s11947-021-02613-2>
13. Zhao, Kang, Zhihua Zha, He Li, and Jie Wu. 'Early Detection of Moldy Apple Core Based on Time-Frequency Images of Vibro-Acoustic Signals'. *Postharvest Biology and Technology* 179 (1 September 2021): 111589. <https://doi.org/10.1016/j.postharvbio.2021.111589>
14. Chayaprasert, Watcharapol, and Richard Stroschine. 'Rapid Sensing of Internal Browning in Whole Apples Using a Low-Cost, Low-Field Proton Magnetic Resonance Sensor'. *Postharvest Biology and Technology* 36, no. 3 (1 June 2005): 291–301. <https://doi.org/10.1016/j.postharvbio.2005.02.006>.
15. Cho, Byoung-Kwan, Watcharapol Chayaprasert, and Richard L. Stroschine. 'Effects of Internal Browning and Watercore on Low Field (5.4MHz) Proton Magnetic Resonance Measurements of T2 Values of Whole Apples'. *Postharvest Biology and Technology* 47, no. 1 (1 January 2008): 81–89. <https://doi.org/10.1016/j.postharvbio.2007.05.018>.
16. Dael, M. van, P. Verboven, A. Zanella, J. Sijbers, and B. Nicolai. 'Combination of Shape and X-Ray Inspection for Apple Internal Quality Control: In Silico Analysis of the Methodology Based on X-Ray Computed Tomography'. *Postharvest Biology and Technology* 148 (1 February 2019): 218–27. <https://doi.org/10.1016/j.postharvbio.2018.05.020>.
17. Hu, Wenyan, Jiangtao Li, Xiaoqiong Zhu, Zhongyi Wang, Daqing Piao, and Longlian Zhao. 'Nondestructive Detection of Underlying Moldy Lesions of Apple Using Frequency Domain Diffuse Optical Tomography'. *Postharvest Biology and*

- Technology 153 (July 2019): 31–42.
<https://doi.org/10.1016/j.postharvbio.2019.03.014>
18. Cen, Haiyan, and Yong He. ‘Theory and Application of near Infrared Reflectance Spectroscopy in Determination of Food Quality’. *Trends in Food Science & Technology* 18, no. 2 (1 February 2007): 72–83.
<https://doi.org/10.1016/j.tifs.2006.09.003> .
 19. Sirisomboon, Panmanas. ‘NIR Spectroscopy for Quality Evaluation of Fruits and Vegetables’. *Materials Today: Proceedings, International Conference on Advances in Science & Engineering ICASE -2017, 19th – 22nd January 2017*, 5, no. 10, Part 3 (1 January 2018): 22481–86. <https://doi.org/10.1016/j.matpr.2018.06.619>
 20. Cattaneo, Tiziana M. P., and Annamaria Stellari. ‘Review: NIR Spectroscopy as a Suitable Tool for the Investigation of the Horticultural Field’. *Agronomy* 9, no. 9 (September 2019): 503. <https://doi.org/10.3390/agronomy9090503> .
 21. Tan, Jin Yeong, Pin Jern Ker, K. Y. Lau, M. A. Hannan, and Shirley Gee Hoon Tang. ‘Applications of Photonics in Agriculture Sector: A Review’. *Molecules* 24, no. 10 (January 2019): 2025. <https://doi.org/10.3390/molecules24102025>
 22. Li, Lei, Qin Zhang, and Danfeng Huang. ‘A Review of Imaging Techniques for Plant Phenotyping’. *Sensors* 14, no. 11 (November 2014): 20078–111.
<https://doi.org/10.3390/s141120078>.
 23. Ali, Ansar, and Muhammad Imran. ‘Remotely Sensed Real-Time Quantification of Biophysical and Biochemical Traits of Citrus (*Citrus Sinensis* L.) Fruit Orchards – A Review’. *Scientia Horticulturae* 282 (10 May 2021): 110024.
<https://doi.org/10.1016/j.scienta.2021.110024>.
 24. Goh, Jia Quan, Abdul Rashid Mohamed Shariff, and Nazmi Mat Nawi. ‘Application of Optical Spectrometer to Determine Maturity Level of Oil Palm Fresh Fruit Bunches Based on Analysis of the Front Equatorial, Front Basil, Back Equatorial, Back Basil and Apical Parts of the Oil Palm Bunches’. *Agriculture* 11, no. 12 (December 2021): 1179. <https://doi.org/10.3390/agriculture11121179>.
 25. Li, Jiangbo, Wei Luo, Zheli Wang, and Shuxiang Fan. ‘Early Detection of Decay on Apples Using Hyperspectral Reflectance Imaging Combining Both Principal Component Analysis and Improved Watershed Segmentation Method’. *Postharvest Biology and Technology* 149 (March 2019): 235–46.
<https://doi.org/10.1016/j.postharvbio.2018.12.007>.

26. Sánchez, Natalia Hernández, Sébastien Lurol, Jean Michel Roger, and Véronique Bellon-Maurel. 'Robustness of Models Based on NIR Spectra for Sugar Content Prediction in Apples'. *Journal of Near Infrared Spectroscopy* 11, no. 2 (1 April 2003): 97–107. <https://doi.org/10.1255/jnirs.358>.
27. Giovanelli, G., N. Sinelli, R. Beghi, R. Guidetti, and E. Casiraghi. 'NIR Spectroscopy for the Optimization of Postharvest Apple Management'. *Postharvest Biology and Technology* 87 (1 January 2014): 13–20. <https://doi.org/10.1016/j.postharvbio.2013.07.041>.
28. Zude-Sasse, Manuela, Ingo Truppel, and Bernd Herold. 'An Approach to Non-Destructive Apple Fruit Chlorophyll Determination'. *Postharvest Biology and Technology* 25, no. 2 (1 June 2002): 123–33. [https://doi.org/10.1016/S0925-5214\(01\)00173-9](https://doi.org/10.1016/S0925-5214(01)00173-9).
29. Shariati, Mahdi, Mohammad Saeed Mafipour, Peyman Mehrabi, Ali Shariati, Ali Toghroli, Nguyen Thoi Trung, and Musab N. A. Salih. 'A Novel Approach to Predict Shear Strength of Tilted Angle Connectors Using Artificial Intelligence Techniques'. *Engineering with Computers* 37, no. 3 (1 July 2021): 2089–2109. <https://doi.org/10.1007/s00366-019-00930-x>
30. Mammoliti, Elisa, Francesco Di Stefano, Davide Fronzi, Adriano Mancini, Eva Savina Malinverni, and Alberto Tazioli. 'A Machine Learning Approach to Extract Rock Mass Discontinuity Orientation and Spacing, from Laser Scanner Point Clouds'. *Remote Sensing* 14, no. 10 (January 2022): 2365. <https://doi.org/10.3390/rs14102365>.
31. Ribeiro Junior, Franklin M., Reinaldo A. C. Bianchi, Ronaldo C. Prati, Kari Kolehmainen, Juha-Pekka Soininen, and Carlos A. Kamienski. 'Data Reduction Based on Machine Learning Algorithms for Fog Computing in IoT Smart Agriculture'. *Biosystems Engineering*, 25 January 2022. <https://doi.org/10.1016/j.biosystemseng.2021.12.021>
32. Henrique da Silva Melo, Bruno, Rafaella Figueiredo Sales, Lourival da Silva Bastos Filho, Jorge Souza Povoas da Silva, Aluska Gabrielle Carolino de Almeida Sousa, Deborah Maria Camará Peixoto, and Maria Fernanda Pimentel. 'Handheld near Infrared Spectrometer and Machine Learning Methods Applied to the Monitoring of Multiple Process Stages in Industrial Sugar Production'. *Food Chemistry* 369 (1 February 2022): 130919. <https://doi.org/10.1016/j.foodchem.2021.130919>

33. Wang, Zhaodi, Menghan Hu, and Guangtao Zhai. 'Application of Deep Learning Architectures for Accurate and Rapid Detection of Internal Mechanical Damage of Blueberry Using Hyperspectral Transmittance Data'. *Sensors* 18, no. 4 (April 2018): 1126. <https://doi.org/10.3390/s18041126>.
34. Munera, Sandra, José Blasco, Jose M. Amigo, Sergio Cubero, Pau Talens, and Nuria Aleixos. 'Use of Hyperspectral Transmittance Imaging to Evaluate the Internal Quality of Nectarines'. *Biosystems Engineering* 182 (1 June 2019): 54–64. <https://doi.org/10.1016/j.biosystemseng.2019.04.001>.
35. Zhaoyong, Zhou, Lei Yu, Su Dong, Zhang Haihui, He Dongjian, and Chenghai Yang. 'Detection of Moldy Core in Apples and Its Symptom Types Using Transmittance Spectroscopy'. *International Journal of Agricultural and Biological Engineering* 9, no. 6 (2016): 148–55. <http://www.ijabe.org/index.php/ijabe/article/view/2235>
36. Shenderay, Clara, Itzhak Shmulevich, Victor Alchanatis, Haim Egozi, Aharon Hoffman, Viacheslav Ostrovsky, Susan Lurie, Ruth Ben Arie, and Ze'ev Schmilovitch. 'NIRS Detection of Moldy Core in Apples'. *Food and Bioprocess Technology* 3, no. 1 (February 2010): 79–86. <https://doi.org/10.1007/s11947-009-0256-1>.
37. Tian, Xi, Qingyan Wang, Wenqian Huang, Shuxiang Fan, and Jiangbo Li. 'Online Detection of Apples with Moldy Core Using the Vis/NIR Full-Transmittance Spectra'. *Postharvest Biology and Technology* 168 (October 2020): 111269. <https://doi.org/10.1016/j.postharvbio.2020.111269>.
38. Jacquez, Jonn A., and Hans F. Kuppenheim. 'Theory of the Integrating Sphere'. *JOSA* 45, no. 6 (1 June 1955): 460–70. <https://doi.org/10.1364/JOSA.45.000460>
39. M, Hossin, and Sulaiman M.N. 'A Review on Evaluation Metrics for Data Classification Evaluations'. *International Journal of Data Mining & Knowledge Management Process* 5, no. 2 (31 March 2015): 01–11. <https://doi.org/10.5121/ijdkp.2015.5201>
40. Marom, Nadav David, Lior Rokach, and Armin Shmilovici. 'Using the Confusion Matrix for Improving Ensemble Classifiers'. In *2010 IEEE 26-Th Convention of Electrical and Electronics Engineers in Israel*, 000555–59, 2010. <https://doi.org/10.1109/EEEI.2010.5662159>.
41. Fabian Pedregosa; Gaël Varoquaux; Alexandre Gramfort; Vincent Michel; Bertrand Thirion; Olivier Grisel; Mathieu Blondel; Peter Prettenhofer; Ron Weiss; Vincent Dubourg; Jake Vanderplas; Alexandre Passos; David Cournapeau; Matthieu Perrot;

- Édouard Duchesnay (2011). "[Scikit-learn: Machine Learning in Python](#)". *Journal of Machine Learning Research*. 12: 2825–2830
42. Myles, Anthony J., Robert N. Feudale, Yang Liu, Nathaniel A. Woody, and Steven D. Brown. ‘An Introduction to Decision Tree Modeling’. *Journal of Chemometrics* 18, no. 6 (2004): 275–85. <https://doi.org/10.1002/cem.873>.
43. Breiman, Leo. ‘Random Forests’. *Machine Learning* 45, no. 1 (1 October 2001): 5–32. <https://doi.org/10.1023/A:1010933404324>.
44. Gulzat, Turken, Naizabayeva Lyazat, Vladimír Siládi, Gulbakyt Sembina, and Satymbekov Maksatbek. ‘Research on Predictive Model Based on Classification with Parameters of Optimization’. *Neural Network World* 30 (1 January 2020): 295–308. <https://doi.org/10.14311/NNW.2020.30.020>.
45. Omar, Norshafarina Binti, Fatimatufaridah Binti Jusoh, Roliana Binti Ibrahim, and Mohd Shahizan Bin Othman. ‘Review of Feature Selection for Solving Classification Problems’, n.d., 7 (2013). https://www.researchgate.net/publication/282971834_Review_of_Feature_Selection_for_Solving_Classification_Problems
46. Chen, RC., Dewi, C., Huang, SW. *et al.* Selecting critical features for data classification based on machine learning methods. *J Big Data* 7, 52 (2020). <https://doi.org/10.1186/s40537-020-00327-4>
47. Cho, Byoung-Kwan, Moon S. Kim, In-Suck Baek, Dae-Yong Kim, Wang-Hee Lee, Jongkee Kim, Hanhong Bae, and Young-Sik Kim. ‘Detection of Cuticle Defects on Cherry Tomatoes Using Hyperspectral Fluorescence Imagery’. *Postharvest Biology and Technology* 76 (1 February 2013): 40–49. <https://doi.org/10.1016/j.postharvbio.2012.09.002>.
48. Jason Brownlee, *How to Perform Feature Selection With Numerical Input Data*, <https://machinelearningmastery.com/feature-selection-with-numerical-input-data/> , accessed January 7th, 2022.
49. Hagan, M.T., H.B. Demuth, and M.H. Beale, *Neural Network Design*, Boston, MA: PWS Publishing, 2017. <https://doi.org/10.1016/j.ijrmms.2017.03.012>
50. Scales, L. E. ‘Introduction to Non-Linear Optimization’. Macmillan International Higher Education, 1985. <https://books.google.com/books?hl=it&lr=&id=AEJdDwAAQBAJ&oi=fnd&pg=PR9&dq=Scales,+L.+E.+%E2%80%98Introduction+to+Non->

51. Phansalkar, V.V., and P.S. Sastry. 'Analysis of the Back-Propagation Algorithm with Momentum'. *IEEE Transactions on Neural Networks* 5, no. 3 (May 1994): 505–6. <https://doi.org/10.1109/72.286925>.
52. Zhang, Jingcheng, Yanbo Huang, Ruiliang Pu, Pablo Gonzalez-Moreno, Lin Yuan, Kaihua Wu, and Wenjiang Huang. 'Monitoring Plant Diseases and Pests through Remote Sensing Technology: A Review'. *Computers and Electronics in Agriculture* 165 (1 October 2019): 104943. <https://doi.org/10.1016/j.compag.2019.104943>
53. Martinelli, Federico, Riccardo Scalenghe, Salvatore Davino, Stefano Panno, Giuseppe Scuderi, Paolo Ruisi, Paolo Villa, et al. 'Advanced Methods of Plant Disease Detection. A Review'. *Agronomy for Sustainable Development* 35, no. 1 (1 January 2015): 1–25. <https://doi.org/10.1007/s13593-014-0246-1>
54. Pu, Yuan-Yuan, Yao-Ze Feng, and Da-Wen Sun. 'Recent Progress of Hyperspectral Imaging on Quality and Safety Inspection of Fruits and Vegetables: A Review'. *Comprehensive Reviews in Food Science and Food Safety* 14, no. 2 (2015): 176–88. <https://doi.org/10.1111/1541-4337.12123>
55. Shihab, Tay H., Amjed N. Al-Hameedawi, and Ammar M. Hamza. 'Random Forest (RF) and Artificial Neural Network (ANN) Algorithms for LULC Mapping'. *Engineering and Technology Journal* 38, no. 4 (25 April 2020): 510–14. <https://doi.org/10.30684/etj.v38i4A.399>.
56. Raczko, Edwin, and Bogdan Zagajewski. 'Comparison of Support Vector Machine, Random Forest and Neural Network Classifiers for Tree Species Classification on Airborne Hyperspectral APEX Images'. *European Journal of Remote Sensing* 50, no. 1 (1 January 2017): 144–54. <https://doi.org/10.1080/22797254.2017.1299557>.
57. Hinton, Geoffrey E. '20 - CONNECTIONIST LEARNING PROCEDURES' This Chapter Appeared in Volume 40 of *Artificial Intelligence* in 1989. <https://doi.org/10.1016/B978-0-08-051055-2.50029-8>
58. Breiman, Leo, Jerome H. Friedman, Richard A. Olshen, and Charles J. Stone. *Classification And Regression Trees*. New York: Routledge, 2017. <https://doi.org/10.1201/9781315139470>
59. Trinci, A. P. J. YR 1971. 'Exponential Growth of the Germ Tubes of Fungal Spores'. *Microbiology* 67, no. 3 (n.d.): 345–48. <https://doi.org/10.1099/00221287-67-3-345>

60. Rojas, Raúl. 'The Backpropagation Algorithm'. In *Neural Networks: A Systematic Introduction*, edited by Raúl Rojas, 149–82. Berlin, Heidelberg: Springer, 1996. https://doi.org/10.1007/978-3-642-61068-4_7
61. Abiodun, Oludare Isaac, Aman Jantan, Abiodun Esther Omolara, Kemi Victoria Dada, Nachaat AbdElatif Mohamed, and Humaira Arshad. 'State-of-the-Art in Artificial Neural Network Applications: A Survey'. *Heliyon* 4, no. 11 (1 November 2018): e00938. <https://doi.org/10.1016/j.heliyon.2018.e00938>.
62. Barbedo, Jayme Garcia Arnal. 'Impact of Dataset Size and Variety on the Effectiveness of Deep Learning and Transfer Learning for Plant Disease Classification'. *Computers and Electronics in Agriculture* 153 (1 October 2018): 46–53. <https://doi.org/10.1016/j.compag.2018.08.013>.

Chapter four

Conclusions

This PhD thesis presented novel low-cost hyperspectral applications for high-throughput phenotyping and post-harvest quality control in apple fruits, focusing on an industrial context application of the hyperspectral technologies.

The Senop HSC-2 hyperspectral low-cost camera (HSC-2) was successfully optimised, developing a novel correction method to obtain an optimised radiance output. The presence of spectral jumps and falls in the HSC-2 spectrum and the background noise, due to the intrinsic characteristics and sensitivity of the hyperspectral camera optical sensors, were substantially reduced by using the novel correction method developed in this PhD thesis. In addition, the influence of the dark current signal on the hyperspectral output was computed, permitting the improvement of the spectral results. Based on the results, the HSC-2 low-cost hyperspectral camera can be considered a powerful tool in hyperspectral applications, such as crop monitoring and disease detection, especially in the near-infrared spectral range from 650 to 820 nm. The optimisation of the HSC-2 hyperspectral outputs obtained by the radiance correction method developed has first permitted the use of the HSC-2 in a high-throughput phenotyping context.

The HSC-2 was integrated into a high-throughput phenotyping platform during a tomato drought stress experiment conducted using four untested tomato genotypes (Red Setter, Torremaggiore, 770P and 990P) characterised by high industrial interest. The genotypes were tested during two cycles of full and partial irrigation for two months. The principal phenotyping traits were assessed by processing the images acquired by the phenotyping platform acquisition. The environmental parameters were processed and compared with the phenotyping results. A novel hyperspectral acquisition setup was made in the high-throughput phenotyping platform, and an innovative segmentation method was developed and tested, reducing the hyperspectral dataset dimension by 85.5%. In addition, the time processing for the hyperspectral images was highly reduced. Achieving the optimisation of the storage space and the data processing time reduction are two relevant goals, representing a starting point for further developments and applications of low-cost hyperspectral technologies in a phenotyping industrial context.

An hyperspectral index (H-index) capable of detecting the water stress status was successfully developed and tested. The genotype's response to the water stress obtained using the phenotyping platform image analysis was compared to a novel H-index developed in this PhD thesis. The H-index has demonstrated better efficiency in water stress detection in the first stress stages, highlighting a higher sensitivity compared to the phenotyping traits obtained by the high-throughput phenotyping platform. Based on the H-index and OIs results, the genotype's water stress resistance was assessed for all genotypes, and 770P and 990P were more susceptible to water stress than Red Setter and Torremaggiore genotypes. Therefore, the integration of a hyperspectral instrument in the high-throughput phenotyping platform in ALSIA is currently being evaluated.

A novel low-cost hyperspectral technology was also developed to improve post-harvest quality control in the apple industry. Indeed, a low-cost hyperspectral system based on a light collection by an integrating sphere and the Ocean optics USB 2000 spectrometer, was successfully developed and tested during a laboratory-controlled experiment. Seventy apples of the Golden Delicious variety were infected by *Alternaria alternata*, one of the primary pathogens responsible for the moldy core disease. The apples were measured during five measurement rounds for 13 days. Based on correlation analysis results, the spectral features more linked to the moldy core presence were identified in the spectral region from 863.38 to 877.69 nm. Two binary classification models based on Artificial Neural Network Pattern Recognition and Bagging Classifier with decision trees were developed, revealing a better detection capability by Artificial Neural Network Pattern Recognition, especially in the early stage of infection. Indeed, the Artificial Neural Network's predictive accuracy was 100% in round 1 and 97.15% in round 2. The proposed system surpassed previous moldy core detection methods needing only one measurement per fruit and improving over ten times the minimum infection level used in previous studies. Those results have a notable significance in an automated industrial context, where increased speed and measurement precision positively impacts the entire quality control process.

Overall, the results obtained in this PhD open new ways to the application of low-cost hyperspectral technologies in an industrial-research context. Further models of low-cost hyperspectral cameras can be tested and optimised by applying the correction method developed in this PhD. Low-cost hyperspectral technologies can be further applied to detect abiotic and biotic stresses in a phenotyping context, with the aim of conducting

phenotyping experiments in the open field. The apparatus developed for moldy core detection can be tested on other fruits, apple varieties and diseases such as biotic and abiotic internal browning, and post-harvest CO₂ damage. In addition, the link between skin color, texture, biochemical contents, and spectral response can be explored.

Further development of the results obtained in this PhD thesis can be the optimization of the measurement time per fruit, with the final objective of the industrial application of the measurement system developed.

Finally, spectral investigations based on the methods developed in this PhD can be extended using hyperspectral instruments with a more comprehensive spectral range, increasing the industrial interest toward developing and applying of low-cost hyperspectral technologies in agricultural processes.

Further activities carried out during the PhD period

Peer-reviewed journal articles

Genangeli Andrea, Giorgio Allasia, Marco Bindi, Claudio Cantini, Alice Cavaliere, Lorenzo Genesisio, Giovanni Giannotta, Franco Miglietta, and Beniamino Gioli. ‘A Novel Hyperspectral Method to Detect Moldy Core in Apple Fruits’. *Sensors* 22, no. 12 (January 2022): 4479. <https://doi.org/10.3390/s22124479>

Damm, A., S. Cogliati, R. Colombo, L. Fritsche, A. Genangeli, L. Genesisio, J. Hanus, et al. ‘Response Times of Remote Sensing Measured Sun-Induced Chlorophyll Fluorescence, Surface Temperature and Vegetation Indices to Evolving Soil Water Limitation in a Crop Canopy’. *Remote Sensing of Environment* 273 (1 May 2022): 112957. <https://doi.org/10.1016/j.rse.2022.112957>

Book chapters

Di Cicco, Annalisa, Remika Gupana, Alexander Damm, Simone Colella, Federico Angelini, Luca Fiorani, Florinda Artuso, Brando, Vittorio Ernesto; Lai, Antonia; Genangeli Andrea; Miglietta, Franco ; Santoleri, Rosalia. “Flex 2018” Cruise: An Opportunity to Assess Phytoplankton Chlorophyll Fluorescence Retrieval at Different Observative Scales’. In *Proceedings e Report*, edited by Laura Bonora, Donatella Carboni, and Matteo De Vincenzi, 1st ed., 126:688–97. Florence: Firenze University Press, 2020. <https://doi.org/10.36253/978-88-5518-147-1.68>

Oral communications

Andrea Genangeli, Giorgio Allasia, Marco Bindi, Claudio Cantini, Alice Cavaliere, Lorenzo Genesisio, Giovanni Giannotta, Franco Miglietta, Beniamino Gioli. ‘Metodologia non invasiva di detection iperspettrale del marciume del cuore della mela nella fase di post-raccolta’. 8° Convegno Nazionale GdL SOI Postraccolta, Pescia (PT), 29-30 settembre 2022.

Abraham Mejia Aguilar, Andrea Vianello, A. Genangeli, G Giannotta, Roberto Monsorno. ‘Low-Cost and Autonomous Hyperspectral Sensor Node for Precision Agriculture Methods’. *SFScon South Tyrol Free Software Conference 2021* (Bolzano /

Bozen, 11/11/2021 - 12/11/2021).

https://bia.unibz.it/esploro/outputs/conferencePresentation/Low-cost-and-autonomous-hyperspectral-sensor-node/991006249097701241?institution=39UBZ_INST

Poster

Antonia Corvino, Michela Palumbo, Ilde Ricci, Maria Cefola, Beniamino Gioli, Andrea Genangeli, Giovanni Giannotta, Bernardo Pace. ‘Impiego di tecniche iperspettrali per predire il contenuto in zuccheri in frutti di actinidia’. 8° Convegno Nazionale GdL SOI Postraccolta, Pescia (PT), 29-30 settembre 2022.

Alessandra Ruggiero, Anna Tedeschi, Gaetano Guarino, Andrea Genangeli, Angelo Petrozza, Antonello Costa, Stephan Summerer, Giorgia Batelli, Stefania Grillo. “Digital phenotypes during recurrent drought stress: screening of a tomato collection”. LXV SIGA Annual Congress From genes to fork - On Mendel's footsteps, Piacenza, 6-9 September 2022.

Workshops

ANNUAL MEETING PROGETTO E-crops (<https://www.e-crops.it/>) :

“Trappole e sensori ottici” Giovanni Giannotta (FOS), Genangeli (UNIFI, IBE, FOS). (Oral communication).

“Sviluppo di metodologie di inferenza su fenotipi digitali: integrazione di una tecnologia iperspettrale low-cost in una HTPP” Genangeli A. et al. (CNR, ALSIA, FOS). (Oral communication).

“Stima di crop traits per attività di field phenotyping su frumento con dati multi e iperspettrali di proximal e aerial remote sensing: risultati preliminari della campagna E-CROPS 2022 ad Arborea (OR)” Boschetti M., Heidarian R., Candiani G., De Peppo M., Cesaraccio C., Mereu S., Duce. P., Serralutzu F., Cillis D., Cipriani A., Groli E., Ravaglia S., Arghittu P., Moresi F.V., Maesano M., Genangeli A., Carotenuto F., Gioli B. (CNR, BF, UNITUS, UNIFI).

“Tecniche non-distruttive per la predizione del grado di maturazione di fragole e kiwi”.
Cefola, Pace, Corvino, Palumbo, Ricci, Sicuro, Gioli, Genangeli, Giannotta (CNR, FOS,
UNIFI)

“Digitalizzazione del fenotipo in piattaforma HTPP: l'esempio degli stress biotici su pomodoro” Cillo F., Stavelone L., Veronico P., Melillo M.T., Genangeli A., Bubici G., Prigigallo M.I., Sportelli G. (CNR, UNIFI)

**“Attività scientifica di CAL/VAL della missione PRISMA” Riunione
Tecnica 5**

<https://www.asi.it/scienze-della-terra/prisma/>

“Attività di rilevamento su sistemi agricoli condotta ad Arborea (OR)”; A. Genangeli,
B. Gioli, S. Mereu (IBE, UNIFI), M. Pepe, M. Boschetti (IREA) (Oral communication).